

Copyright

by

Carl William Magnuson

2014

**The Dissertation Committee for Carl William Magnuson certifies that this is the  
approved version of the following dissertation:**

**Chemical Vapor Deposition Graphene on Polycrystalline Copper Foil**

**Committee:**

---

Deji Akinwande, Supervisor

---

Rodney S. Ruoff, Co-supervisor

---

Eric M. Taleff

---

Ken Shih

---

Luigi Colombo

# **Chemical Vapor Deposition Graphene on Polycrystalline Copper Foil**

**by**

**Carl William Magnuson, B.S.**

**Dissertation**

Presented to the Faculty of the Graduate School of

The University of Texas at Austin

in Partial Fulfillment

of the Requirements

for the Degree of

**Doctor of Philosophy**

**The University of Texas at Austin**

**May 2014**

## **Dedication**

In memory of

Gary Norris

(1982-2009)

## **Acknowledgements**

First, I thank my friends and coworkers in Los Angeles for encouraging and supporting my decisions to return to graduate school and pursue my doctoral degree. Specifically, my co-workers at Northrop Grumman - Noel Villegas, Tony DiNardo, and Mark Innocenzi - for all they taught me and instilling in me a need for a greater skill set that only an advanced degree could deliver. My manager, Joan Butterfield, had an unselfish desire to see me succeed even if it meant losing me as an employee and integral member of her team. Without them, I never would have undertaken this challenge.

Next I thank Sandia National Labs for their generous fellowship through their Laboratory Directed Research and Development program supporting me financially for three of these years. Without them I could not have given 100% of my energy and attention to my research while keeping a roof over my head and food in my belly. I specifically thank my mentor at Sandia, Michael Brumbach, and the UT campus recruiter, Mark Ladd. Mike helped guide and complete the yearly grant proposals and reviews for my research and took care of all the other behind-the-scenes paper work to keep my funding going. Mark was sure to have a meal with me every time he was in Austin to find out if everything was running smoothly and, more importantly, that I was happy.

Michael Ronalter and Adam Kennedy, at the university's glass shop, taught me glass blowing skills that I could not have learned in any class at the university. For an

entire semester I came in for two hours a day twice a week and learned the basics of glass blowing. They emphasized how to make useful and common lab equipment, like condensers and bubblers, using minimal tools that I would likely have available to me when working outside a glass shop. Of course, they also did a great job making the quartz-ware and other glass parts I needed throughout my research. They were both truly indispensable for completing my research.

I work with a great group of researchers. Specifically the post-docs that I got to work so closely with and learn so much from: Aruna Velamakanni, Weiwei Cai, and Xuesong Li. Aruna helped me when I first arrived at UT to become familiar with laboratory research. Weiwei taught me countless lab tricks and practical skills. Xuesong's ground breaking work on graphene growth on copper via CVD intrigued me enough to finish this dissertation on the subject. He was unselfish with his ideas and research, sharing them both with me, wanting nothing in return except that I use them to succeed in my own research. I need to thank all my colleagues in the Ruoff Research group: not only the posts-docs, but the numerous and talented visiting scholars from all around the world, my fellow grad students, and – not to be overlooked – the handful of undergraduate students I got to mentor and learn from. Richard Piner kept most of the shared characterization equipment (SEM, micro-Raman, etc.) up and running and accomplished great AFM studies. The research administrators, Shannon Wilkerson and Dustin Wilson were both wonderful at navigating the bureaucracy of the university. Finally – and most importantly – my advisor, Prof. Ruoff truly assembled a world class

research group at UT. I am constantly in awe of his dedication and ability to generate ground breaking research year after year.

I thank my entire dissertation committee: Professors Ruoff, Taleff, Shih, and Akinwande and Dr. Colombo. Unfortunately, Prof. Ventrice was removed from my committee after moving from Texas State to SUNY College of Nanoscale Science & Engineering, but he has continued mentoring me and reviewing my work (including this dissertation). Prof. Akinwande stepped up to become my supervisor after Prof. Ruoff left the University of Texas shortly before my final oral exam. They have all given me great advice and suggestions for my research. They have also spent their all-too-limited time editing and reviewing this dissertation; I specifically thank Prof. Ruoff for his very detailed review of this dissertation.

Finally, I thank my loving wife Whitney for making this all that much more worth doing. I love you, Whitney.

# Chemical Vapor Deposition Graphene on Polycrystalline Copper Foil

Carl William Magnuson, Ph.D.

The University of Texas at Austin, 2014

Supervisor: Deji Akinwande

Co-supervisor: Rodney S. Ruoff

Abstract: Graphene, a single atomic layer of  $sp^2$ -bonded carbon, has been of significant interest to basic sciences and engineering. Among its unique properties are exceptional mechanical strength, from the strong carbon-carbon bond; high in-plane thermal conductivity; high carrier mobilities, since electrons and holes travel through graphene as mass-less Dirac fermions; and quantum effects (such as the quantum Hall effect), which can be observed at room temperature.

In 2009, Li *et al.*, of Professor Ruoff's research group at the University of Texas at Austin, published a seminal paper detailing the production of fairly high quality graphene grown on copper foils using chemical vapor deposition (CVD). The potential for scalability of graphene CVD processing is extremely attractive, and this is currently the most promising method for its commercial viability, particularly for transparent conductive electrodes (TCEs). Here, graphene-based TCEs are compared with TCEs made with multi-walled carbon nanotubes (MWCNTs). A novel technique to reduce the

sheet resistance of MWCNT-based TCEs in half is described in detail. Even with these improvements, graphene-based TCEs outperform MWCNT-based TCEs.

The decomposition of copper oxides at high temperatures in an oxygen deficient environment is characterized. The ability for the oxygen evolved from the copper foil during this decomposition to react with carbon on the surface of the copper substrate is verified. This phenomenon was used to develop a technique for getting clean pre-graphene growth copper substrates and allowing repeatable graphene nucleation results.

A technique for growing large graphene domains inside a copper vapor trapping ‘copper enclosure’ is described. The quality of the graphene grown inside the copper enclosure is characterized and shown to be of very high quality. This technique can grow graphene domains over 0.5 mm across.

Finally, a possible cause of graphene ad-layer growth on the copper surface is suggested. It is proposed that gas diffusing through the copper substrate at high temperature delaminates the graphene from the copper surface in some regions. This then allows carbon containing molecules to diffuse under the graphene and grow new graphene layers. The increased ad-layer growth in the presence of helium supports this.

## Table of Contents

List of Figures .....	xii
Chapter One: Introduction.....	1
1.1. Motivation.....	1
Graphene properties and potential uses .....	2
1.2. Graphene fabrication techniques.....	5
1.3. Goals .....	7
Chapter Two: CVD Growth Systems.....	8
2.1. CVD with Four Inch Chamber.....	8
2.2. RF Inductive Heating CVD System.....	15
2.3. Pros and Cons of RF and Thermal CVD Systems .....	18
Chapter Three: Substrate Pre-growth Preparation .....	24
3.1. The Challenge of Getting a Clean Pre-growth Substrate.....	24
3.2. Experimental Details.....	27
3.3. Data and Results .....	28
Chapter Four: CNT and Graphene Transparent Conductive Electrodes.....	36
4.1. Site-Specific Deposition of Au Nanoparticles in CNT Films by Chemical Bonding.....	38
Introduction.....	39
Results and Discussions.....	42
Conclusions.....	58
Methods.....	59
Characterization .....	64
4.2. Graphene based TCEs.....	65
Graphene/metal nanowires hybrid .....	66
Graphene/CNT bybrid .....	67

Chapter Five: Large Graphene Domains .....	69
5. Achieving Large Graphene Domains Inside a Copper Enclosure .....	71
Introduction:.....	71
Chapter Six: Graphene ad-layers .....	83
Introduction:.....	83
Methods: .....	85
Graphene Synthesis.....	85
Characterization. ....	87
Results and Discussion: .....	87
Chapter Seven: Conclusions.....	96
Chapter Eight: Future Research Directions.....	98
<b>Appendix</b> .....	100
Acronyms.....	100
List of Publications .....	101
<b>References</b> .....	103
<b>Vita</b> 114	

## List of Figures

Figure 1.1.	Graphene is a single atomic layer of $sp^2$ -bonded carbon and can be thought of as an unrolled bucky-ball or carbon nanotube or a single layer of graphite <sup>16</sup> .	2
Figure 1.2.	Effective mobility of single-layer graphene transistors made using graphene grown via low-pressure CVD as a function of channel dimensions <sup>1</sup> .	4
Figure 1.3.	a) TEM image of chemically exfoliated graphene from Boehm's 1962 publication <sup>24</sup> . b) Optical microscopy photo of mechanically exfoliated graphene on a Si/SiO <sub>2</sub> wafer from the University of Manchester. ....	6
Figure 2.1.	Photo of computer controlled and monitored graphene CVD system with 4-inch diameter growth chamber. ....	9
Figure 2.2.	The temperature profile of the 4 inch diameter tube furnace.....	11
Figure 2.3.	The graphical user interface for the LabView programed CVD system control and monitoring software.....	14
Figure 2.4.	Solid works model image of the inductively heated CVD system. ..	15
Figure 2.5.	Photo of a 125 $\mu\text{m}$ thick 2 inch by 0.5 inch copper foil being heated by inductive heating.....	18
Figure 2.6.	The oxygen and argon pressure in the tube furnace CVD system before and after <i>in-situ</i> high temperature (1000 °C) oxidation. ....	20
Figure 2.7.	Photo of the cold-zone region of the tube furnace with copper deposited on the inside of the quartz tube. ....	21

Figure 2.8. Photo of copper foil after localized melting in the inductively heated CVD system. ....	23
Figure 3.1. SEM image of a copper foil with a sub-monolayer of graphene after being annealed under 700 Torr 5% hydrogen in argon at 1030 °C. Not only are the graphene islands still present, but the electron beam induced deposition (EBID), from looking at the sample with SEM prior to annealing, is also still present. ....	26
Figure 3.2. SEM images of (a) 99.8% Cu foil and (b) OFHC Cu foil surfaces after cleaning with acetone, acetic acid, and annealing at 1040 °C for 1 hour under 10 sccm H <sub>2</sub> showing differing amounts of surviving carbon residue. Four of the small remaining residue spots have been circled in Figure 3.2a. Maps of the Raman G-peak position for graphene grown on (c) 99.8% copper and (d) OFHC copper. ....	30
Figure 3.3. Raman spectra from the same copper sample after being oxidized at 300 °C (CuO), vacuum annealed at 600 °C (Cu <sub>2</sub> O), and vacuum annealed at 1000 °C (Cu). ....	31
Figure 3.4. Log plot of the partial pressure of oxygen evolving from copper oxide versus inverse temperature while cooling the sample. ....	33
Figure 3.5. The oxygen, carbon monoxide, and carbon dioxide partial pressures in the CVD system versus the furnace temperature upon the initial heating of (a) just the CVD chamber and sample holder, (b) oxidized OFHC copper, (c) OFHC copper, and (d) 99.8% copper. ....	35
Figure 4.1. Photos of Samsung smart phone with the one on the left having a graphene based touch screen on the one and the right having a traditional ITO based touch screen <sup>65</sup> . ....	37

- Figure 4.2. (a) Schematic depicting the attachment of cysteine molecules to make Au-Cys nanoparticles. (b) Schematic showing the availability of the -NH<sub>2</sub> group for bonding upon changing the pH by addition of base (OH<sup>-</sup>) ions.....42
- Figure 4.3. TEM image of a post annealed MWCNT-COCl-AyCysNP network. The particles' sizes and positions are the same as before annealing.44
- Figure 4.4. (a) Bright-Field TEM micrograph of the MWCNT network showing Au-Cys nanoparticles at the nodes (circled) and one along a segment (squared). (b) A high magnification phase contrast image of one of the nodes. Insert: Micro-EDS line profile for gold and sulfur across the Au-Cys nanoparticle. (c) A bright-field STEM image of the MWCNT network showing the D-STEM beam positioned exactly at one of the Au-Cys nanoparticles labeled 'A'. (d) Spot diffraction pattern obtained by D-STEM from the nanoparticle shown in (c). The bright center spot in the diffraction pattern is (000). .....46
- Figure 4.5. TEM image of part of a MWCNT network with gold nanoparticles at a node (image obtained on networks after annealing), where both the segments and nodes of the network could be easily differentiated. The green lines represent the linear length of the MWCNTs occupied by the node and the red lines represent the segments. In this image, 2 of the 3 gold nanoparticles are located at a node (circled).....48

Figure 4.6. (a) TEM image of gold nanoparticles that were not capped with cysteine. The gold nanoparticles were not attached to MWCNTs and their sizes were both larger and their distribution varied more greatly than the gold nanoparticles capped with cysteine. (b) TEM image of a MWCNT network from the same sample as (a). (c) SEM image of a region of a MWCNT network with non-capped gold nanoparticles. Most of the gold nanoparticles are washed away during filtration in the film making process. A remaining particle is not at a network node. ....51

Figure 4.7. (a) XPS survey scan of MWCNT-AuCys films before and after annealing. The peaks corresponding to nitrogen and sulfur disappear after annealing. (b) Deconvolved C 1s peak for the un-annealed film. (c) Deconvolved C 1s peak for the annealed film. (d) The N 1s peak (400.5eV) before annealing; disappears after annealing. (e) Deconvolved S 2p peak. (f) The Au 4f peaks are present both before and after annealing. ....52

Figure 4.8. (a) Comparative survey spectra of as-purchased (dashed), MWCNT-COOH (dotted), and MWCNT-COCl (solid) samples. The MWCNT-COOH sample shows a clear increase in the oxygen content and the MWCNT-COCl sample shows a peak for Cl 2p. (b) The Cl 2p peak at 199.5 eV is indicative of a C-Cl bond that is incorporated due to the formation of CO-Cl bonds. ....55

Figure 4.9. Transmittance plot of films made from both pristine MWCNTs and MWCNT-Au-Cys. At 550 nm, the transmittance of the pristine MWCNT network is 53.1% and the MWCNT-Au-Cys network is 54.8%. ....56

Figure 4.10. I-V plots for the thin films made with pristine MWCNTs and MWCNT-Au-Cys before and after annealing. The non-linearities in the curves are an artifact of the characterization setup, not a property of the films. When the current supply changes between the high and low current regimes, the actual current is lower than reported causing dips in the I-V curves. To obtain the sheet resistance the slope of the I-V curve is multiplied by  $\pi/\ln 2$  ( $\sim 4.5$ ). From the slope of these I-V curves, the sheet resistance of the films was determined to be 41 k $\Omega/\square$  for the pristine MWCNT film, 580 k $\Omega/\square$  for the pre-annealed MWCNT-Au-Cys film, and 19.5 k $\Omega/\square$  for the post-annealed MWCNT-Au-Cys film. ....57

Figure 4.11. (a) TEM images showing intact endcaps on oxidized MWCNTs before functionalization with  $-\text{COCl}$  groups. The dark spot is not a gold nanoparticle but is due to mass thickness contrast. (b) and (c) show intact endcaps with and without gold nanoparticles respectively. (Scale bars in (b) and (c) are 50 nm.).....60

Figure 4.12. UV spectra of the gold hydrosol and of the cysteine capped gold nanoparticles. ....61

Figure 4.13. FTIR spectra of acid functionalized a) multiwalled carbon nanotubes (MWCNT-COOH), b) MWCNTs (MWCNT-COCl), c) MWCNTs linked with Au-Cys (MWCNT-AuCys).....63

Figure 4.14. Sheet resistance vs. transmittance for graphene based transparent conducting electrodes<sup>102</sup> .....66

Figure 4.15. (a) Typical SEM image of graphene/NW films. (b) SEM image of a NW crossing several line disruptions shown by arrows. (c) Optical microscopy image of the hybrid films with a dashed line corresponding to the Raman map ( $1560\text{--}1620\text{ cm}^{-1}$ ) showing a NW crossing with a line disruption in d. Scale bars in a, b, c, and d are  $6\text{ }\mu\text{m}$ . (e) Optical transmittance spectra of graphene and graphene/NW films. (f)  $R_s$  versus optical transmittance for graphene and graphene/NW films.<sup>103</sup> .....67

Figure 4.16. Transparent conducting films based on graphene and carbon nanotubes can achieve sheet resistances less than  $10\text{ }\Omega/\square$ <sup>104</sup>. .....68

Figure 5.1. a) SEM image of graphene island grown under low pressure. b) Optical-profilometer data of a graphene island on the same copper foil as a).70

Figure 5.2. (a) Copper foil enclosure prior to insertion in the furnace. (b) Schematic of the CVD system for graphene on copper.<sup>105</sup> .....72

Figure 5.3. Graphene growth inside the enclosure as a function of time for two methane flow rates and partial pressures at  $1035\text{ }^\circ\text{C}$ .<sup>105</sup> .....74

Figure 5.4. SEM images of graphene on copper grown by CVD. (a) Graphene domain grown at  $1035\text{ }^\circ\text{C}$  on Cu at an average growth rate of  $\sim 6\text{ }\mu\text{m}/\text{min}$ . (b) Graphene nuclei formed during the initial stage of growth. (c) High-surface-energy graphene growth front shown by the arrow in (a).<sup>105</sup> .....75

Figure 5.5. Raman map of the G bands corresponding to  $^{12}\text{C}$  (yellow) and  $^{13}\text{C}$  (black). The numbers in the figure correspond to the relative methane cycle numbers.<sup>105</sup> .....77

Figure 5.6. (a) PEEM image recorded near a graphene domain. The black line indicates the path from which selected-area diffraction patterns were recorded. The graphene is bright, and the surrounding Cu foil is dark. (b-e) Electron diffraction patterns (33 eV) recorded from 2  $\mu\text{m}$  areas of the graphene. Each pattern is labeled by the position along the black line in (a) at which the pattern was recorded. The diffraction spots are indicated in (b). (f) PEEM image recorded at the end of the scan.<sup>105</sup> .....78

Figure 5.7. (a) D-band and (b) G-band Raman maps of graphene within the domain and at the edges of the growing domain and (c) Raman spectra of large-domain graphene within the bulk of the film and along the dendrite. The FWHM of the 2D-band of the dendrite was slightly smaller than that of the bulk, and the ratio of the intensities of the 2D- and G-bands was larger for the dendritic region than the bulk, suggesting a lower carrier concentration for the dendritic region within the “bulk” of the domain and the tip of the dendrite. The 2D-peak FWHM was 38  $\text{cm}^{-1}$  for the bulk and 32  $\text{cm}^{-1}$  for the dendrite, whereas the G-band FWHM was  $\sim 23 \text{ cm}^{-1}$  for both regions.<sup>105</sup> .....80

Figure 5.8. Optical image of centimeter-scale graphene domains grown on the inside of an oxidized copper pocket<sup>114</sup>. .....82

Figure 6.1. SEM images of graphene grown from a) the inside of the copper enclosure and b) the outside of the same enclosure. The darker contrast areas indicate more graphene layers. ....89

Figure 6.2.	SEM images of a) mostly monolayer graphene grown with methane in purely argon atmosphere and b) graphene with many ad-layers grown with methane in a 5% hydrogen in argon atmosphere. Darker areas indicate graphene ad-layers. <sup>120</sup> .....	90
Figure 6.3.	SEM images from the same location on the same copper substrate after a) submonolayer graphene growth, b) oxidation and annealing under 5% hydrogen in argon at 700 °C for 10 seconds, and c) annealing at 1000 °C for one hour.....	92
Figure 6.4.	SEM images of graphene grown under (a-c) argon, (d-e) helium, and (g-i) 5% H <sub>2</sub> in argon. The samples were grown at (a,d,g) 1000 °C, (b,e,h) 1025 °C, and (c,f,i) 1050° C. ....	93
Figure 6.5.	a and b) Micro-raman maps of the graphene D and 2D peaks normalized to the G peak intensity for the sample grown under helium shown in Figure 6.4e. c) Raman map of the graphene 2D peak highlighting the ad-layer areas with a peak width of ~30 cm <sup>-1</sup> . Scale bars are 5 μm. ....	94

# Chapter One: Introduction

## 1.1. MOTIVATION

Graphene, defined as an isolated single layer of graphite, has promising electrical<sup>1-4</sup>, thermal<sup>5-6</sup>, mechanical<sup>7</sup>, and ‘quantum’<sup>3, 8</sup> properties. It has been the subject of intense research over the last 15 years<sup>9</sup> and several thorough review articles<sup>10-11</sup> have already been published on this topic as well as a detailed account of its history<sup>12</sup>. The term “graphene” was discussed in 1986<sup>13</sup> and later defined by IUPAC in 1997<sup>12</sup>, and graphene is defined as a monolayer of pure carbon with all carbon atoms perfectly sp<sup>2</sup>-bonded to all others. In 2009, Li *et al.* published a seminal paper in *Science* detailing graphene synthesis on copper foil via CVD using methane as the carbon precursor<sup>14</sup>. Since this technique can quickly and relatively inexpensively produce large single-layer graphene sheets that are limited only by the size of the copper substrate, it has quickly become the main method of producing graphene for both research and commercial applications. While, to date, graphene grown on copper has shown electrical properties equal to that of graphene exfoliated from HOPG<sup>15</sup>, the challenge of understanding and controlling its nucleation and growth remain largely unfinished – particularly on commercially available polycrystalline copper foil.

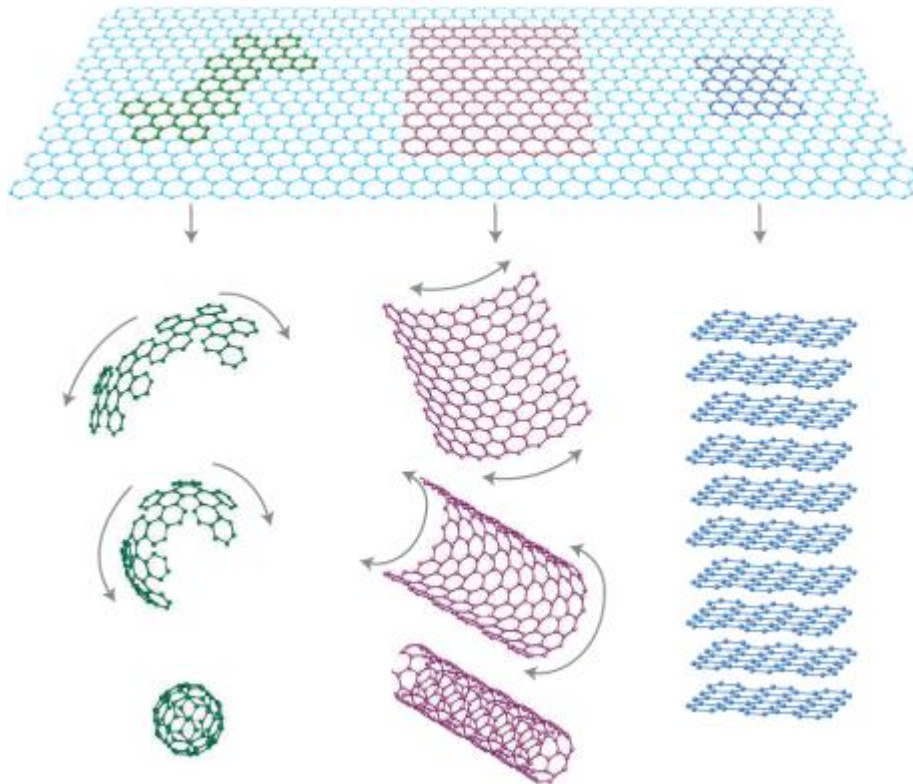


Figure 1.1. Graphene is a single atomic layer of  $sp^2$ -bonded carbon and can be thought of as an unrolled bucky-ball or carbon nanotube or a single layer of graphite<sup>16</sup>.

### **Graphene properties and potential uses**

While graphene is a single layer of graphite, there are colloquially used terms such as mono-layer, bi-layer, and even multi-layer to describe graphene. Mono-layer graphene is a single atomic layer of graphene; bi-layer graphene is two layers stacked on top of each other, either Bernal stacked as in graphite (referred to as AB stacked) or misoriented; multi-layer graphene has more than two graphene layers, and the stacking orientation can be again of interest. Multi-layer graphene may be referred to as ultrathin

graphite when the stacking order is the same as in graphite. The additional layers of graphene comprising bi-layer or multi-layer graphene are referred to as ad-layers when there is not complete coverage throughout of the first layer. Ad-layers can either be on top of or underneath the first/primary layer (with respect to, e.g., the growth substrate). A continuous area of graphene with the same crystallographic orientation is called a graphene domain. During the initial stages of growth, isolated regions of graphene will form that are called graphene islands. A graphene island may be a single crystal or can contain multiple graphene domains. Once graphene islands have grown together, they become a graphene sheet, and it has then been typical to refer to that as polycrystalline graphene containing single crystal grains.

Electrons in graphene can move as a 2D electron gas<sup>17</sup>. Because of this non-scattering, non-interacting movement of electrons, electron mobilities over 200,000  $\text{cm}^2/\text{V}\cdot\text{s}$  have been measured in suspended graphene at low temperature<sup>4</sup>. Even at room temperature on  $\text{SiO}_2$ , graphene's intrinsic electron mobility is still  $\sim 40,000 \text{ cm}^2/\text{V}\cdot\text{s}$ <sup>18</sup>. This extremely high electron mobility can be utilized in high speed electronics. Because the deposition of gold contacts on graphene reportedly does not affect graphene's electronic structure or electron-phonon coupling<sup>19</sup>, this allows graphene to be incorporated into many practical devices without sacrificing the high carrier mobility of graphene. However, the measured mobilities in graphene field-effect-transistors (FETs) are dependent on both the channel length and width<sup>1</sup>. Figure 1.2 shows this dependence using graphene I grew on copper via low pressure CVD. Graphene is neither a metal nor

semiconductor in that the band structure forms a Dirac cone with no band-gap at the charge neutrality point, thus making it a semi-metal<sup>20</sup>. Additionally, while the theoretical minimum conductance of graphene is only  $4e^2/h$  at this charge neutrality point of the Dirac cone, because of the interactions between carriers and often, when not suspended, a substrate, this value is increased somewhat, resulting in a higher minimum conductance and a parabolic shape to the gate-voltage measurements of graphene based FETs<sup>21</sup>. A thorough review of graphene based transistors has recently been published elsewhere<sup>10</sup>.

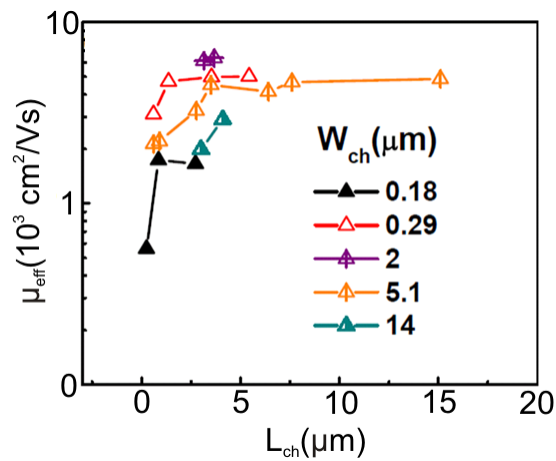


Figure 1.2. Effective mobility of single-layer graphene transistors made using graphene grown via low-pressure CVD as a function of channel dimensions<sup>1</sup>.

In addition to traditional transistor based electronics, graphene could usher in the era of quantum computing and has already been used to generate stable Q-bits for over 1 second at room temperature<sup>8</sup>. Graphene's uses go beyond electronic applications. Its huge surface/weight ratio of  $2630 \text{ m}^2/\text{g}$  also makes it of interest for ultra-capacitors and hydrogen storage<sup>22</sup>.

## 1.2. GRAPHENE FABRICATION TECHNIQUES

Graphene can be obtained by separating one carbon sheet from graphite. Graphene fabricated in this way is called exfoliated graphene. Because of its low defect density, mechanically exfoliated graphene is often used as the standard of high quality. The University of Manchester's mechanically exfoliated graphene obtained in their 2004 publication<sup>2</sup> involved using tape to pull a sheet of graphene from graphite; this method has become known as the "scotch-tape method"; the same method has been in use since the 1960's to achieve individual layers of, for example, metal chalcogenides. An optical microscope photo of graphene produced by this method is shown in Figure 1.3b. Chemical intercalants can also be used to separate graphene from graphite as shown in Figure 1.3a. This "chemically exfoliated graphene" currently yields lower quality graphene than that obtained by mechanical exfoliation due to the chemical process generating defects in the graphene layers. The graphene often becomes heavily oxidized, forming what has been called 'graphene oxide' to indicate an individual layer of graphite oxide. However, unlike mechanical exfoliation, chemical exfoliation can be scaled to produce large amounts of graphene/graphene oxide powder. These graphene oxide platelets have been layered to form a film and then reduced to 'reduced-graphene-oxide films of paper-like materials'<sup>23</sup>.

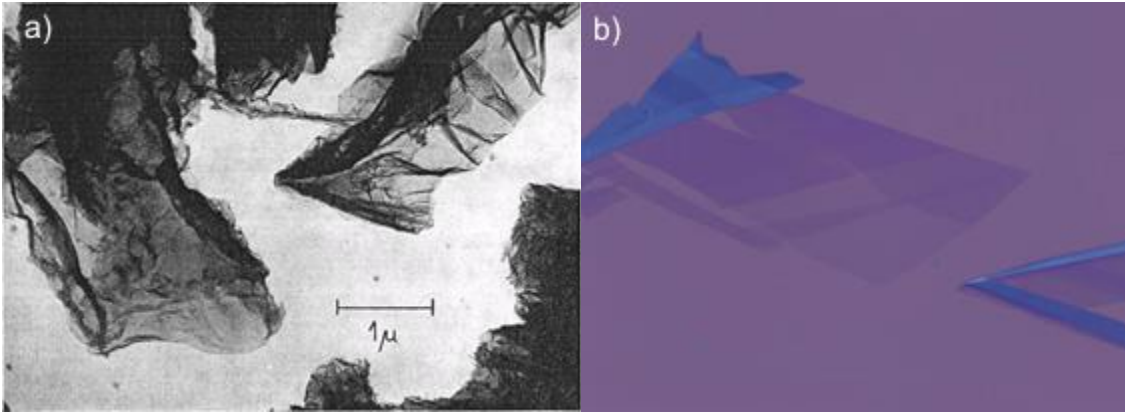


Figure 1.3. a) TEM image of chemically exfoliated graphene from Boehm's 1962 publication<sup>24</sup>. b) Optical microscopy photo of mechanically exfoliated graphene on a Si/SiO<sub>2</sub> wafer from the University of Manchester.

'High quality' large area graphene sheets can be synthesized via chemical vapor deposition (CVD) on metals. Besides the focus of this dissertation - graphene grown on copper - graphene has been grown on many other transition metals, such as Ru, Ir<sup>25-27</sup> and Pt(111)<sup>28</sup>. While growing graphene on Ni normally yields multi-layer graphene, monolayer graphene can also be grown on Ni(111) between 500 °C and 600 °C using ethylene<sup>29</sup>.

While graphene growth on non-metallic surfaces has been reported, it has also been pointed out that most hydrocarbons will decompose at high temperature without any catalyst (starting at 300 °C and almost completely at 1300 °C for methane) creating mainly sp<sup>2</sup>-bonded graphitic structures<sup>30-32</sup>. It is debated whether the "graphene" films grown on these non-metallic surface are actually graphene-like or simply thin films of

‘carbon black’-like material. While the ability to grow graphene on thick non-metallic surfaces is still debated, growth of graphene on a non-metal 2-D material currently being heavily researched, hBN, has been reported<sup>33</sup>.

### **1.3. GOALS**

The main goal of my research has been to investigate techniques for improving chemical vapor deposited graphene growth and compare its performance as a transparent conductive film to that of different carbon based transparent conductive electrodes made from multi-walled carbon nanotubes. To accomplish this, a low-pressure CVD system was designed and built using a 4 inch diameter tube-furnace. Using this system, a technique for *in-situ* cleaning of the copper substrates is developed, allowing for improved and repeatable graphene nucleation. The performance of graphene films grown with this technique as transparent conductive electrodes is compared to that of multi-walled carbon nanotube films. To improve the performance of the multi-walled carbon nanotube films, gold nanoparticles deposited at the nanotube network junctions was studied. To improve the performance of graphene films, a method of growing graphene inside a ‘copper enclosure’ to increase the graphene domain size was studied. Finally, since graphene ad-layers have a large effect on improving the performance of graphene-based conductive films, a possible cause of the ad-layer growth, which can facilitate either increasing or decreasing the amount of ad-layers in a graphene film, is studied.

## **Chapter Two: CVD Growth Systems**

While commercial CVD systems (e.g. AIXTRON's "Black Magic" Plasma CVD System) have been used to grow graphene<sup>31</sup>, a custom system can provide flexibility and cost savings. For this research I have used two custom designed and built CVD systems: 1) a computer controlled low-pressure tube furnace CVD system, and 2) a high-pressure inductively heated CVD system.

### **2.1. CVD WITH FOUR INCH CHAMBER**

To grow graphene on copper substrates, it was necessary that I build a custom high vacuum thermal chemical vapor deposition (CVD) system. A picture of the CVD system that I built is shown in 2.1. This system is different in several key ways than the low vacuum CVD system I first built to conduct the preliminary studies of graphene growth on copper.

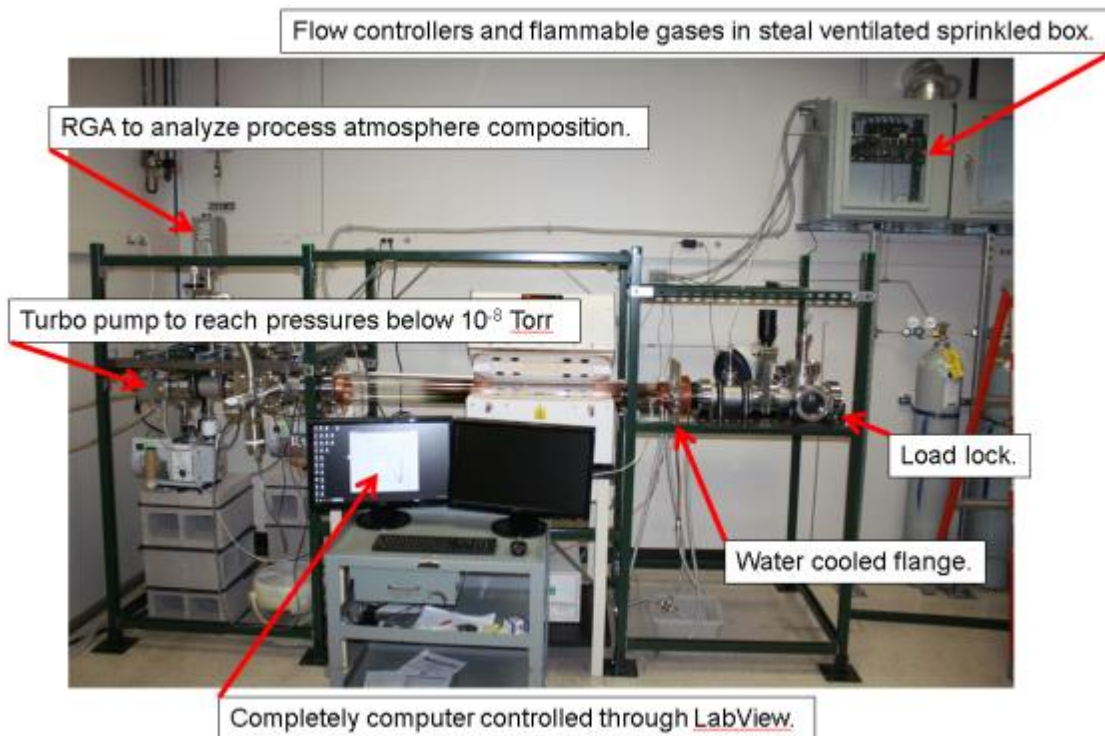


Figure 2.1. Photo of computer controlled and monitored graphene CVD system with 4-inch diameter growth chamber.

First, the system has a turbo pump with a direct line-of-sight to the sample substrate allowing base pressures below  $10^{-8}$  Torr. The original CVD system only had a rotary vane mechanical pump to obtain a vacuum down to  $\sim 10^{-2}$  Torr. To reach high vacuum, not only is a turbo pump used, but, instead of the quick connect flanges used on the previous system, all the flanges on the high vacuum side of the system are conflat flanges, which are capable of achieving ultra-high vacuum (UHV). Reaching lower background pressures allows the removal of undesired residual gasses like water and oxygen from the system before growth. Water and oxygen can etch graphene at high temperature, which changes the graphene's growth and reduces its quality.

The turbo pump also allows the system to reach pressures low enough (below  $10^{-5}$  Torr) to use a residual gas analyzer (RGA). The RGA measures both the composition of the residual gasses in the CVD system – like water and oxygen pressures – and any gasses which may evolve from the substrate during heating – like sulfur dioxide or oxygen. The RGA determines the background, uncontrolled, gasses which might be present in the CVD atmosphere in addition to the purposefully added hydrogen, argon, and methane.

A different tube furnace was also selected for the new CVD system which is not only bigger (with a 4 inch diameter instead of 1 inch) but also maintains a more precise and constant substrate temperature. The power controller of the old system either had the current to the heater all the way on or all the way off. To maintain a given temperature, the furnace coils pulse heat into the system. This results in substrate temperature swings up to 70 °C while the system is supposed to be maintaining a given temperature. The new furnace controller has a phase-angle-fired current controller which allows the power to the furnace coils to not just be either on or off but to be at any power level. With the phase-angle-fired power controller, the furnace is able to maintain a temperature to within 1% of the set point. As can be seen in the temperature profiles in Figure 2.2, the temperature gradient in the center 6 inches of the furnace is less than 10 °C. The 4 inch by 6 inch uniform heat zone allows the growth of either larger samples or many smaller samples at the same time.

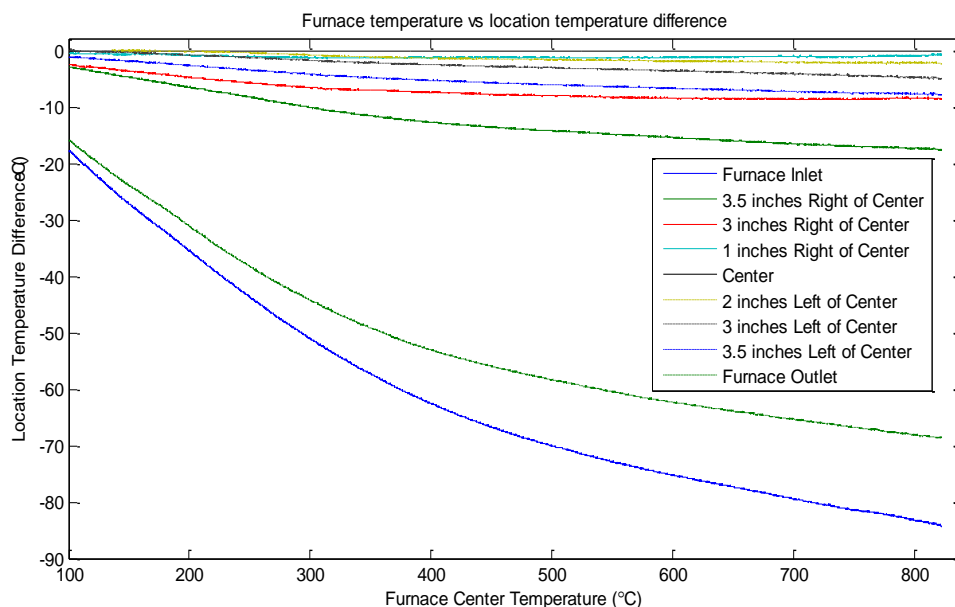


Figure 2.2. The temperature profile of the 4 inch diameter tube furnace.

There are a couple of drawbacks to the larger furnace. First, it takes much longer to heat and cool. The smaller furnace can cool from the growth temperature to a temperature where the sample can be removed within a few hours. The 4 inch furnace takes over 14 hours to cool. This drastically reduces the number of growth runs that can be done in a day and may also affect the quality of the produced graphene films. Second, much more heat radiates out of the sides of the tube furnace. With a 1 inch furnace, the quartz tube is room temperature a few inches away from the furnace even while the furnace is at growth temperatures. This means that no special connectors to the quartz tubes need to be used and no cooling system for the flange connected to the tube had to be developed. However, to keep the flange at the end of the 4 inch quartz tube from getting too hot and starting to leak, a cooling system for the flange had to be devised.

This system ended up having three parts. First, a fan was placed at the end of the tube to blow air over the flange (this had the greatest cooling effect but was not enough on its own). Second, large copper plates were bolted to the flange to work as a heat sink/spreader. Third, copper tubing with chilled water flowing through it was placed not only around the flange but also in direct contact with the quartz tube. Thermal grease was used to get better thermal contact between the quartz tube and the copper tubing. With all three of these cooling methods, the furnace is able to maintain a temperature of 1080 °C indefinitely without the flange overheating and leaking.

A conductance control valve is placed downstream of the graphene growth chamber. The conductance control valve is a motorized butterfly valve which can quickly and accurately change how open the valve is and thus control how fast gas can flow through it (i.e., the gas conductance). This allows the chamber pressure to be controlled independently from the gas flow rates.

The gas flows are controlled by 6 mass flow controllers (MFCs). The MFCs are built by Alicat and are high speed, high accuracy controllers. Five of the controllers are low flow (0 – 10 standard cubic centimeters per minute (sccm)) for flowing hydrogen, methane, <sup>13</sup>C enriched methane, dilute methane, and dilute <sup>13</sup>C enriched methane. The sixth MFC is higher flow (0-200 sccm) and is used for Argon.

Finally, the MFCs, gate valves, conductance control valve, furnace, and RGA are all computer controlled through LabView (Figure 2.3). Being computer controlled allows more precise control of all the growth parameters simultaneously and for them to

be continuously changed. This precision leads to much greater repeatability between growths. All of the system parameters (i.e., chamber pressure, composition, and temperature and gas flow rates) are also recorded ten times a second (much faster and more accurately than they could be recorded by hand).

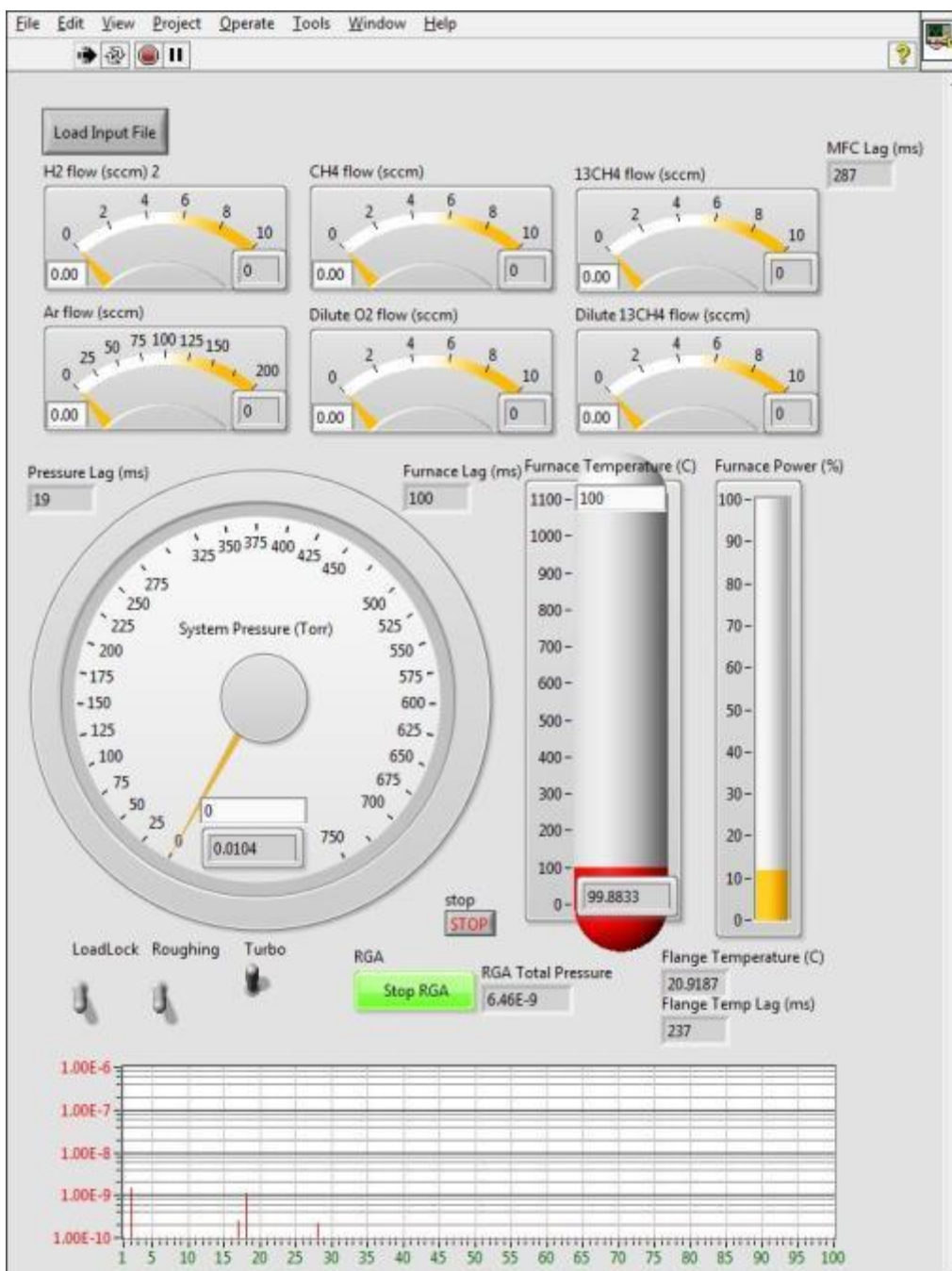


Figure 2.3. The graphical user interface for the LabView programmed CVD system control and monitoring software.

## 2.2. RF INDUCTIVE HEATING CVD SYSTEM

In addition to the 4 inch CVD system that was built by myself, which uses a tube furnace to heat the sample substrate, a CVD system – built largely by Dr. Huifeng Li and Dr. Richard Piner – which uses inductively coupled radio frequency (RF) power to heat the sample substrate, was also used to grow graphene on copper foil.

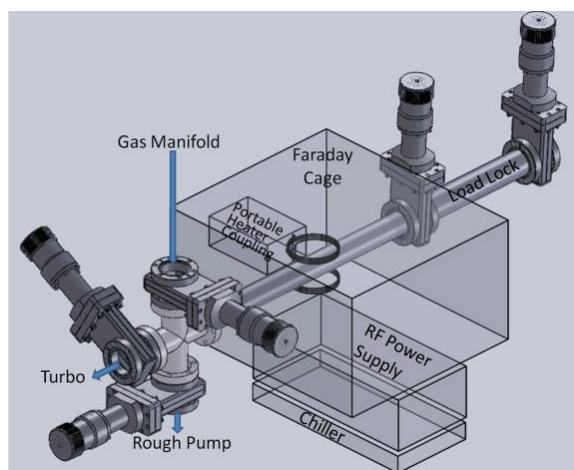


Figure 2.4. Solid works model image of the inductively heated CVD system.

Outside the quartz tube growth chamber is an RF coil that inductively heats only the metal foil by induction. With an optical pyrometer coupled to the RF power supply, precise control of the substrate temperature is possible with a closed-loop proportional-integral-derivative (PID) controller. The turbo pump and high-vacuum-compatible components ensure that the system has very little oxygen and/or water before graphene growth.

There are a few important technical issues with the RF CVD system, which are described below.

- I. The typical RF coil design is a solenoid, but RF heating currents are induced perpendicular to the magnet field. For bulky materials, this is not an issue. However, in the case of a foil, the metal is almost a 2-dimensional conductor. The  $\vec{B}$  field must be perpendicular to the surface of the foil. Although copper has very good heat conductivity, a uniform magnetic field is still required for good heating uniformity. Thus, a coil with Helmholtz-like geometry is used to achieve uniform and efficient heating of the foil.<sup>34</sup> The coils include two circular copper tube coils, each having two turns with a radius of 3.7 cm. The separation between the two coils is 7 cm. The operational frequency is between 230 kHz and 240 kHz. The calculated magnetic field in the common axis direction in the copper foil plane shows that the magnitude of the magnetic field is constant with a 10% variation throughout a 1 inch by 0.5 inch copper foil area. This results in fairly uniform graphene growth on the copper foil in this region.
- II. Small areas of the copper foil substrate can experience a “burn-out” problem where any hot spot of the foil can become even hotter than the other area. The reason for this is that, as in all metals, the resistivity of copper increases with temperature which causes more power to go into the hot spot making it get even hotter (a runaway process) and melt. Figure 2.8 shows a photo of a copper foil that has had a small portion melted

because of this. This undesired localized copper foil melting can be suppressed by increasing the gas pressure to help maintain a constant temperature across the substrate surface.

- III. The 25- $\mu\text{m}$  thick copper foils can have a serious “burn-out” problem, and it is very difficult to control the power to maintain the temperature at the desired set point, possibly because a thin foil has a much smaller heat capacity compared with the supporting quartz tube. By using thicker foils, both the RF coupling efficiency and the thermal stability and uniformity are greatly improved. The calculated skin depth of copper is 135  $\mu\text{m}$  at room temperature and 301  $\mu\text{m}$  at 1035  $^{\circ}\text{C}$ , with an RF frequency of 240 kHz. Therefore, a 125- $\mu\text{m}$  thick copper foil thickness is a good trade-off.
- IV. Since the foil temperature is measured with an optical pyrometer from outside the quartz tube, the tube must be kept clear to allow the laser through to the substrate. At low pressure and high temperature, copper sublimates from the substrate and deposits on the inside of the quartz tube. This copper blocks the line-of-site of the optical pyrometer to the substrate preventing accurate temperature measurement. To prevent this, the system must be at high pressure when the substrate is at high temperature to prevent copper evaporation from the substrate.



Figure 2.5. Photo of a 125  $\mu\text{m}$  thick 2 inch by 0.5 inch copper foil being heated by inductive heating.

### **2.3. PROS AND CONS OF RF AND THERMAL CVD SYSTEMS**

Both the large 4-inch diameter tube furnace CVD system and the inductively heated CVD system have pros and cons over the other.

Thermal CVD system:

**Pros:**

- Large phase-angle-fired controlled furnace allows precise control and uniformity of substrate temperature.
- Computer control gives second-by-second control over process parameters.
- Large samples or many small samples can be grown at once.
- Process gasses and growth atmosphere composition can be changed quickly.
- Attached RGA can monitor the composition of the chamber atmosphere.

**Cons:**

- Large furnace takes ~14 hours to cool from the growth temperature to 100 °C.
- Water cooling is needed to prevent the ends of quartz tube from leaking.
- Large chamber can take hours to pump down to below  $10^{-8}$  Torr.
- Unable to do in-situ high temperature oxidation due to copper depositing on chamber walls.
- System must be kept at low pressure while at high temperature.

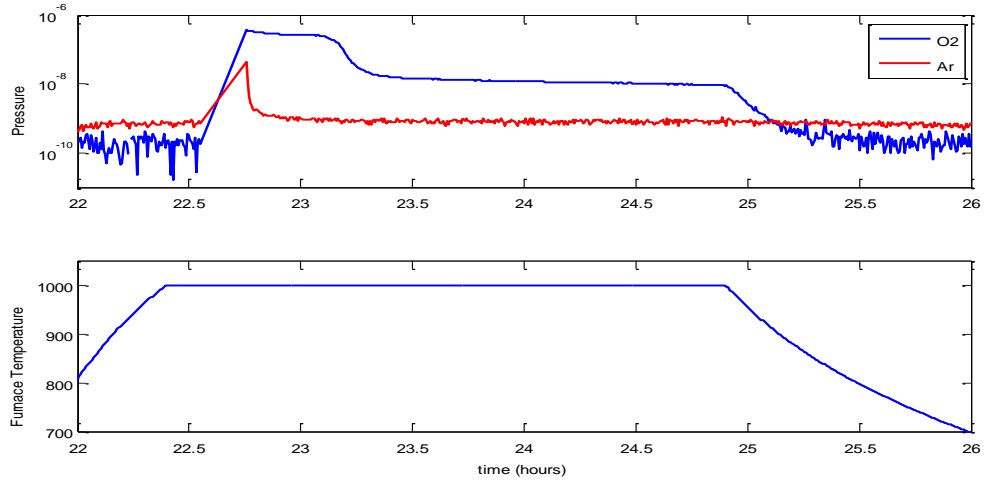


Figure 2.6. The oxygen and argon pressure in the tube furnace CVD system before and after *in-situ* high temperature (1000 °C) oxidation.

Figure 2.6 shows the oxygen and argon partial pressure in the CVD system before and after high temperature substrate oxidation. At 22.6 hours, 0.066 mTorr of 20% oxygen in argon is introduced into the CVD system at 1000 °C for 10 minutes. The argon is then quickly pumped away while the copper substrate continues to reduce and release oxygen at  $\sim 10^{-7}$  Torr. After the sample fully reduces, oxygen continues evolving from the oxidized copper on the inside of the quartz tube in the cold-zone region (Figure 2.7). This region is  $\sim 850$  °C and continues introducing  $\sim 10^{-8}$  Torr oxygen until the furnace is cooled. Because of this unattended continued release of oxygen even after the copper substrate has been reduced, *in-situ* high temperature oxidation of the substrate could not be done in the low pressure tube furnace CVD system.

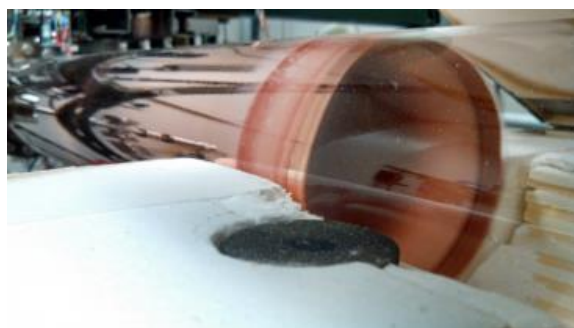


Figure 2.7. Photo of the cold-zone region of the tube furnace with copper deposited on the inside of the quartz tube.

Inductively heated CVD system:

**Pros:**

- Sample can be heated and cooled rapidly.
- Since there is no gas flow during growth, undesired trace gasses are not constantly being introduced into the chamber.
- Small chamber pumps down to below  $10^{-9}$  Torr in the matter of minutes.
- Chamber walls remain cool so no active cooling is required.
- *In-situ* substrate oxidation is possible.

**Cons:**

- There is no gas flow during growth so any evolved gases (e.g. H<sub>2</sub>O, CO, CO<sub>2</sub>, etc.) are not pumped away from the substrate.
- Cannot quickly change between process gases (e.g. from normal methane to <sup>13</sup>C-enriched methane).
- Localized heating can cause portions of the substrate to undesirably melt.
- Only small samples (~1 inch by 0.5 inches) can be made.
- System must be at high pressure when at high temperature.



Figure 2.8. Photo of copper foil after localized melting in the inductively heated CVD system.

## Chapter Three: Substrate Pre-growth Preparation<sup>†</sup>

### 3.1. THE CHALLENGE OF GETTING A CLEAN PRE-GROWTH SUBSTRATE

Since Li *et al.* published the growth of graphene on copper via chemical vapor deposition (CVD)<sup>14</sup>, there has been extensive research in the understanding of the basic growth mechanism of graphene and to extending the two-dimensional growth observed on copper to other metal surfaces, as well as to dielectric surfaces<sup>11</sup>. While much progress has been made in growing large-area graphene films<sup>35-44</sup>, more is required before extremely high quality wafer-scale single-crystal graphene can be achieved. One bottleneck in synthesizing large-area graphene grains is that it has been difficult to decrease the number of nucleation sites. Ideally, as in the classical case of bulk single-crystal growth, a single nucleation site is all that is needed to initiate growth of single-crystal graphene. This assumption is valid as long as the interaction between the substrate and graphene is weak, such as the case for graphene on copper. Another approach for producing large area crystalline graphene, is to grow the graphene epitaxially. However, the high costs of the single crystal metal substrates makes this technique prohibitively expensive for most applications. A number of studies have been done to attempt to understand the nucleation of graphene on Cu, however there has not

---

<sup>†</sup> Portions of this section have been accepted for publication as Carl W. Magnuson, Xianghua Kong, Hengxing Ji, Cheng Tan, Hui Feng Li, Richard Piner, Carl A. Ventrice, Jr., and Rodney S. Ruoff; Copper Oxide as a ‘Self-cleaning’ Substrate for Graphene Growth. *Journal of Materials Research* **2014** accepted

been wide application of this understanding and there are many aspects that could influence nucleation that have not been evaluated<sup>36-37, 40, 45-47</sup>. Some techniques have been used since the discovery of graphene growth on Cu, *e.g.* hydrogen annealing, electrochemical polishing, etching in acid solutions *etc.*, to create a clean copper surface, with some success. It is found, however, that even long, high temperature annealing under hydrogen still leaves carbon on the copper surface<sup>48</sup>. Figure 3.1 shows that not only graphene on the copper surface can survive a high temperature anneal under hydrogen, but so can the carbon deposited as the result of electron beam induced deposition (EBID) during SEM use<sup>49</sup>. In addition, there is a recent report that graphene etching in hydrogen is caused by trace amounts of oxygen in the hydrogen source gas rather than the hydrogen itself<sup>50</sup>. Kim *et al.* suggest that “we should consider that this residual carbon might perturb growth”<sup>48</sup>. My results show that the residual carbon not only perturbs growth but promotes graphene nucleation, as well.

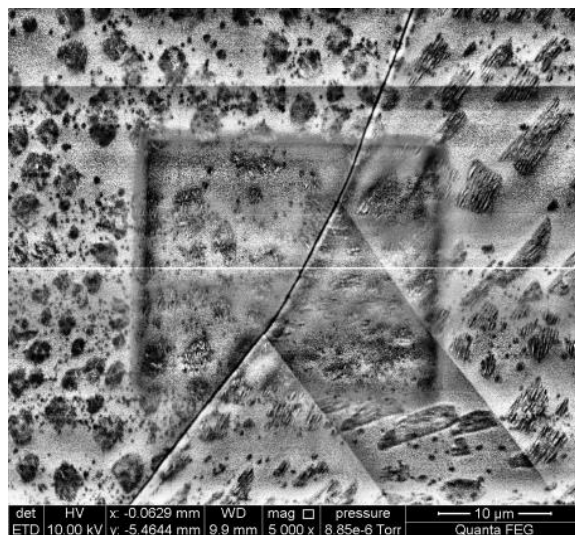


Figure 3.1. SEM image of a copper foil with a sub-monolayer of graphene after being annealed under 700 Torr 5% hydrogen in argon at 1030 °C. Not only are the graphene islands still present, but the electron beam induced deposition (EBID), from looking at the sample with SEM prior to annealing, is also still present.

The challenge of getting low nucleation density, and thus large graphene grains, relies on reproducibly obtaining a clean copper surface free of the adventitious carbon or other carbon sources before methane is introduced into the CVD system. Obtaining a perfectly clean surface *ex situ* in a perfect clean room environment, free of any dust or hydrocarbons, still would not prevent carbon from being on the surface before growth since carbon monoxide is reported to form a carbon layer on copper even at room temperature (which becomes graphitic at 300 °C)<sup>51</sup>. To eliminate any preformed graphene nucleation sites, the substrate must be cleaned *in situ* just prior to graphene growth. Some other metals used as substrates for growing graphene, like iridium and

ruthenium, are already commonly cleaned *in situ* at high temperatures by introducing a small amount of oxygen which ‘burns off’ any remaining carbon contaminants<sup>27</sup>.

It is reported here that copper with an oxidized surface, including cuprous oxide ( $\text{Cu}_2\text{O}$ ) and cupric oxide ( $\text{CuO}$ ), can act as a ‘self-cleaning substrate’ for graphene growth by CVD. Both  $\text{Cu}_2\text{O}$  and  $\text{CuO}$  thermally decompose into metallic copper below copper’s melting point at low oxygen partial pressures and release oxygen from the substrate surface. With the assistance of a residual gas analyzer (RGA), it was found that the released oxygen is free to react with the carbon residues on the copper surface and forms carbon monoxide and carbon dioxide, leaving a clean copper surface apparently free of carbon for large-area graphene growth.

### 3.2. EXPERIMENTAL DETAILS

*Normal copper foil cleaning method:* after rinsing with acetone, copper foils were dipped into acetic acid for 2h and then dried with nitrogen. Electropolishing was done in a homemade electrochemistry cell as reported previously<sup>52</sup> with the acetic acid cleaned Cu foil (25- $\mu\text{m}$  thick Cu foil, 99.8% , Alfa Aesar NO. 13382; 125- $\mu\text{m}$  thick Cu foil, OFHC, Eagle Brass, C10200) as the anode and a large Cu plate as the cathode.

*Copper oxidation was performed in a Ney Vulcan 3-550 box furnace.* Cu foils were heated to 250 °C or 300 °C (heating the substrates much above 250 °C heavily oxidizes the copper which then takes a long time to fully reduce in the CVD system) under

ambient atmosphere at 1 degree per minute and immediately allowed to cool, at 1 degree per minute in the box furnace, to room temperature.

*All residual gas analysis experiments were conducted in a high-vacuum CVD system with a 10 cm diameter quartz tube chamber equipped with a turbopump to reach vacuum levels compatible with the RGA (A vacuum pressure of  $10^{-8}$  Torr was reached at 100 °C before heating the system further). The entire CVD system has a 10 cm inner diameter and is 2.5 meters long. Gas analysis was done by a Stanford Research Systems Quadrupole Residual Gas Analyzer (SRS RGA100) which is located next to the turbo pump inlet 1.5 meters from the furnace center.*

*Scanning electron microscopy (SEM) images were acquired with an FEI Quanta-600 FEG Environmental SEM using an acceleration voltage of 30 kV. Raman spectra (WITec Alpha 300 micro-Raman imaging system) were obtained using a 488 nm wavelength incident laser.*

### **3.3. DATA AND RESULTS**

First, the effect of the normal cleaning methods and the resulting graphene nucleation density and domain size was studied. Two kinds of commonly used commercial Cu foils were chosen, the non-oxygen-free copper [hereafter referred to as oxygen-rich (OR) copper, 25- $\mu\text{m}$  thick, 99.8% , Alfa Aesar No. 13382] and the oxygen-free-high-conductivity (OFHC) copper (125- $\mu\text{m}$  thick, Eagle Brass, 99.99% C10200) for comparison. Both copper foils were thoroughly cleaned with acetone and acetic acid shortly before a high temperature annealing with hydrogen. Figure 3.2a and Figure 3.2b

show that indeed residues – likely carbon since Raman spectra taken from the residue on the OFHC copper had both D and G peaks - remained on both copper surfaces after annealing at 1040 °C for 1h with hydrogen flowing (10 sccm), although much less is on the OR copper compared to on the OFHC copper. This is attributed to the oxygen present in OR copper.

To measure and compare the graphene nucleation density and the resulting domain size on the two kinds of Cu foils after normal cleaning and hydrogen protected annealing,  $^{13}\text{C}$  methane was used for the first 5 mins of growth, followed by growth with normal methane, which is composed predominately of  $^{12}\text{C}$ . The as-grown graphene islands then have  $^{13}\text{C}$  at their centers with a Raman G-peak position of  $\sim 1525\text{ cm}^{-1}$  and normal graphene surrounding the  $^{13}\text{C}$  region with a G-peak at  $\sim 1585\text{ cm}^{-1}$ <sup>53-55</sup>. Raman maps of graphene grown in the same system at the same time following the same cleaning process show that the graphene islands on the commonly used 99.8% OR copper foil are  $\sim 20\text{ }\mu\text{m}$  across, compared to the  $\sim 2\text{ }\mu\text{m}$  graphene domains on the OFHC copper foil (Figure 3.2c and Figure 3.2d). Since the main difference between the two copper foil substrates is that one is oxygen free while the other is not, copper oxides were used to mimic the 99.8% copper and found that this yielded still lower nucleation densities. Nucleation density on copper oxides is dramatically decreased and millimeter-sized graphene islands are readily achieved on the thermally reduced pre-oxidized copper surface.

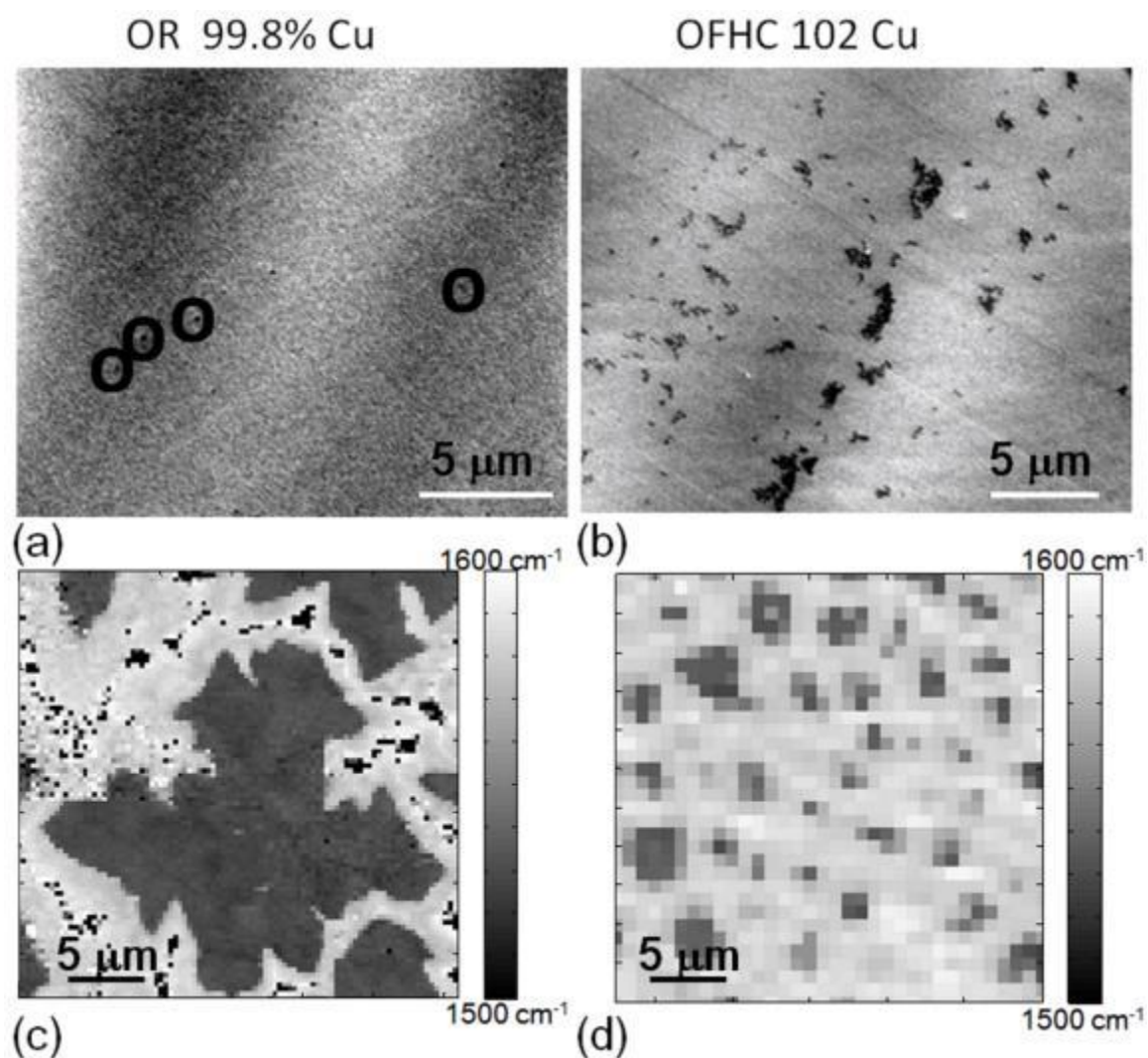


Figure 3.2. SEM images of (a) 99.8% Cu foil and (b) OFHC Cu foil surfaces after cleaning with acetone, acetic acid, and annealing at 1040 °C for 1 hour under 10 sccm H<sub>2</sub> showing differing amounts of surviving carbon residue. Four of the small remaining residue spots have been circled in Figure 3.2a. Maps of the Raman G-peak position for graphene grown on (c) 99.8% copper and (d) OFHC copper.

Copper can be readily oxidized and forms Cu<sub>2</sub>O and CuO after heating in air<sup>56-58</sup>. The copper substrates were oxidized in a box furnace under ambient atmosphere. The

surface of the oxidized copper foil becomes dark brown (cuprous oxide) when heated to 250 °C and then black (cupric oxide) when heated to 300 °C, for the heating time used.

CuO is reported to thermally decompose to Cu<sub>2</sub>O under vacuum around 350 °C<sup>59</sup>. Cupric oxide and cuprous oxide can be distinguished from each other not only by color but also by Raman spectroscopy<sup>60-61</sup>. Figure 3.3 shows the Raman spectra from the surface of OFHC copper foil after having been oxidized at 300 °C to form cupric oxide and then after being thermally reduced to cuprous oxide under vacuum at 600 °C. Although Cu<sub>2</sub>O is stable and solid at atmospheric pressure up to 1230 °C, well above the melting point of copper (1085 °C), it will thermally decompose into metallic copper below copper's melting point at low oxygen partial pressures (below  $\sim 10^{-6}$  Torr at 1000 °C based on this experimental data). Figure 3.3 also shows the Raman spectra of the cuprous oxide sample after being thermally reduced to metallic copper under vacuum at 1000 °C.

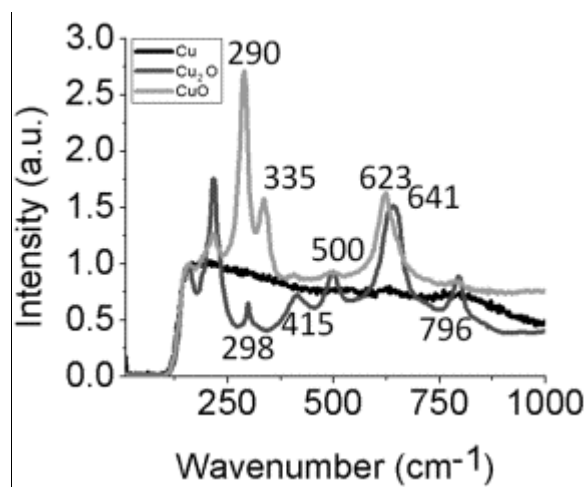


Figure 3.3. Raman spectra from the same copper sample after being oxidized at 300 °C (CuO), vacuum annealed at 600 °C (Cu<sub>2</sub>O), and vacuum annealed at 1000 °C (Cu).

To show the relationship between the oxygen partial pressure and temperature during the decomposition of copper oxide, a 50 mm square piece of the as-oxidized 125- $\mu\text{m}$  thick OFHC Cu foil was placed in the CVD system and the system was pumped down to  $\sim 10^{-8}$  Torr. The system with the pre-oxidized copper oxide substrate was heated to 1080  $^{\circ}\text{C}$  and then immediately allowed to cool. While heating and cooling, the composition of the CVD chamber atmosphere was measured downstream of the sample using an RGA. Figure 3.4 shows the oxygen partial pressure versus temperature as the sample was cooled. As the temperature increases, the cuprous oxide will thermally decompose even at higher oxygen pressure. This temperature/pressure profile was quite reproducible between copper pre-oxidation levels and cooling rates. The logarithmic relationship between the oxygen partial pressure and temperature (as shown in Figure 3.4) fits well with previously published results<sup>62</sup>. It is noted that this data fits almost exactly with that of Kodera *et. al.* but only if  $^{\circ}\text{C}$  is used instead of K in their reported data. More recent work has shown the earlier reports including that of Kodera *et. al.* drastically over estimated the oxygen solubility in copper<sup>63</sup>. In fact, Kodera *et. al.* over estimate the oxygen pressure for the other metal oxides measured in their work – which they also mention in their publication.

If the substrate is too lightly oxidized, the oxygen pressure will drop prematurely due to the substrate becoming completely reduced (this is the case of the 99.8% Cu foil from Alfa Aesar, which reaches a maximum oxygen pressure around 1020  $^{\circ}\text{C}$  with no detectable oxygen in the system by  $\sim 1050$   $^{\circ}\text{C}$  Figure 3.5d). While the oxygen pressure is

dependent on temperature, when the oxygen pressure starts to decrease again depends on the amount of original cuprous oxide in the substrate and the temperature at which it is being reduced; thus the needed anneal temperature and time to fully reduce all the cuprous oxide is dependent on the substrate and can vary from substrate to substrate. As expected, heating OFHC copper does not result in an increase in oxygen partial pressure as shown in Figure 3.5c. To be mentioned, ex-situ oxidation followed by vacuum thermal reduction does not noticeably affect the texture or grain size distribution of the copper substrate.

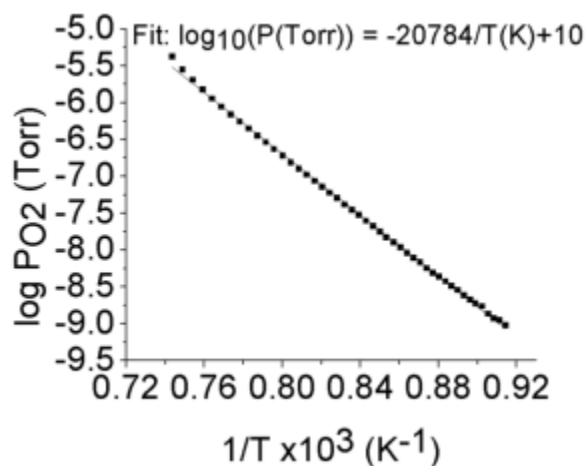


Figure 3.4. Log plot of the partial pressure of oxygen evolving from copper oxide versus inverse temperature while cooling the sample.

Not only is a neat copper surface obtained after thermal decomposition, but oxygen is also released from the substrate surface during this decomposition, which raises the possibility of copper oxides as a ‘self-cleaning’ substrate for graphene growth. Indeed, the released oxygen does react with any adventitious carbon on the copper surface forming carbon monoxide and carbon dioxide; Figure 3.5b shows the CO and

CO<sub>2</sub> partial pressure, along with the O<sub>2</sub> partial pressure, while heating the oxidized copper foil for the first time (The background gas partial pressures from the system chamber have been subtracted so that only the gasses evolving from the substrate are shown in Figure 3.5b). The background pressures remain below  $5 \times 10^{-8}$  Torr and are shown in Figure 3.5a. As the oxygen evolves from the copper oxide, it reacts with the surface carbon forming both a peak in the CO pressure and a corresponding dip in the O<sub>2</sub> pressure around 995 °C. At higher temperature, the CO<sub>2</sub> pressure rises until the surface carbon has been depleted, indicated by a decrease in the CO<sub>2</sub> pressure. How much CO and CO<sub>2</sub> are generated depends on the quantity of carbon residues present on the substrate, and varies between different substrates. To obtain a surface free of carbon, the CO and CO<sub>2</sub> pressures must decrease (indicating that carbon is depleted) before the O<sub>2</sub> pressure decreases due to the copper becoming fully reduced. This is the case for the partial pressures while heating the 99.8% foil shown in Figure 3.5d, where some (but not all) of the carbon is burned off and why there is still some of the likely carbon residue visible in Figure 3.2a. If the substrate is not sufficiently oxidized to provide enough oxygen to fully burn off any surface carbon, then the surface will not be completely clean for graphene growth.

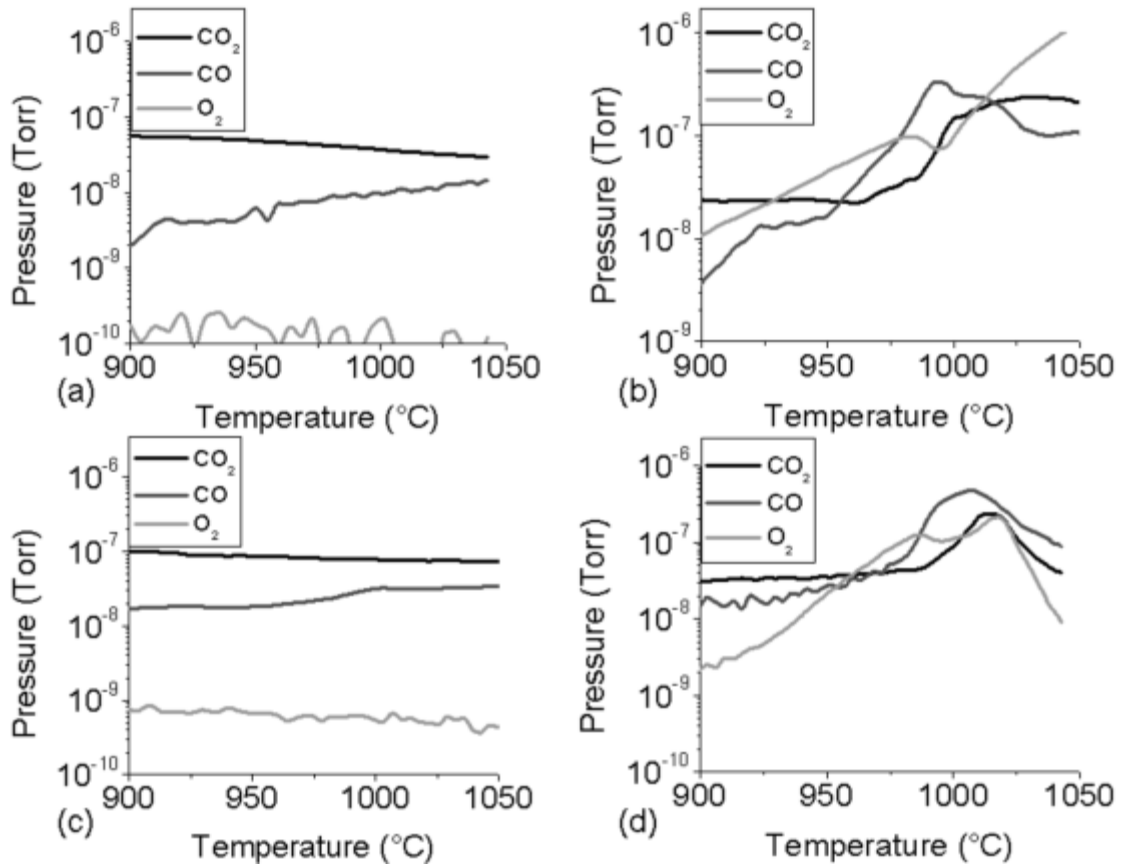


Figure 3.5. The oxygen, carbon monoxide, and carbon dioxide partial pressures in the CVD system versus the furnace temperature upon the initial heating of (a) just the CVD chamber and sample holder, (b) oxidized OFHC copper, (c) OFHC copper, and (d) 99.8% copper.

## **Chapter Four: CNT and Graphene Transparent Conductive**

### **Electrodes**

Transparent thin conductive films (TCFs), also known as transparent conductive electrodes (TCEs), are used in many modern technological devices such as solar cells, lasers, flexible electronics electrodes, displays, etc. The current most widely used material for transparent thin conductive films in liquid crystal, flat panel, and plasma displays is indium tin oxide (ITO). Unfortunately, there are concerns that the world's supply of indium is becoming limited, driving up its cost and limiting its widespread use. The need for a replacement for ITO is an urgent and pressing challenge. US energy consumption continues to rise as well as CO<sub>2</sub> and other greenhouse emissions. It is estimated that the US will release over 5.6 billion metric tons of CO<sub>2</sub> into the atmosphere annually by 2040<sup>64</sup>. The need for widespread use of clean renewable energy sources is apparent not only to meet our energy needs but to protect the earth's environment. Solar cells can help meet both these challenges, but if they are to be deployed on a large scale, they need cheap, plentiful, and sustainable transparent conductive films. Transparent conductive films made from graphene have already been used in tests to replace the ITO screen in Samsung smart phones<sup>65</sup>; however, these are not yet in commercial production.



Figure 4.1. Photos of Samsung smart phone with the one on the left having a graphene based touch screen on the one and the right having a traditional ITO based touch screen<sup>65</sup>.

The work described in this chapter was the result of a close collaboration with Dr. Aruna Velamakanni who devised the chemical fabrication technique. My role was to make all the samples as well as characterize them. To provide a comprehensive picture, I describe also the work by my collaborators (the D-STEM analysis performed by Dr. K. J. Ganesh and the XPS data analysis performed by Dr. Aruna Velamakanni and Dr. Hugo Celio), which resulted in a publication from this work<sup>66</sup>. Thus, I will allude to who did what in the chapter so that it is clear what I contributed.

#### 4.1. SITE-SPECIFIC DEPOSITION OF AU NANOPARTICLES IN CNT FILMS BY

##### CHEMICAL BONDING<sup>‡</sup>

Until this work, there had been no attempt to date to specifically modify the nodes in carbon nanotube (CNT) networks. Prof. Ruoff conceived of this idea: if the nodes can be modified in favorable ways the electrical and/or thermal and/or mechanical properties of the CNT networks could be improved. In an attempt to influence the performance as a transparent conductive film, gold nanoparticles capped with the amino acid cysteine (Au-CysNP) have been selectively attached at the nodes of multi-walled carbon nanotube networks by Dr. Aruna Velamakanni and me. These nanoparticles having an average diameter of 5 nm as observed by TEM. FTIR and XPS were used to characterize each step of the MWCNT chemical functionalization process. The chemical process was designed to favor selective attachment at the nodes and not the segments in the CNT networks (The chemical processing was designed to direct formation of nodes where the gold nanoparticles are). The nanoparticles, which were loosely held in the CNT network, could be easily washed away by solvents, whereas those bound chemically remained. TEM results show that the Cys-AuNPs are preferentially located at the nodes of the CNT networks when compared to the segments. These nanoparticles at the nodes were also characterized by a novel technique called diffraction scanning transmission electron microscopy (D-STEM) confirming their identity. Four-probe measurements found that

---

<sup>‡</sup> Portions of this section have been published as Aruna Velamakanni, Carl W. Magnuson, K. J. Ganesh, Yanwu Zhu, Jinho An, Paulo J. Ferreira, and Rodney S. Ruoff; Site-Specific Deposition of Au Nanoparticles in CNT Films by Chemical Bonding. *ACS Nano* **2010** 4 (1), 540-546

the sheet resistance of the modified CNT networks was half that of similarly transparent pristine multi-walled CNT networks.

## **Introduction**

The overall electrical, thermal, and mechanical performance of networks of overlapped and criss-crossed carbon nanotubes (CNTs) (also called buckytube paper, CNT films, etc.) is largely determined by the nature of the contact at the node—that is, the intersection of overlapping CNTs. There has been no other work to date on selective modification of the nodes in CNT networks, and such an effort is reported here, with an eye towards improving the transparent electrode performance of such networks.

Transparent electrical conductors are a key component in modern technology, used in various applications<sup>67-69</sup> including, but not limited to, solar cells, flat panel displays, solid state lighting, still-image recorders, lasers, optical communication devices, electrodes in flexible electronics, and sensitive bolometers for detecting infrared radiation. Transparent conductive films (TCFs) based on carbon nanotubes are a promising candidate for potential use in all of the above applications and have been touted as a possible replacement for the currently used indium tin oxide (ITO) films. CNT films could offer a lower cost solution that is far more compatible with high volume production techniques, and, unlike metal oxide films, CNT films can be deposited with high volume roll to roll processes. CNT films are far more compliant than brittle metal oxide films, suggesting their use in plastic electronics and solar cells, thus offering interesting possibilities for both fundamental science and important technological areas.

Random or quasi-random networks of CNTs (“CNT nets”) have been made in thin film form and studied for use in applications such as those mentioned above.<sup>67-69</sup>

The application of CNT networks as thin films for TCFs has a major limitation, their relatively high electrical resistance. If the electrical conductivity of CNT nets could be significantly improved, the technological value of these thin films as transparent conductive electrodes would be enormously improved. The overall electrical resistance of CNT TCFs is largely determined by the resistance at the crossing points (also called nodes or junctions) of the CNTs. The CNT network is defined as being comprised of nodes and segments. Modeling studies of networks of one-dimensional elements have shown a resistivity dependence on segment length distributions and node resistances.<sup>70</sup> The electrical resistance at the nodes of CNT networks has been estimated through Monte Carlo modeling to be approximately 100 times larger than the quantum resistance of 6.5 k $\Omega$ —as determined by fitting experimental I-V data of actual CNT nets.<sup>71</sup> Through such modeling it has been shown that if the node resistance value were identical to the quantum resistance, the overall CNT net resistance could be lowered by about a factor of ten.<sup>71</sup> So for the specific types of networks that have been modeled, improvements up to a factor of ten could in principle be achieved if the node resistance were markedly lower.<sup>72</sup> The nature of the bonding at the node also plays a central role in the mechanics of CNT nets, per modeling studies.<sup>73-74</sup> For example, replacing the weak van der Waals contact of two crossing CNTs with strong covalent bonds could significantly improve the mechanical performance, and such a CNT net would be sufficiently robust<sup>75</sup> to be

infiltrated with other materials such as polymers, ceramics, and perhaps even metals. The robust CNT net could then serve in structural applications and would further be capable of being an electrically and thermally conductive component in, e.g., insulating matrix materials, with potential use in smart material applications.

A chemical approach designed by Prof. Ruoff and Dr. Velamakanni is presented for “selectively depositing” functionalized gold nanoparticles at the nodes of multiwalled carbon nanotubes (MWCNTs). Previous work which incorporated gold nanoparticles into MWCNT networks did not target the selective deposition of nanoparticles to be at the nodes of the networks. Methods that lead to a random distribution of gold nanoparticles include solution-based,<sup>76-81</sup> electrostatic,<sup>82</sup> gold evaporation,<sup>83-84</sup> and through the use of  $\gamma$ -radiation.<sup>83</sup> Control on the deposition of gold nanoparticles capped with cysteine (Au-Cys Figure 4.2a) at the nodes of MWCNT networks has been demonstrated here. The main goal of this work is to explore the fundamental science of a method for selective deposition of material at the nodes of MWCNT networks. Following the procedure of chemical linking and annealing, the conductive material (gold nanoparticles) is ensured to be deposited specifically at the nodes and not randomly on the MWCNT films. This will potentially enhance the performance of TCFs based on MWCNTs, and the endeavor of achieving selective deposition at the nodes will hopefully inspire others to find routes to achieving this as well.

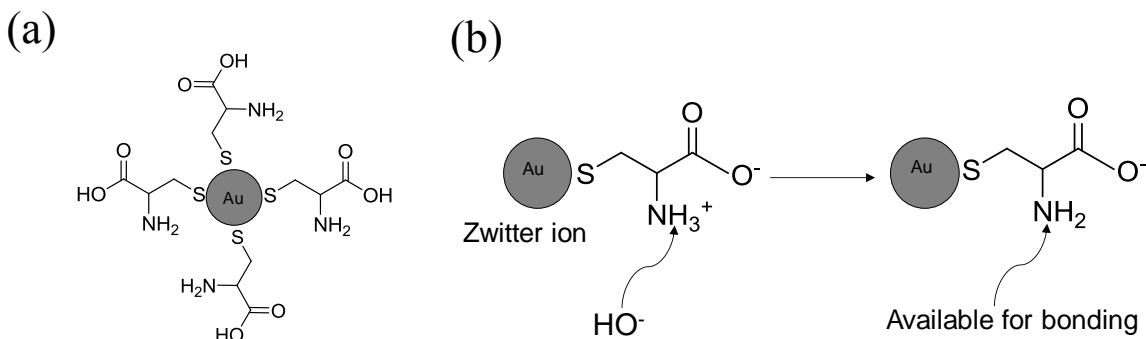


Figure 4.2. (a) Schematic depicting the attachment of cysteine molecules to make Au-Cys nanoparticles. (b) Schematic showing the availability of the  $-NH_2$  group for bonding upon changing the pH by addition of base ( $OH^-$ ) ions.

## Results and Discussions

Cysteine is an amino acid with three functional groups: thiol ( $-SH$ ), amino ( $-NH_2$ ) and carboxylic acid ( $-COOH$ ). While the  $-SH$  group interacts with the gold nanoparticle via the gold-thiol bond, the  $-NH_2$  and  $-COOH$  groups can make chemical bonds with the complementary groups on functionalized MWCNTs. Cysteine at pH 7 is a zwitterion and thus has positive and negative charges on different atoms in the molecule but a net zero overall charge. Specifically, the  $-NH_2$  and  $-COOH$  groups exist as  $-NH_3^+$  and  $-COO^-$  due to migration of a proton from the  $-COOH$  group to the  $-NH_2$  group. However, the pH can be adjusted such that one of those groups can be made available for reaction. In the present work, a weak base, ammonium hydroxide ( $NH_4OH$ ), has been added to adjust the pH to 10 so as to react with the conjugate acid  $NH_3^+$ . Thus  $NH_3^+$  is converted back to a free amino ( $-NH_2$ ) group that is then available for reaction with the

acid chloride (CO-Cl) groups (obtained after multiple steps of functionalization, details in 'Methods' section below) on the MWCNTs. A schematic of this is shown in Figure 4.2b. When one cysteine capped gold nanoparticle (Au-CysNP) gets linked to a MWCNT chemically, the remaining groups on the same Au-CysNP can link to other MWCNTs. This results in a gold nanoparticle 'drawing' two (or more in some cases) MWCNTs together and 'trapping' itself at the resulting intersection or the node of the two MWCNTs. Some Au-CysNPs are not able to link with other MWCNTs, remain at places other than the nodes such as the segments or the endcaps of MWCNTs (see supporting information). It is well known that gold strongly dewets from certain types of carbon nanotubes,<sup>85</sup> thereby tending to minimize their ability to aid in the electrical contacts between tubes. However, the morphological stability of the gold film/nanoparticles depends on the relative strength of the interface bonds (adhesion),<sup>86</sup> and, in the present case, gold nanoparticles are chemically bound to the MWCNTs and hence are more strongly attached than if they were physically adsorbed. Although annealing these films at 400 °C for an hour leads to the decomposition of cysteine into various gaseous products, leaving just the gold nanoparticles at the nodes, the strong covalent bonds by which they were originally attached to the MWCNTs helps them remain at the same position even after annealing and losing the cysteine capping; it has been reported that pure cysteine thermally decomposes at 400 °C also.<sup>87</sup> TEM images, Figure 4.3, after annealing show that the gold nanoparticles do not dewet and are still located at the network nodes.

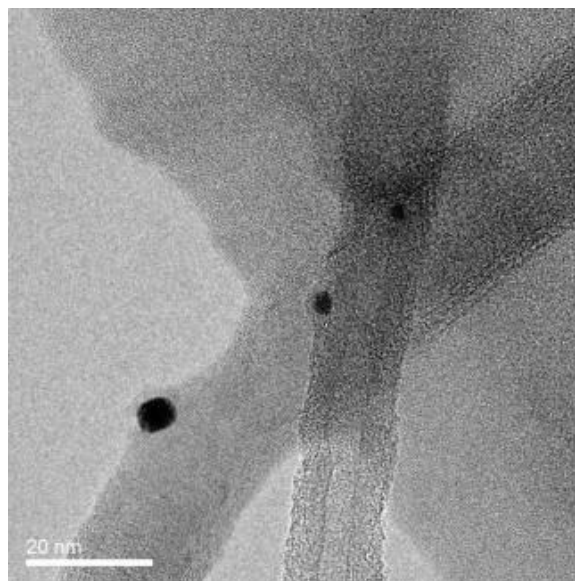


Figure 4.3. TEM image of a post annealed MWCNT-COCl-AyCysNP network. The particles' sizes and positions are the same as before annealing.

Control experiments were conducted where the gold nanoparticles were not capped with cysteine to observe if there was still specificity in linking of the gold nanoparticles. Films were made with these non-cysteine-capped gold nanoparticles following the same procedure used for MWCNT-Au-CysNPs. It was found that the gold nanoparticles agglomerated to larger particles and most of the gold nanoparticles simply did not adhere to the MWCNTs. (TEM and SEM images of networks with Au nanoparticles not capped with cysteine can be found in the supporting information.) The very few nanoparticles that did stay within the network were located randomly on the network as opposed to what was found when they were capped. This is attributed to the lack of cysteine capping around the gold nanoparticles which not only stabilized them

and prevented agglomeration, but also provided complementary groups ( $\text{-NH}_2$  with  $\text{-COCl}$ ) to bond with the functionalized MWCNTs. The Au-Cys NPs were first linked to the tubes and then the films were made. This procedure ensures that the location of gold nanoparticles on MWCNTs is due to the chemical bonds and that they are thus located at positions where they are linking the tubes. When a film is made with such linked tubes, the gold nanoparticles remain at the intersections of the tubes. These intersections are (some of) the nodes of the carbon nanotube networks/films. However, if a film is first made and then the gold nanoparticles deposited, there is very little control on directing the nanoparticles to the junctions, resulting in a random dispersion across the network as evidenced by the TEM results. This remains an exciting challenge for future work—selective deposition at the nodes of already-made CNT nets.

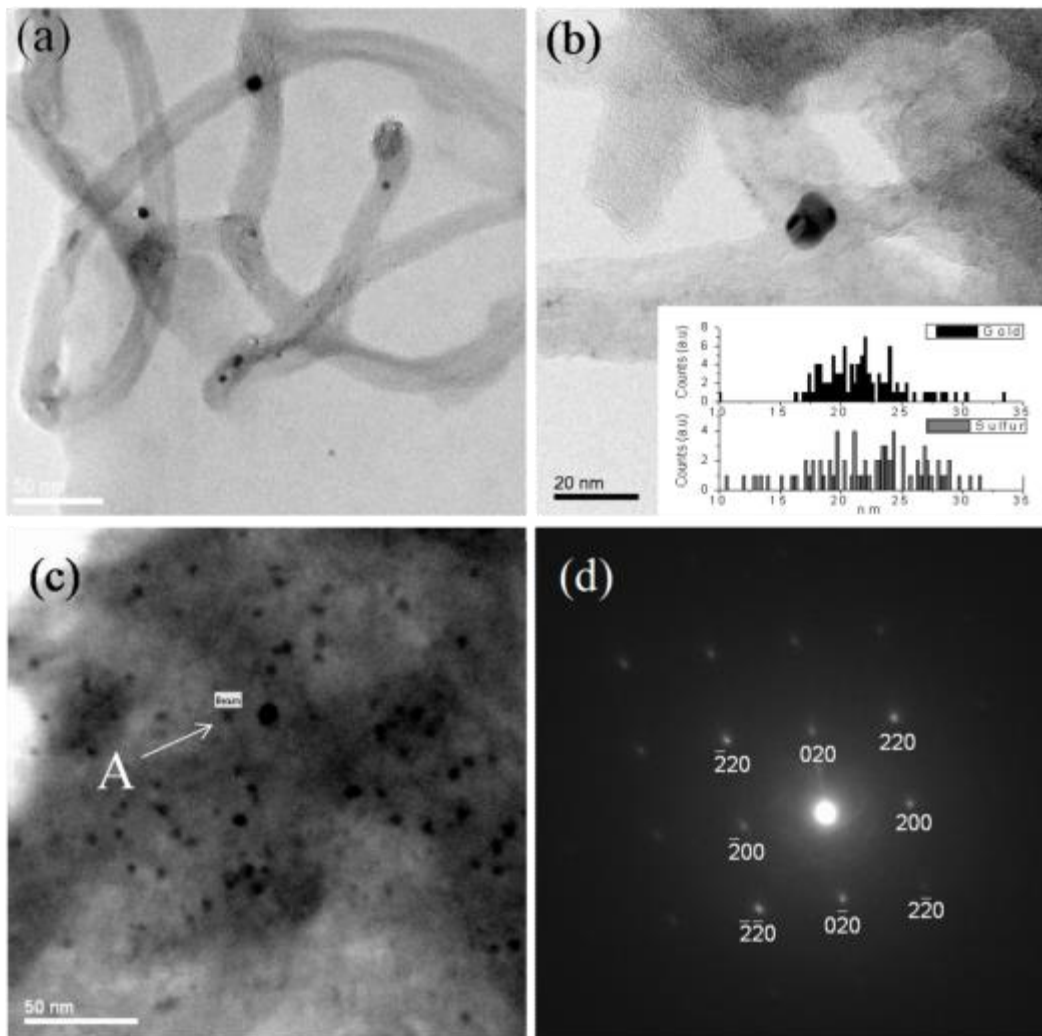


Figure 4.4. (a) Bright-Field TEM micrograph of the MWCNT network showing Au-Cys nanoparticles at the nodes (circled) and one along a segment (squared). (b) A high magnification phase contrast image of one of the nodes. Insert: Micro-EDS line profile for gold and sulfur across the Au-Cys nanoparticle. (c) A bright-field STEM image of the MWCNT network showing the D-STEM beam positioned exactly at one of the Au-Cys nanoparticles labeled 'A'. (d) Spot diffraction pattern obtained by D-STEM from the nanoparticle shown in (c). The bright center spot in the diffraction pattern is (000).

A phase contrast image of a sparse MWCNT-Au-CysNP network is seen in Figure 4.4a. Four different samples were observed and 150 nodes in each sample were analyzed. It was observed that 85% of the particles were at the nodes and the remaining 15% were along the segments. Also many nodes were unoccupied by Au-Cys particles, leaving them as unmodified nodes. Figure 4.4b shows a high magnification TEM image of a Au-CysNP between two MWCNTs. TEM was also used to examine areas of the MWCNT networks that were sparse enough to clearly differentiate between network nodes and segments. Measurement of the linear lengths of the segments and nodes showed that 30% of the overall lengths of the MWCNTs were located at nodes. However, in these areas, 85% of the gold nanoparticles were located at the nodes. If the particles were randomly distributed along the MWCNTs, one would expect only 30% to be at the nodes. This clearly shows that the Au-CysNPs are more selectively deposited at the network nodes. To determine the percentage of the network occupied by nodes, the length occupied by the nodes was divided by the total length of MWCNTs in the network. Figure 4.5 shows an example of how these two lengths were measured. To get the fraction of the MWCNTs that are at the network nodes, the length of the nodes was divided by the length of the nodes plus the lengths of the segments of the MWCNTs. Images of networks containing over 100 nodes were analyzed. It was found that 30% of the lengths were at nodes while 85% of the Au-Cys nanoparticles were located at nodes.

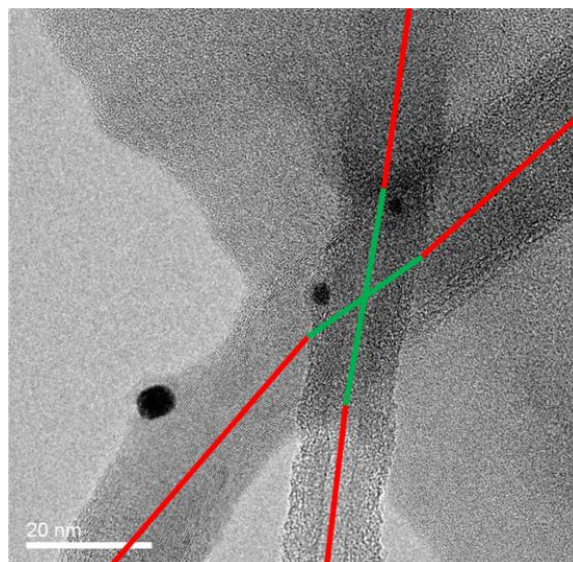


Figure 4.5. TEM image of part of a MWCNT network with gold nanoparticles at a node (image obtained on networks after annealing), where both the segments and nodes of the network could be easily differentiated. The green lines represent the linear length of the MWCNTs occupied by the node and the red lines represent the segments. In this image, 2 of the 3 gold nanoparticles are located at a node (circled).

Using the same TEM sample as in Figure 4.4a, a line scan using micro-EDS across a gold nanoparticle (~5 nm in diameter) located at a node of the MWCNT network revealed that the nanoparticle was coated with a thin layer of sulfur (Figure 4.4b insert) which is due to the gold-thiol linkage. This has also been proven by XPS data as discussed below.

A recently developed technique called D-STEM was also employed by Dr. K. J. Ganesh to identify the material deposited at the nodes. The interest is to characterize just the nanoparticle at the node and not the surrounding material in order to confirm that the

material deposited at the node was in fact a gold nanoparticle. The nanobeam diffraction (NBD) technique was not used to characterize the material at the nodes in spite of having a very small beam size because, during operation, the NBD technique requires constant toggling between the image and diffraction modes, which might result in potential beam shifts, thereby affecting position-accuracy. In D-STEM, the enhanced control and precise positioning of the beam on the region of interest enables rapid collection of sharp spot patterns from nanostructures as small as 3 nm. The details of this technique can be found elsewhere.<sup>88</sup> Figure 4.4c shows a representative bright-field STEM image of a node with a nanoparticle.

In order to accurately determine the identity of the nanoparticles positioned at the nodes by electron diffraction, sharp spot patterns were achieved by using the ‘D-STEM’ technique, which employs a near-parallel illumination with a convergence angle less than 1 mrad in a modified STEM configuration. In any scanning transmission condition, the image resolution is determined by the probe size, and the probe size for low probe defining apertures (low convergence angles) depends on the diffraction limit. Therefore, the probe size in D-STEM (for such low convergence at 200 kV) is  $\sim$  1-2 nm. The modified STEM optics in D-STEM results in uncorrectable distortions of the off-axis beams during the scanning process.<sup>88</sup>

These two factors impair the image resolution (in Figure 4.4b). In conventional STEM, operating at convergence angles of the order of 10-20 mrad, the probe sizes are much smaller, which in turn provides better spatial resolution in real space. However in

reciprocal space, it results in large discs which also suffer from dynamical diffraction effects and disc overlaps that hinder accurate indexing. D-STEM was used to position the probe accurately at the nanoscale feature of interest in the image and simultaneously obtain easily indexable sharp diffraction patterns which prove the location of the nanoparticles and that they are in fact gold Au (0) nanoparticles.

The 1-2 nm diameter near-parallel probe was positioned on the nanoparticle labeled (A), and the diffraction pattern obtained is shown in Figure 4.4d. The obtained four-fold diffraction pattern was indexed to a [001] beam direction and, when compared, the interplanar spacings revealed a perfect match to gold (Au (0)). A single crystal Si [110] specimen was used to calibrate the camera length for this technique.

Figure 4.6a and Figure 4.6b shows the TEM images and Figure 4.6c the SEM image from a control experiment performed to find out if uncapped gold nanoparticles adhere to the MWCNT networks and if adhering, whether they do so in selected regions of the network. The results show that the uncapped gold nanoparticles do not adhere to the network and instead aggregate into larger particles away from the network.

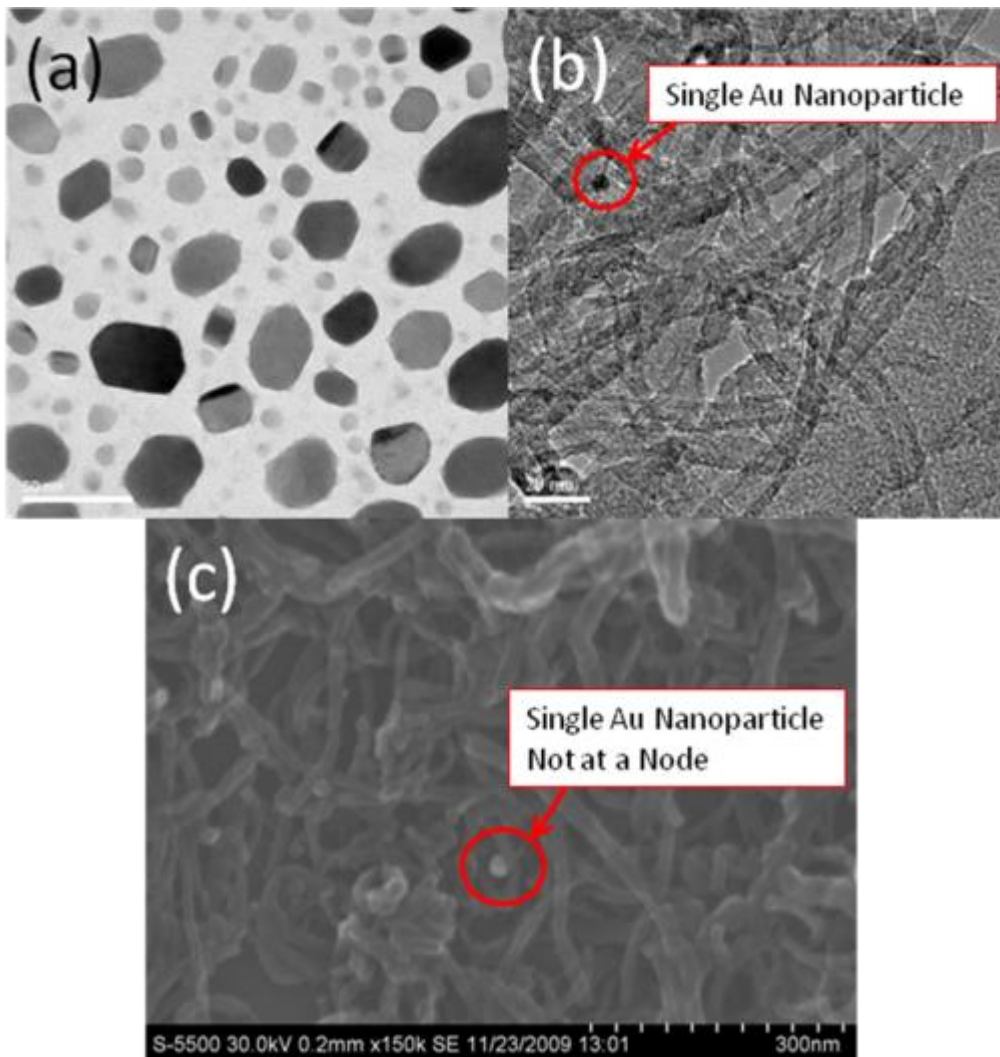


Figure 4.6. (a) TEM image of gold nanoparticles that were not capped with cysteine. The gold nanoparticles were not attached to MWCNTs and their sizes were both larger and their distribution varied more greatly than the gold nanoparticles capped with cysteine. (b) TEM image of a MWCNT network from the same sample as (a). (c) SEM image of a region of a MWCNT network with non-capped gold nanoparticles. Most of the gold nanoparticles are washed away during filtration in the film making process. A remaining particle is not at a network node.

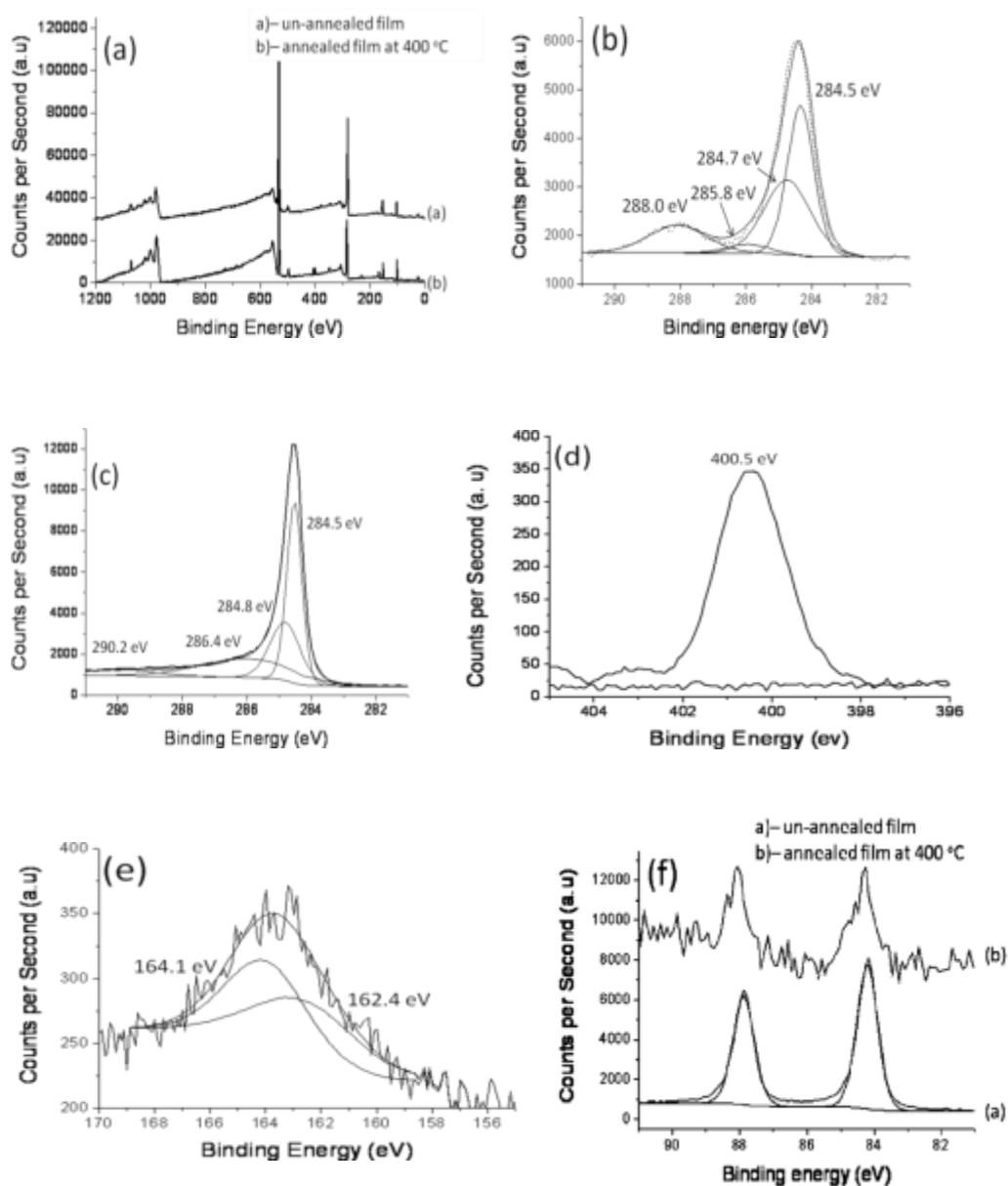


Figure 4.7. (a) XPS survey scan of MWCNT-AuCys films before and after annealing. The peaks corresponding to nitrogen and sulfur disappear after annealing. (b) Deconvoluted C 1s peak for the un-annealed film. (c) Deconvoluted C 1s peak for the annealed film. (d) The N 1s peak (400.5eV) before annealing; disappears after annealing. (e) Deconvoluted S 2p peak. (f) The Au 4f peaks are present both before and after annealing.

XPS data was taken on the samples by Dr. Aruna Velamakanni and me. The data was largely analyzed by Dr. Aruna Velamakanni and Dr. Hugo Celio. Figure 4.7a shows the XPS survey spectra of unannealed and annealed films deposited on glass. The survey spectrum of unannealed film showed peaks for sulfur and nitrogen in addition to gold, carbon, and oxygen. A better insight into the binding of the Au-CysNPs was obtained by looking at the high resolution elemental spectra of the individual elements present. Figure 4.7b shows the C 1s peak for the MWCNT-AuCys films before annealing. This was fit to four components: the component at 288.0 eV corresponds to amide linkage (-NH-C=O), 285.8 eV to -C-O in hydroxyl groups (which get incorporated during oxidation along with the carboxylic groups), and the remaining two peaks at 284.5 eV and 284.7 eV to the  $sp^2$  and  $sp^3$  carbons respectively in MWCNTs. Figure 4.7c shows the C 1s peak for the annealed Au-Cys-MWCNT films. The peaks at 284.5 eV and 284.8 eV correspond to the  $sp^2$  and  $sp^3$  carbons, respectively, in the MWCNTs. The peak at 286.4 eV corresponds to the -C-OH which remains after annealing. It was observed that the other high oxidation peaks disappear, such as the amide in the previous case. Instead, a shakeup peak at 290.2 eV appears. The shakeup peaks which are due to  $\pi \pi^*$  transitions and are more pronounced in the conjugated and aromatic systems and occur above 290 eV.<sup>89-90</sup> In the case of functionalized tubes with Au-CysNPs, the conjugation is largely disrupted due to introduction of  $sp^3$  carbons due to oxidation and chemical bonding. After annealing when the cysteine capping is decomposed (loss of amide bonds) and more  $sp^2$

bonding is attained due to decarboxylation of the MWCNTs, the shake-up peak becomes more prominent as seen in Figure 4.7c. The origin of the N 1s peak at 400.5 eV (Figure 4.7d) is due to the incorporation of the amide bond that is formed by linking the Au-CysNPs to the MWCNTs. A peak corresponding to the amide bond is also seen in the C 1s spectrum at 288.0 eV. The S 2p peak is deconvolved into two components for the unbound thiol due to any free cysteine at 164.1 eV and another peak at 162.5 eV<sup>87, 91-93</sup> due to the gold-thiol interactions. Both the N 1s and S 2p peaks disappeared completely in the annealed films. This is attributed to the decomposition of cysteine into various gaseous products at 400 °C.<sup>87</sup> Figure 4.7f shows the comparative spectra of Au 4f before and after annealing. The Au 4f (7/2) peak has been referenced at 84 eV which is typical of Au (0).<sup>94-95</sup> The Cl 2p peak is absent in both the annealed and unannealed films confirming the absence of AuCl<sub>3</sub>. This eliminated the possibility of other species such as Au<sup>3+</sup> that might also contribute to the signal for Au in XPS. Indexing the D-STEM diffraction pattern from the particles at the nodes proved that these particles are Au (0) and not a compound such as AuCl<sub>3</sub> containing Au<sup>3+</sup>. Hence it can be concluded that Au<sup>3+</sup> is not present, and the signal for gold is in fact coming from Au (0). The incorporation of -Cl in the form of -CO-Cl in the MWCNTs (see supporting information) and attachment of the Au-CysNPs to the MWCNTs has been successfully proven by XPS; this was otherwise very difficult by FTIR due to the limit of detection for that technique, owing to the fact that mild oxidation was used and thus fewer functional groups were introduced.

Figure 4.8a shows the comparative XPS survey spectrum of the pristine MWCNTs, MWCNT-COOH and MWCNT-COCl samples. The MWCNT-COOH sample shows an increase in the oxygen peak and the MWCNT-COCl sample shows a peak for Cl 2p indicating that the MWCNT-COOH functionalized tubes have been converted to MWCNT-COCl. Figure 4.8b shows the high resolution Cl 2p spectrum of the MWCNT-COCl sample at 199.5 eV that is indicative of a C-Cl bond incorporated due to the formation of CO-Cl bonds.

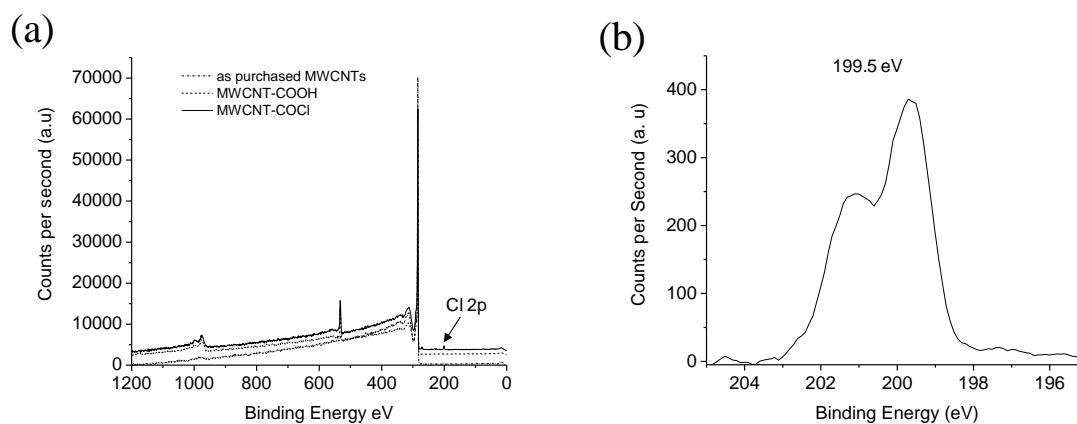


Figure 4.8. (a) Comparative survey spectra of as-purchased (dashed), MWCNT-COOH (dotted), and MWCNT-COCl (solid) samples. The MWCNT-COOH sample shows a clear increase in the oxygen content and the MWCNT-COCl sample shows a peak for Cl 2p. (b) The Cl 2p peak at 199.5 eV is indicative of a C-Cl bond that is incorporated due to the formation of CO-Cl bonds.

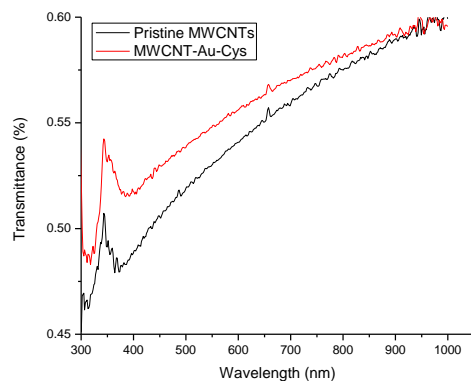


Figure 4.9. Transmittance plot of films made from both pristine MWCNTs and MWCNT-Au-Cys. At 550 nm, the transmittance of the pristine MWCNT network is 53.1% and the MWCNT-Au-Cys network is 54.8%.

The van der Pauw four probe method<sup>96</sup> was used to measure (Keithley 6221 and 6514) the sheet resistivity of the vacuum-filtered films after they were transferred onto glass substrates. The resistivity of four films from the same MCE membrane before annealing was  $\sim 580 \text{ k}\Omega/\square$ . After annealing under argon at 400 °C for one hour, the resistivity of the thin conductive films dropped to  $19.5 \text{ k}\Omega/\square$ . The transmittances of the same films (Figure 4.9) measured at 550 nm with a spectroscopic ellipsometer (J. A. Woollam M2000D) were found to be  $54.8 \pm 0.3\%$ . Four TCFs made with pristine MWCNTs from the same MCE membrane with transmittance  $53.1 \pm 0.2\%$  were found to have a sheet resistance of  $41 \text{ k}\Omega/\square$ . Even though the pristine MWCNT TCFs were slightly less transparent than the modified films, their sheet resistance was over twice as large. Annealing the TCFs for one hour at 400 °C under argon did not change their

transmittance, nor did it change the sheet resistance of the pristine MWCNT films. (I-V curves of all three types of films can be found in Figure 4.10.)

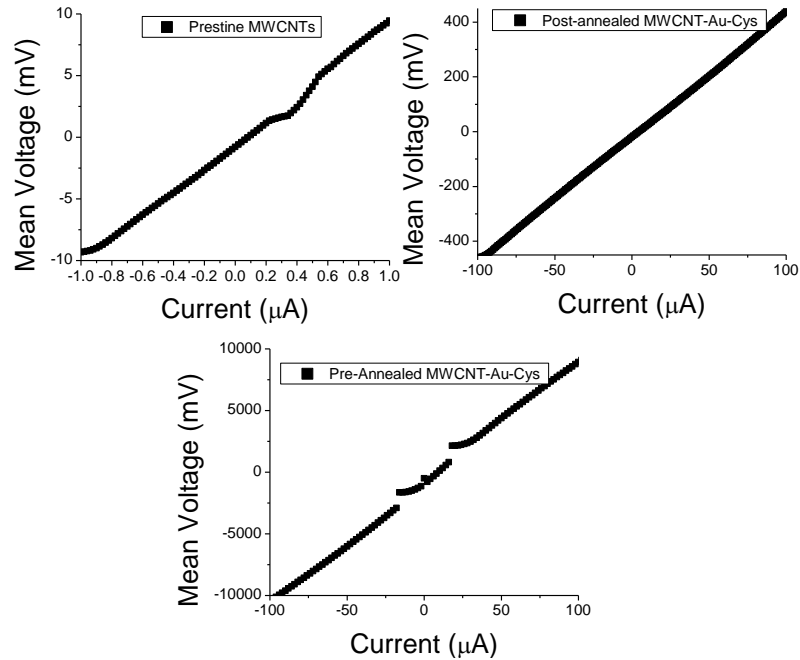


Figure 4.10. I-V plots for the thin films made with pristine MWCNTs and MWCNT-Au-Cys before and after annealing. The non-linearities in the curves are an artifact of the characterization setup, not a property of the films. When the current supply changes between the high and low current regimes, the actual current is lower than reported causing dips in the I-V curves. To obtain the sheet resistance the slope of the I-V curve is multiplied by  $\pi/\ln 2$  ( $\sim 4.5$ ). From the slope of these I-V curves, the sheet resistance of the films was determined to be  $41 \text{ k}\Omega/\square$  for the pristine MWCNT film,  $580 \text{ k}\Omega/\square$  for the pre-annealed MWCNT-Au-Cys film, and  $19.5 \text{ k}\Omega/\square$  for the post-annealed MWCNT-Au-Cys film.

## Conclusions

Au-CysNPs were incorporated selectively at the nodes of CNT networks. These nanoparticles are chemically bound to the MWCNTs via amide bonds and are preferentially located at the nodes of the MWCNT network rather than along the segments. Since the weak van der Waals contact of two crossed CNTs has been successfully replaced by strong covalent bonds, the mechanical performance of the CNT net might also be improved, and is thus suggested as a topic of further study. The electrical resistivity of TCFs made with MWCNT-Au-Cys is roughly half that of those with the same transmittance but composed of pristine MWCNTs alone. This is the first report of an experimental attempt to selectively modify the nodes and not the segments of CNT networks so as to enhance the performance of such networks. The concept of selective modification of the nodes in CNT networks is a topic of a recent patent filing by one of the authors.<sup>97</sup> A recent publication (appearing after the submission of the work presented here) by Rodríguez-Manzo et al.<sup>98</sup> explored irradiating a cobalt nanoparticle located near the node of two MWCNTs to “nano-weld” the MWCNTs together, with a focused electron beam in a TEM at elevated temperatures. Using a similar method of selectively depositing nanoparticles at the nodes of MWCNT networks as shown in the work here for the deposition of cobalt nanoparticles and then “nano-welding” the MWCNTs en masse such as might be achieved through large area irradiation, is suggested for future research.

## Methods

Acid functionalized MWCNTs (MWCNT-COOH): Multi-walled carbon nanotubes (Sigma Aldrich 99.97% pure 6-13 nm in diameter) were annealed at 225 °C for 24 hours in air to remove any amorphous carbon and oxidize any catalyst particles. The annealed MWCNTs were then oxidized to generate –COOH functional groups by stirring with a mixture of concentrated sulfuric and nitric acid (3:1)<sup>99</sup> for 24 hours. Stirring was used instead of sonication in an attempt to prevent the nanotubes from breaking at the end caps. The endcaps of the MWCNTs will open if harsh oxidizing conditions, such as high temperature treatment and/or sonication, are used. To prevent this, mild oxidation conditions, such as stirring the MWCNTs in H<sub>2</sub>SO<sub>4</sub>+HNO<sub>3</sub> (3:1) at room temperature, were used rather than sonication. This approach results in the retention of end caps as seen in the TEM image below (Figure 4.11a-c). The oxidized MWCNTs (MWCNT-COOH) were vacuum filtered (Millipore 1.0 micron PTFE) and thoroughly rinsed with deionized water (17.5 MΩ Barnstead).

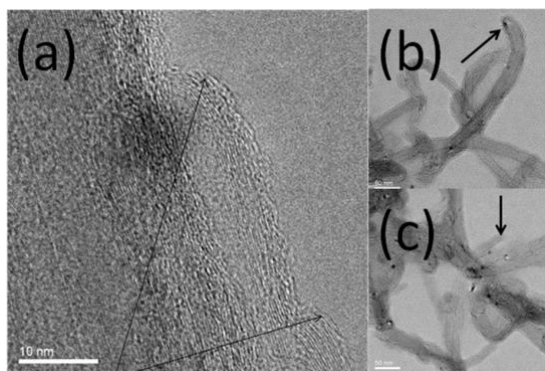


Figure 4.11. (a) TEM images showing intact endcaps on oxidized MWCNTs before functionalization with  $-\text{COCl}$  groups. The dark spot is not a gold nanoparticle but is due to mass thickness contrast. (b) and (c) show intact endcaps with and without gold nanoparticles respectively. (Scale bars in (b) and (c) are 50 nm.)

Acid chloride functionalized MWCNTs (MWCNT-COCl): 100 mg MWCNT-COOH was stirred in 50 ml thionyl chloride with 2 drops dimethylformamide (DMF) as a catalyst, under argon for 24 hours at 70 °C. The functionalized MWCNTs were vacuum filtered (Millipore 1.0 micron PTFE) and completely rinsed with tetrahydrofuran (THF) to prevent hydrolysis of the  $-\text{COCl}$  functional groups. The acid chloride functionalized MWCNTs (MWCNT-COCl) were stored under argon to prevent any hydrolysis and were used immediately for further reactions.

Synthesis of gold nanoparticles (Au-CysNPs): Cysteine capped gold nanoparticles (Au-CysNPs) were prepared by a known method.<sup>100</sup> Briefly, reduction of tetrachloroauric acid with sodium borohydride, followed by addition of the amino acid cysteine, resulted in Au-CysNPs. The Au-CysNPs dispersed in water were purified to a diameter of 3-5 nm by centrifuging (IEC MediSpin) for one hour. 1 ml ammonium

hydroxide was diluted with 100 ml H<sub>2</sub>O. The pH of 10 ml Au-CysNPs was adjusted to 10.4 (measured with a Fisher Scientific Accumet Excel pH meter) by adding 6 drops of the diluted ammonium hydroxide.

Figure 4.12 shows the UV–Vis spectra of gold hydrosol (obtained by sodium borohydrate reduction) and also of Au-Cys<sup>100</sup>. The strong absorption at 512 nm is the characteristic gold plasmon resonance. The spectra of Au-Cys nanoparticles showed a red shift and broadening of the above band indicating some aggregation as a consequence of surface modification. The interaction of cysteine with the gold nanoparticles was also seen by a rapid change in the color of the solution from ruby red to blue on addition of cysteine to the gold hydrosol.

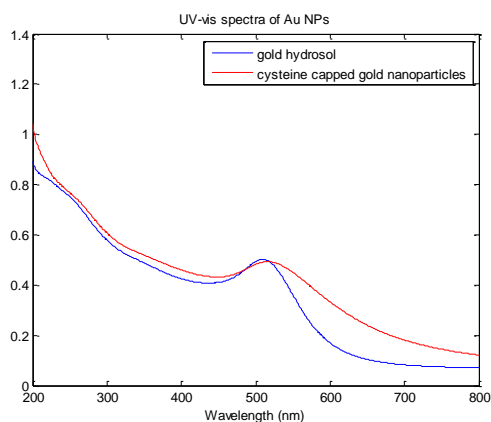


Figure 4.12. UV spectra of the gold hydrosol and of the cysteine capped gold nanoparticles.

FT-IR spectra were employed in an attempt to detect the characteristic bands of MWCNTs with different functional groups and the cysteine moiety after gold nanoparticle conjugation. Figure 4.13a represents the FTIR spectrum of acid functionalized MWCNTs (MWCNT-COOH). The IR spectrum shows a very small peak at  $3500\text{ cm}^{-1}$  characteristic of the  $\text{-OH}$  stretch region from carboxylic acids. MWCNTs are treated with strong acids ( $\text{H}_2\text{SO}_4+\text{HNO}_3$ ) to introduce oxidation. The FTIR of acid chloride functionalized MWCNTs (MWCNT-COCl), Figure 4.13b, shows a clear decrease in the intensity of the  $\text{-OH}$  stretch that indicates the conversion of  $\text{-COOH}$  groups to  $\text{-COCl}$ . This is also indicated from XPS data as discussed above. Figure 4.13c represents the MWCNT-COCl linked with Au-Cys nanoparticles. It shows a characteristic stretch from the amide bond at  $3300\text{ cm}^{-1}$  corresponding to the amide bond formed as a result of the linking of cysteine capped gold nanoparticles (Au-Cys) to the MWCNT-COOH (MWCNT-AuCys).

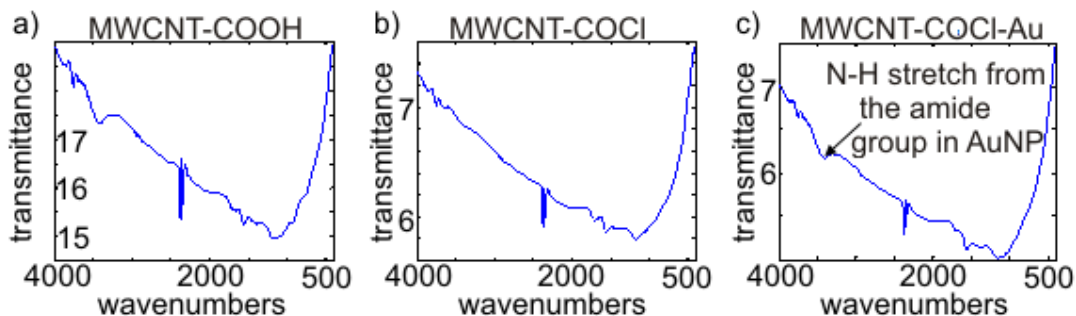


Figure 4.13. FTIR spectra of acid functionalized a) multiwalled carbon nanotubes (MWCNT-COOH), b) MWCNTs (MWCNT-COCl), c) MWCNTs linked with Au-Cys (MWCNT-Au-Cys).

Linking of Au-Cys with MWCNT-COCl (MWCNT-AU-CysNPs) and making films: 20 mg of MWCNT-COCl was suspended in 10 ml THF and 1 ml of the pH-adjusted Au-CysNPs was added drop-wise while stirring under argon. The reactive -COCl groups on the MWCNT-COCl react with the free -NH<sub>2</sub> groups on the Au-CysNPs and are linked via an amide bond. The MWCNTs linked with Au-CysNPs (MWCNT-Au-Cys) were suspended in THF and stirred under argon for 2 days. The solution was then added to 190 ml pure water. This hydrolyzed the remaining -COCl functional groups on the MWCNTs and created a good dispersion of the MWCNT-Au-CysNPs. After decanting the above solution, 6 ml of the supernatant were suspended in 200 ml pure water and vacuum filtered onto a mixed cellulose ester (MCE) filter membrane (Sterlitech) and made into a thin film.<sup>101</sup> To obtain square films, each 47 mm diameter MCE membrane was cut into four smaller squares roughly 1 cm on a side. The film was transferred to a glass cover slide, and the MCE membrane was dissolved with acetone

(soaked three times in an acetone bath for 20 minutes). After rinsing the thin conductive film with ethanol several times, which was observed to wash the unbound nanoparticles away, the film was annealed at 400 °C for 1 hour under argon. The result is uncapped-gold nanoparticles located at the nodes of the MWCNT network.

### **Characterization**

The material was characterized after each step of modification to test whether the desired functionality was being introduced. A Perkin-Elmer UV–Vis spectrophotometer in the range of 200–800 nm was used to monitor the UV–vis absorption spectra of free gold nanoparticles and the Au-CysNPs dispersed in water. Fourier Transform Infrared (FT-IR) spectroscopy (supporting information) and X-ray photoelectron spectroscopy (XPS) were used to follow the functionalization of MWCNTs at each step and also after linking them with the Au-CysNPs. XPS analysis was performed using a Kratos AXIS Ultra DLD XPS equipped with a 180° hemispherical energy analyzer to determine the chemical composition of these nanotubes. Photoemission was stimulated by monochromated Al K-alpha radiation (1486.6 eV) with an operating power of 150 W. It was operated in the analyzer mode at 80 eV for survey scans and 20 eV for detailed scans of core level lines. Binding energies were referenced to the C 1s binding energy set at 284.5 eV. After the Au-CysNPs were linked to the MWCNTs, TEM was done to observe the location of the particles. A drop of the suspension of MWCNT linked with Au-CysNPs was placed on a 400 mesh copper TEM Quantifoil® holey carbon grid. This was

investigated using a JEOL 2010F TEM/STEM ( $C_s = 0.5$  mm) equipped with an ultra high resolution pole piece. An operating voltage of 200 kV was used. In STEM mode (0.5 nm probe, 15 cm camera length, 50  $\mu\text{m}$  condenser aperture), micro-EDS determined if sulfur surrounded the gold nanoparticle via gold-thiol bond while in the MWCNT network. A recently developed technique called D-STEM (Diffraction Scanning Transmission Electron Microscopy) was employed to confirm the identity of the particle at the node of two tubes.

#### **4.2. GRAPHENE BASED TCES**

Even after annealing the MWCNT-Au-Cys films, they still had a sheet resistance of 19.5  $\text{k}\Omega/\square$ . A single layer of graphene I grew using low pressure CVD on copper has a sheet resistance of  $\sim 1$   $\text{k}\Omega/\square$  after being transferred by Dr. Ji Won Suk<sup>102</sup>.

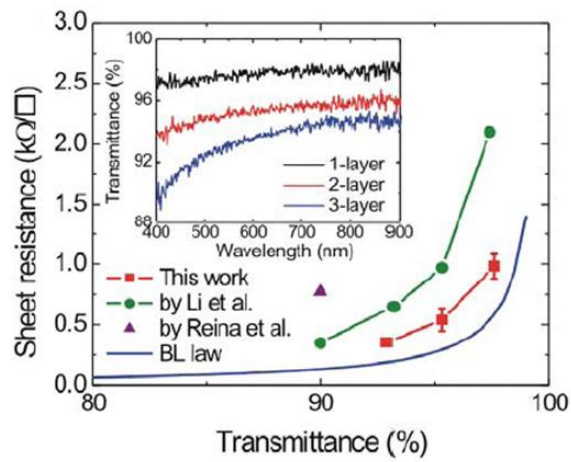


Figure 4.14. Sheet resistance vs. transmittance for graphene based transparent conducting electrodes<sup>102</sup>.

### Graphene/metal nanowires hybrid

Dr. Isakandar Kholmanov was able to reduce the sheet resistance of a single sheet of graphene I grew down to less than  $100 \Omega/\square$  by incorporating silver nanowires<sup>103</sup>.

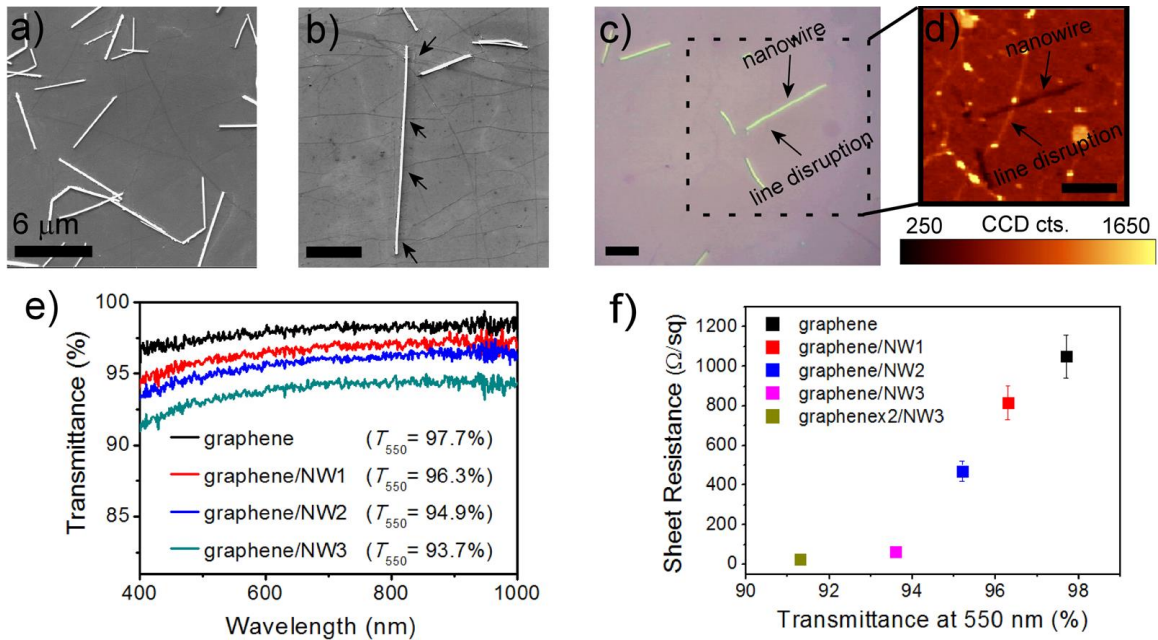


Figure 4.15. (a) Typical SEM image of graphene/NW films. (b) SEM image of a NW crossing several line disruptions shown by arrows. (c) Optical microscopy image of the hybrid films with a dashed line corresponding to the Raman map (1560–1620 cm<sup>-1</sup>) showing a NW crossing with a line disruption in d. Scale bars in a, b, c, and d are 6 μm. (e) Optical transmittance spectra of graphene and graphene/NW films. (f)  $R_s$  versus optical transmittance for graphene and graphene/NW films.<sup>103</sup>

### Graphene/CNT hybrid

Recently Dr. Isakandar Kholmanov has been able to incorporate two layers of doped graphene grown by me with aligned multi-walled carbon nanotubes in-between the layers to get sheet resistances below 10 Ω/□<sup>104</sup>.

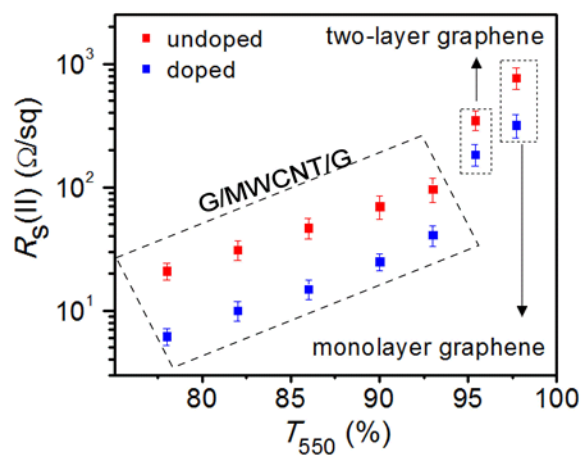


Figure 4.16. Transparent conducting films based on graphene and carbon nanotubes can achieve sheet resistances less than  $10 \Omega/\square$ <sup>104</sup>.

## Chapter Five: Large Graphene Domains

Growing large graphene domains on copper requires a low carbon flux to reduce the number of nucleation sites, which also results in a slow graphene growth rate. To achieve this, growth needs to be done under low carbon precursor pressure and high temperature. Under these high temperature, low pressure conditions, copper evaporates from the bare copper surface. Figure 5.1a shows an SEM image of a  $\sim 100$   $\mu\text{m}$  wide graphene island grown under low pressure for 4 hours. Figure 5.1b is a topology map (measured using an optical profilometer) of a graphene island from the same sample showing that the middle of the island is over  $1.5$   $\mu\text{m}$  higher than the surrounding bare copper surface. The dome-shape of the island is caused because while copper can continue evaporating from the bare copper surface, the graphene prevents further evaporation as it coats the surface. This can be prevented by enclosing the copper substrate to prevent the evaporated copper from leaving the growth system.

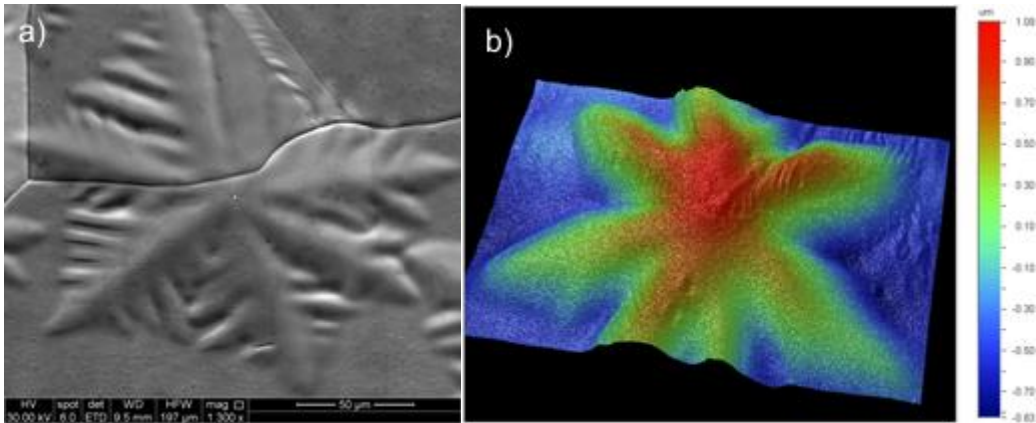


Figure 5.1. a) SEM image of graphene island grown under low pressure. b) Optical-profilometer data of a graphene island on the same copper foil as a).

The work described in this chapter was the result of a close collaboration with Dr. Xuesong Li who originally grew graphene inside a copper enclosure. My role was to build and maintain the CVD system to reproduce his results so that I could make all the samples, as well as characterize them, for use in generating this publication<sup>105</sup>. To provide a comprehensive picture, I also describe the work by my collaborators (the LEEM and PEEM analysis performed by Dr. R. M. Tromp and Dr. J. B. Hannon at IBM; the mobility measurements were performed by Dr. Venugopal), which resulted in a publication from this work<sup>105</sup>. Dr. Luigi Colombo was essential in guiding these experiments as well as the data analysis and write-up of the publication. Thus, I will allude to who did what in the chapter so that it is clear what I contributed.

## 5. ACHIEVING LARGE GRAPHENE DOMAINS INSIDE A COPPER ENCLOSURE<sup>§</sup>

### Introduction:

Graphene growth by chemical vapor deposition (CVD) has been receiving significant attention recently because of the ease with which large-area films can be grown, but the growth of large-domain or large-grain-size single crystals has not been reported to date.<sup>14</sup> In earlier work, growth of graphene on Cu by CVD was found to occur predominantly by surface nucleation followed by a two-dimensional growth process, but the domain size was limited to a few tens of micrometers.<sup>55, 106</sup> The presence of domain boundaries has been found to be detrimental to the transport properties; the precise mechanism of the degradation still remains elusive, but what is known is that structural defects promote surface reactions with adsorbates from the ambient or with deposited dielectrics.<sup>106</sup> The presence of heptagons and pentagons in the network of hexagons has been observed experimentally, and first-principles quantum-transport calculations have predicted that the periodicity-breaking disorder can adversely affect transport properties.<sup>107-108</sup> Any of these defects can give rise to higher surface chemical activity that would further disrupt the  $sp^2$ -bonding nature of graphene and thus impact graphene's fundamental properties. Therefore, it is imperative that large single crystals of graphene be grown to minimize the presence of defects arising from boundaries between

---

<sup>§</sup> Portions of this section have been published as Li, X.; **Magnuson, C. W.**; Venugopal, A.; Tromp, R. M.; Hannon, J. B.; Vogel, E. M.; Colombo, L.; Ruoff, R. S., Large-Area Graphene Single Crystals Grown by Low-Pressure Chemical Vapor Deposition of Methane on Copper. *Journal of the American Chemical Society* **2011**, 133 (9), 2816-2819.

misoriented domains. A very low pressure CVD process is reported here that yields graphene with domains of up to 0.5 mm in size, which is a factor of  $\sim 30$  times larger than previously reported.<sup>106</sup>

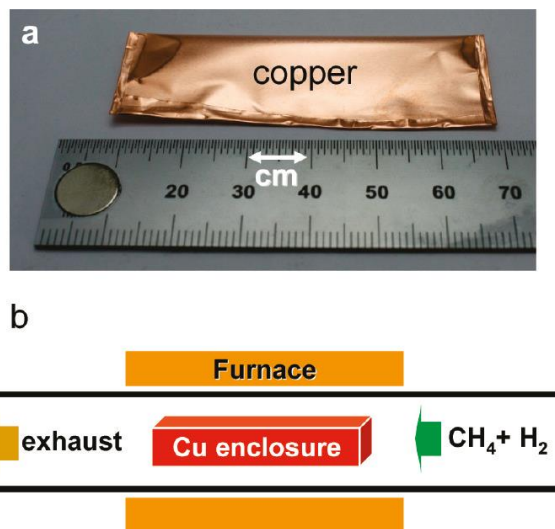


Figure 5.2. (a) Copper foil enclosure prior to insertion in the furnace. (b) Schematic of the CVD system for graphene on copper.<sup>105</sup>

The large-domain graphene growth was observed on the inside of a copper-foil enclosure at high temperature ( $\sim 1035$  °C). The copper-foil enclosure (Figure 5.2a) was formed by bending a 25  $\mu\text{m}$  thick copper foil and then crimping the three remaining sides. The basic growth conditions were similar to those previously reported<sup>55, 106</sup> but employed slightly lower methane flow rates and partial pressures (less than 1 sccm and 50 mTorr, respectively). Graphene grew on both the inside and outside of the Cu enclosure. The graphene growth on the outside showed behavior similar to the graphene growth reported by Li et al.,<sup>106</sup> but there was one difference: at the lower partial pressure

and flow rate and at much longer growth times, a higher density of bilayers and trilayers was observed. A publication on the reason for this by Dr. Yufeng Hao is in preparation. In contrast, the growth on the inside showed a much lower density of nuclei followed by very large domain growth after extended periods of time ( $>1$  h) and a much lower density of ad-layers. At this time, the precise growth conditions inside the enclosure are not well understood. However, the low density of nuclei is believed to be due to the much lower partial pressure of methane and an “improved” environment during growth; that is, the Cu vapor is in static equilibrium, and there is potentially a much lower pressure of unwanted species in the non-ultrahigh vacuum system. Figure 5.3 shows the average domain branch length (about half the domain size from the center of the domain) as a function of growth time for two methane flow rates, 0.5 and 1.3 sccm, which correspond to methane partial pressure of 8 and 21 mTorr, respectively. During the growth process, the hydrogen flow rate was kept constant at 2 sccm with a partial pressure of 27 mTorr, and the chamber background pressure was 17 mTorr. The graphene domains were very large, as shown by scanning electron microscope (SEM) images (Figure 5.4a). The domains also tended to have high “edge roughness”. The shape of the graphene nuclei in the initial stages of growth showed a hexagonal symmetry (Figure 5.4b). At first, the graphene domains grew as six-sided polygons, and these eventually grew into very large graphene domains with growing edges resembling dendrites (Figure 5.4c).

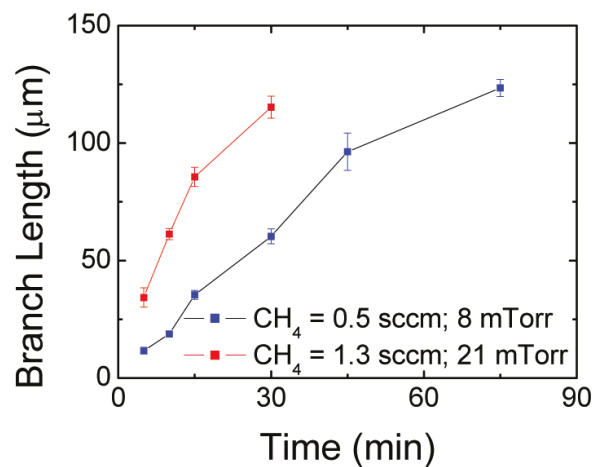


Figure 5.3. Graphene growth inside the enclosure as a function of time for two methane flow rates and partial pressures at 1035 °C.<sup>105</sup>

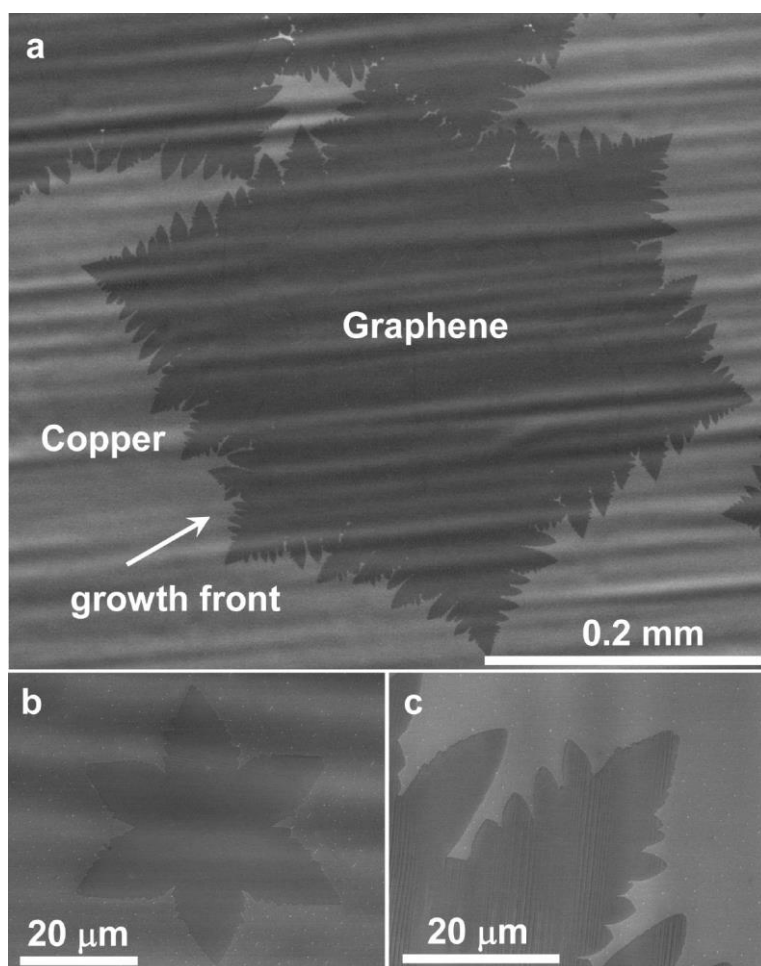


Figure 5.4. SEM images of graphene on copper grown by CVD. (a) Graphene domain grown at 1035 °C on Cu at an average growth rate of  $\sim 6 \mu\text{m}/\text{min}$ . (b) Graphene nuclei formed during the initial stage of growth. (c) High-surface-energy graphene growth front shown by the arrow in (a).<sup>105</sup>

A carbon isotope-labeling technique was also employed to delineate the graphene growth front in order to establish the boundaries between the growing “lobes”, the time dependence, and the spatial dependence.<sup>55</sup> In these experiments, the graphene films were grown by alternating the flow of  $^{12}\text{CH}_4$  and  $^{13}\text{CH}_4$  every 10 min for a total of 90 min at a

flow rate of 0.5 sccm and a corresponding partial pressure of 8 mTorr at 1035 °C. An analysis of the images in Figure 5.5 shows that the graphene growth rate was higher at the tips of the lobes ( $\sim 1.2 \mu\text{m}/\text{min}$ ; region 3b) and lower between the lobes and near the end of the growth process ( $0.1 \mu\text{m}/\text{min}$ ; region 7b), as also seen by the spatial coverage variation of graphene. Furthermore, graphene covered the copper surface and closed onto itself as the growth front advanced. The growth rate at points where the graphene joined was lower than at the tip of the growing front. Figure 5.5 also shows the shape of the growth front at different times during growth, as delineated by the boundaries between the domains of  $^{12}\text{C}$ - and  $^{13}\text{C}$ -based graphene. The structure of the domains, their distribution, and the graphene growth-front structure provide further indications that the growth was surface-mediated, as previously reported.<sup>55</sup> These data also show that the growth was a result of surface growth on the inside of the enclosure rather than diffusion through the Cu from outside the enclosure followed by precipitation upon cooling.

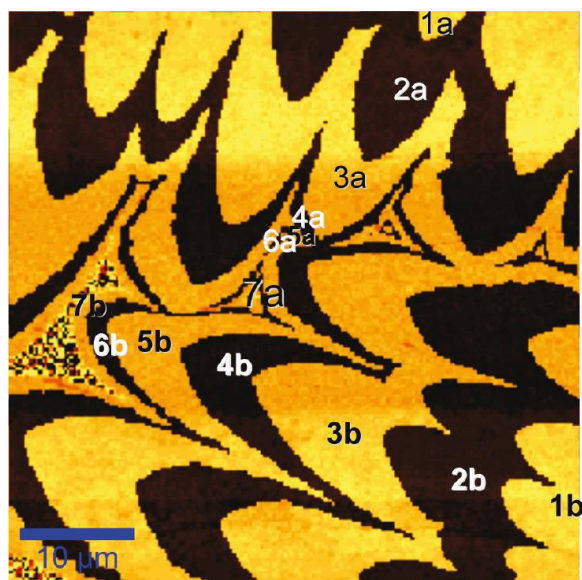


Figure 5.5. Raman map of the G bands corresponding to  $^{12}\text{C}$  (yellow) and  $^{13}\text{C}$  (black). The numbers in the figure correspond to the relative methane cycle numbers.<sup>105</sup>

In order to probe the domain size of the graphene, spatially resolved electron diffraction measurements were made using low energy electron microscopy (LEEM) by Dr. R. M. Tromp and Dr. J. B. Hannon at IBM.<sup>109</sup> Using photoelectron emission microscopy (PEEM), the edge of a graphene domain was located (Figure 5.6a). The diffraction pattern from 2  $\mu\text{m}$  areas of the surface were then recorded. Diffraction from the substrate revealed a highly faceted, rough Cu(100) surface with sharp diffraction spots, while diffraction from the graphene was diffuse (Figure 5.6b-e). The diffuse pattern was similar to that for diffraction from free-standing graphene,<sup>110</sup> perhaps indicating a weak coupling to the rough substrate. To estimate the domain size, the diffraction pattern was recorded as the sample was scanned under the beam along a line

at a constant speed of  $15 \mu\text{m/s}$ , and Figure 5.6 shows the PEEM images and diffraction patterns from selected points along the line scan. Each pattern is labeled by the position from which it was recorded.

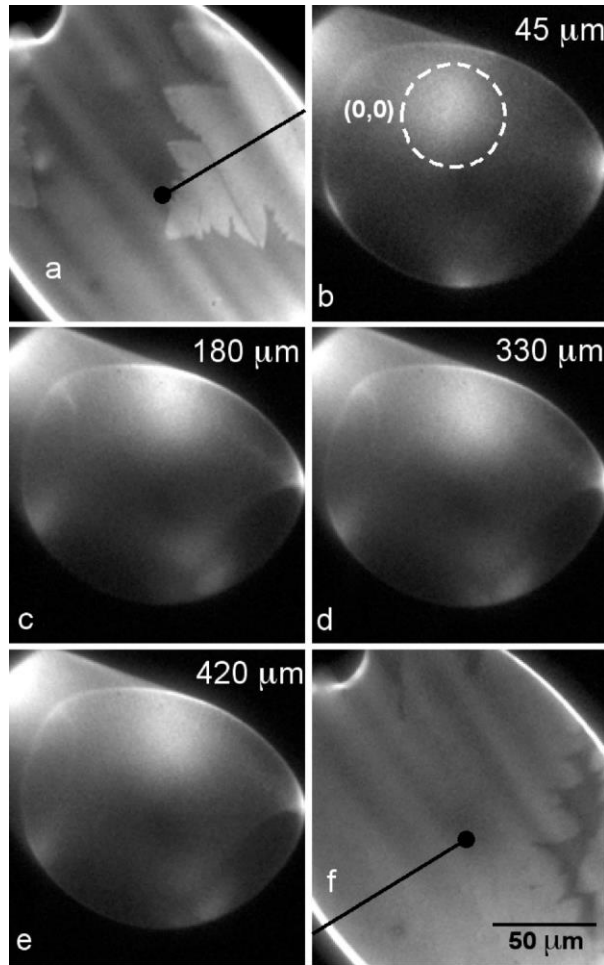


Figure 5.6. (a) PEEM image recorded near a graphene domain. The black line indicates the path from which selected-area diffraction patterns were recorded. The graphene is bright, and the surrounding Cu foil is dark. (b-e) Electron diffraction patterns (33 eV) recorded from  $2 \mu\text{m}$  areas of the graphene. Each pattern is labeled by the position along the black line in (a) at which the pattern was recorded. The diffraction spots are indicated in (b). (f) PEEM image recorded at the end of the scan.<sup>105</sup>

While there were slight continuous rotations of the pattern due to waviness in the foil, there were no discontinuous changes in the orientation of the diffraction spots, suggesting that along this scan of over 400  $\mu\text{m}$ , there were no rotational domain boundaries. Similar measurements were made on a number of domains. On occasion, large ( $>50 \mu\text{m}$ ) domains were observed with a 30 degree relative rotation of the graphene lattice, but in most of the scans, no rotational domain boundaries were observed.

After growth, I transferred the graphene films on to  $\text{SiO}_2/\text{Si}$  substrates as described by Li et al.<sup>111</sup> in order to analyze the films by Raman spectroscopy and perform electrical measurements. Figure 5.7 shows Raman maps of the D-band (Figure 5.7a) and G band (Figure 5.7b) and Raman spectra recorded at two different regions of the domain (Figure 5.7c), one within the film and the other close to the dendrite edge. The spectra show that the growing material was indeed graphene, with a low D-band intensity across the domain and the presence of graphene only. The full width at half-maximum (FWHM) of the G-band was about the same for the two regions ( $23 \text{ cm}^{-1}$ ), and the intensity ratio of the 2D band to the G-band suggests that the carrier concentration was different for the two regions.<sup>112</sup>

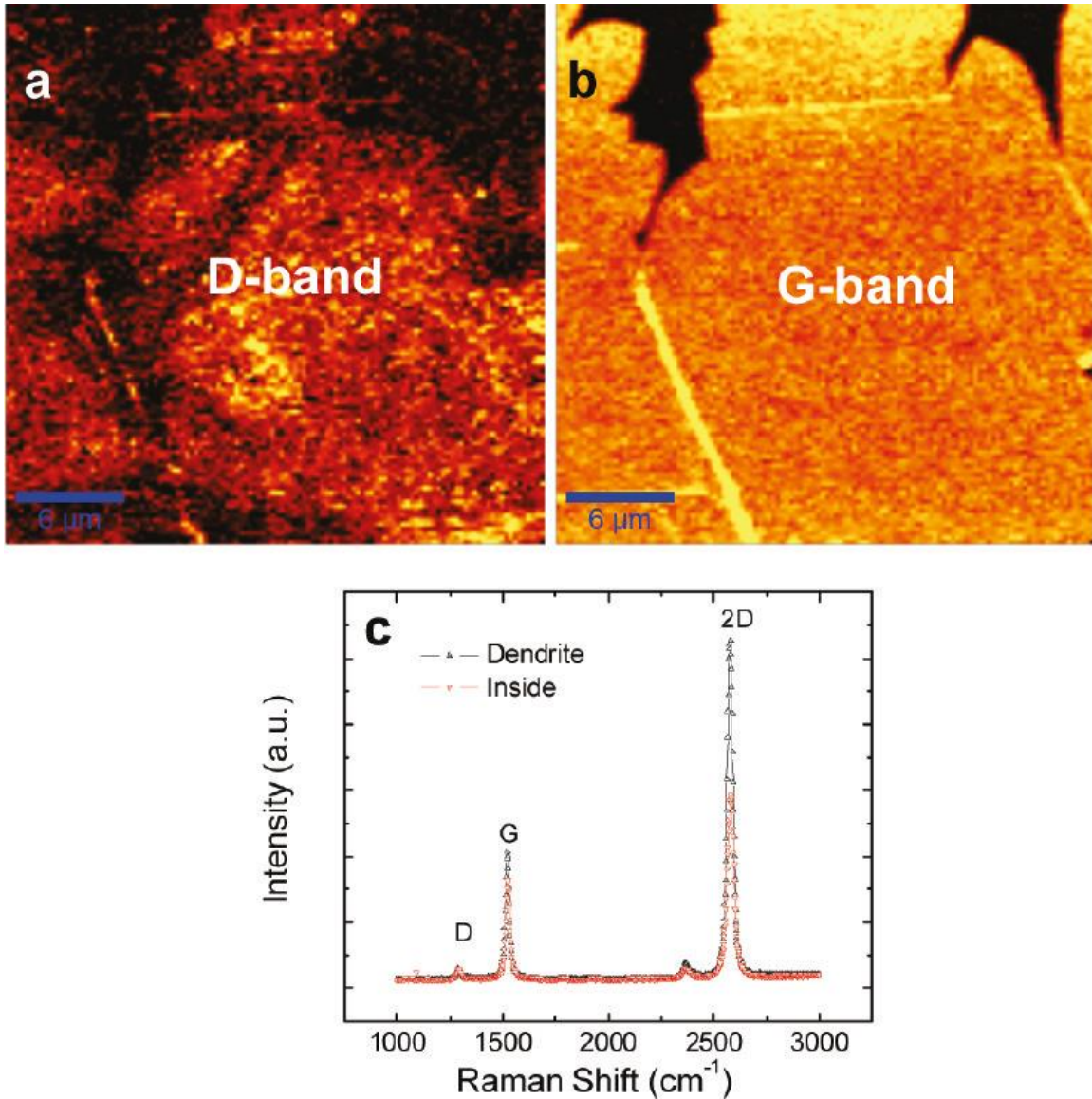


Figure 5.7. (a) D-band and (b) G-band Raman maps of graphene within the domain and at the edges of the growing domain and (c) Raman spectra of large-domain graphene within the bulk of the film and along the dendrite. The FWHM of the 2D-band of the dendrite was slightly smaller than that of the bulk, and the ratio of the intensities of the 2D- and G-bands was larger for the dendritic region than the bulk, suggesting a lower carrier concentration for the dendritic region within the “bulk” of the domain and the tip of the dendrite. The 2D-peak FWHM was  $38\text{ cm}^{-1}$  for the bulk and  $32\text{ cm}^{-1}$  for the dendrite, whereas the G-band FWHM was  $\sim 23\text{ cm}^{-1}$  for both regions.<sup>105</sup>

The quality of the large-area-domain films was also evaluated by measuring the transport properties of the graphene films transferred onto silicon dioxide grown on Si wafers. Field-effect transistors were fabricated by Dr. Archana Venugopal using nickel for the source and drain contacts and the highly doped Si substrate as the back-gate contact. The resistance was measured at room temperature as a function of back-gate voltage, and the mobility was extracted using the methodology introduced by Kim et al.<sup>113</sup> The mobility for these large-domain films was found to be greater than  $4000 \text{ cm}^2 \text{ V}^{-1} \text{ s}^{-1}$ , which is reasonably high but not as high as the highest value for exfoliated films, thus suggesting that the films and transfer process still need improvement.

This method was recently modified by a post-doc in my research group, Dr. Yufeng Hao, to include an oxidation step shortly before graphene growth at very low methane flow rates to grow graphene domains  $\sim 1 \text{ cm}$  across (shown in Figure 5.8) on the inside of the copper pocket<sup>114</sup>.

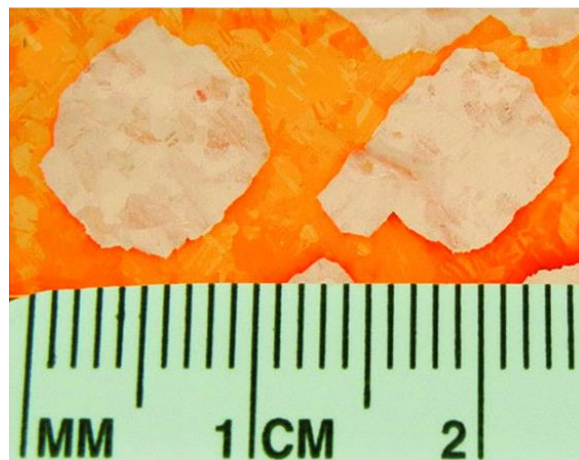


Figure 5.8. Optical image of centimeter-scale graphene domains grown on the inside of an oxidized copper pocket<sup>114</sup>.

## Chapter Six: Graphene ad-layers\*\*

### INTRODUCTION:

In 2009, Li *et al.* published their results on the synthesis of large scale graphene on copper foils via chemical vapor deposition using methane as the carbon precursor<sup>14</sup>. While mostly monolayer graphene was achieved over square centimeter areas, ad-layer regions were present. This is now the main method of producing very large area graphene films for research and commercial applications. However, there are still ad-layers present in this ‘monolayer graphene’ and they have been shown to grow underneath the first graphene layer<sup>115-117</sup>. The cause of, and control of, these ad-layers remains an active research area and their presence has been attributed to several factors including copper purity<sup>31</sup>, hydrogen terminated graphene edges<sup>118</sup>, and carbon diffusion through copper<sup>119</sup>.

We recently described a growth process using inductive heating for the growth of CVD graphene on copper, instead of a tube furnace<sup>120</sup>. The graphene obtained in this study have higher carrier mobilities compared to the graphene grown in hot-walled reactors (typically, tube furnaces)<sup>120</sup>. Graphene grown in the presence of hydrogen had many small ad-layer islands and an increased Raman D-peak (indicating more defective graphene)<sup>120</sup>. While hydrogen has been cited as a necessary component for CVD graphene growth<sup>121-124</sup> under low pressure conditions, it has also been shown to be

---

\*\* Portions of this chapter are to be submitted for publication as Carl W. Magnuson, Alvin Lee, Richard Piner, Luigi Columbo, and Rodney S. Ruoff; Increased Graphene Ad-layer Growth on Copper by Chemical Vapor Deposition Under Helium.

detrimental to growing high-quality graphene<sup>125-126</sup>. Ryu *et al.* recently demonstrated the ability to synthesize predominantly mono-layer graphene on copper via hydrogen-free rapid thermal chemical vapor deposition<sup>127</sup>. Recent DFT calculations have shown that hydrogen can passivate graphene edges making it easier for carbon species to diffuse past the graphene edge to underneath the original graphene layer and promote ad-layer growth<sup>118</sup>. It is hypothesized here that the hydrogen may also be playing another role in promoting graphene ad-layer growth because copper dissolves a significant amount of hydrogen at higher temperatures and pressures<sup>128-129</sup>. Proposed here is that this dissolved hydrogen can precipitate at the Cu-graphene interface and promote the diffusion of carbon species under the original graphene layer. Using a copper enclosure has been shown to reduce graphene nucleation and growth rates on the inside of the pocket and yields extremely large graphene domains<sup>105</sup>. Usually, when not using a copper enclosure, once the surface of the copper is covered by graphene, no additional hydrogen can diffuse into the copper – thus preventing any additional graphene ad-layer growth. However, since the graphene growth inside the pocket is dramatically slower than the outside, hydrogen can continue to be dissolved into the copper from inside the pocket and diffuse through to underneath the outer graphene layer. This added source of hydrogen continues to promote carbon diffusion under the original graphene layers and yields multilayered graphene on the outside surface of the enclosure. This – along with carbon diffusion from the inside of the pocket<sup>119</sup> - may further explain why the graphene grown on the outside of a copper enclosure contains such a high density of multi-layer graphene.

Here, to see if it is in fact this effect of gas diffusing through the copper substrate that is responsible for increased graphene ad-layer growth, helium is used as the background gas instead of hydrogen. Hydrogen has already been shown to promote increased graphene ad-layer growth by passivating the graphene edges and decoupling them from the copper surface<sup>118</sup>. However, helium is chemically inert and does not react with the graphene edges. We find that using helium does indeed induce ad-layer growth on flat copper strips. This further supports the theory that gas dissolved in the copper substrate facilitates additional graphene growth underneath the original growing graphene layer. In addition, the work here demonstrates that while hydrogen plays an important role in copper reduction, other than to maintain a reducing atmosphere it is not necessary for CVD graphene growth on copper.

## **METHODS:**

### **Graphene Synthesis.**

Graphene films were grown on a 125  $\mu\text{m}$  thick oxygen-free high conductivity (OFHC) copper foil (99.99% C10200, Eagle Brass) through inductive heating. This foil was cut into 25 mm by 12 mm strips that were thoroughly degreased by rinsing and soaking in acetone. The samples were stored in sealed vials of acetone in a dark drawer as exposure to UV light results in the formation of copper acetate<sup>64</sup>. When removed from the acetone, the foil was again rinsed with acetone and blown dry with  $\text{N}_2$ . To further clean the surface, the foil was placed in 10% nitric acid in water for 10 minutes,

thoroughly rinsed with 18 M $\Omega$  nano pure water, and blown dry with N<sub>2</sub>. The foil was then placed inside a 20 mm inner diameter fused silica tube that was then inserted into the 25 mm fused silica tube of the CVD system. (This makes it easy to load/unload the copper foils and clean any evaporated copper from the small diameter silica tube.) The pre-growth process to clean and anneal the substrate *in-situ* is as follows: (i) load the Cu foil into the chamber and, with the chamber still open to ambient conditions, heat the foil with 575 W power (~650 °C) for 1 minute. The sample oxidizes and turns black while also burning away any existing carbon and graphene from the sample.; (ii) evacuate the chamber to below 10<sup>-9</sup> Torr; (iii) heat with 200 W power (~650 °C) for 5 min; (iv) fill with 5% hydrogen in argon to 700 Torr for 5 minutes; (v) repeat (iii) and (iv) at 800 °C; (vi) evacuate the chamber to below 10<sup>-9</sup> Torr while allowing the substrate to cool and then re-fill with 5% hydrogen; (vii) heat the foil to 1050 °C for 30 minutes; (viii) repeat (vi) and (vii); (ix) evacuate the chamber to below 10<sup>-9</sup> Torr while allowing the substrate to cool. For graphene growth, the chamber is filled to 650 Torr with the desired background gas (Ar, He, or 5% H<sub>2</sub> in Ar). The sample is then manually heated to 900 °C and then linearly heated to the desired growth temperature over 1 minute. After 5 minutes, an additional 50 Torr of 5% methane in argon is added to the chamber over 30 seconds - for a total chamber pressure of 700 Torr – and held at the growth temperature for 10 minutes. The sample is cooled (first under decreasing power to 700 °C over 5 seconds and then to room temperature under no power by radiative cooling) while the

chamber is evacuated to below  $10^{-9}$  Torr. The sample is allowed to cool for 30 min under vacuum before being removed using argon to bring the chamber back to 1 atm pressure.

Graphene grown with a copper enclosure was performed exactly as described in a previous publication<sup>105</sup>.

### **Characterization.**

Scanning electron microscopy images were obtained using an FEI Quanta-600 FEG-ESEM at an accelerating voltage of 30 kV. Raman spectra were obtained using a WITec Alpha 300 confocal Raman spectroscope with a laser wavelength of 488 nm and a 100x objective lens (laser spot size is ~300 nm).

### **RESULTS AND DISCUSSION:**

In 2011, we published on a method to grow extremely large area single crystal graphene domains on the inside of a copper enclosure (i.e. a copper pocket)<sup>105</sup>. Recently, we have been able to grow domains over 1 cm across on the inside of copper pocket<sup>114</sup>. This “pocket method” was used to grow the graphene shown in the scanning electron microscopy (SEM) images in Figure 6.1. While the inside of the enclosure contains very large mostly monolayer graphene domains ~0.5 mm across, the outside is covered almost entirely by multi-layered graphene, with less than 5% being monolayer graphene. Graphene grown on copper strips at the same time with a copper enclosure produces

results similar to other growths on copper strips (i.e. <5% ad-layer coverage). Why the outside of the enclosure grows predominantly multi-layer graphene has heretofore been unpublished. It has been reported that, without the presence of hydrogen, copper does not form a carbide and does not diffuse into - or through - copper<sup>130-131</sup>. Because of this, carbon catalyzed from the methane on the bare copper surface inside the pocket was thought to be unable to diffuse through to the underside of the outer graphene layers. Recently observed evidence, however, indicates that carbon is in fact able to diffuse from the bare inner copper surface to the underside of the outside graphene layers<sup>119</sup>. The bare copper inner surface of the pocket also allows the continued absorption of hydrogen, which also diffuses to the outside of the copper pocket. This added surface hydrogen may also be promoting ad-layer growth by allowing carbon species on the outside of the pocket to diffuse under the existing graphene islands before the islands have merged together to form a continuous graphene sheet.

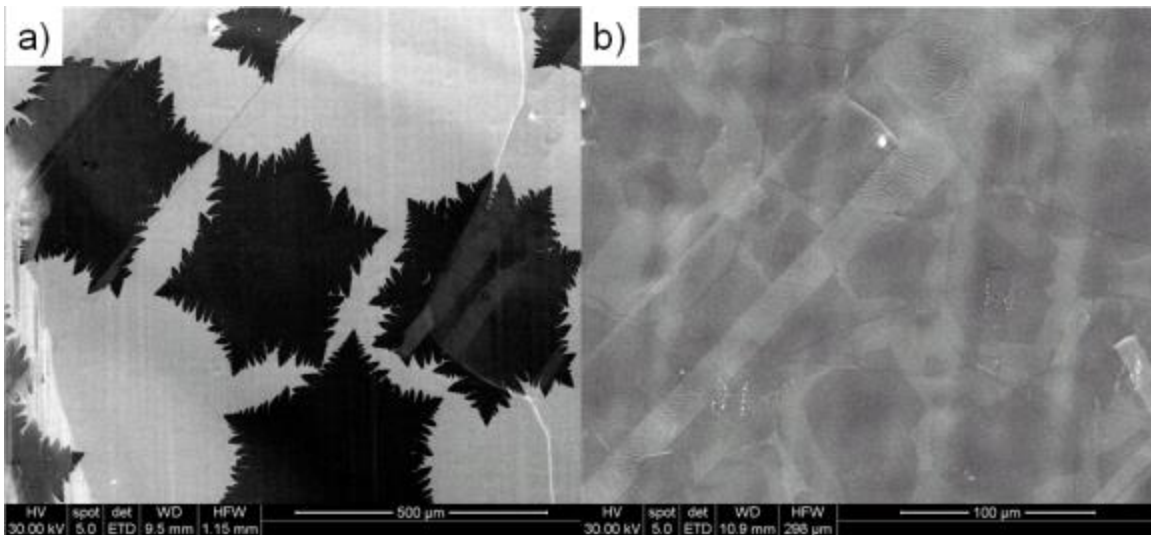


Figure 6.1. SEM images of graphene grown from a) the inside of the copper enclosure and b) the outside of the same enclosure. The darker contrast areas indicate more graphene layers.

As revealed in our recent publication on using magnetic inductive heating to grow graphene on copper substrates, we found that adding an argon anneal (after reducing the copper with hydrogen) and growing graphene without the presence of hydrogen gas significantly decreases the density of graphene ad-layers<sup>120</sup>. Figure 6.2 shows SEM images from this study depicting how ad-layer growth is suppressed when growing graphene without the presence of hydrogen gas. This work demonstrates that hydrogen gas is both not needed to grow graphene on copper and promotes graphene ad-layer growth. It also hypothesized that hydrogen dissolved in and diffusing through the copper was a cause of increased ad-layer growth. This is in addition to the recently modeled role of hydrogen passivating the graphene edges<sup>118</sup>.

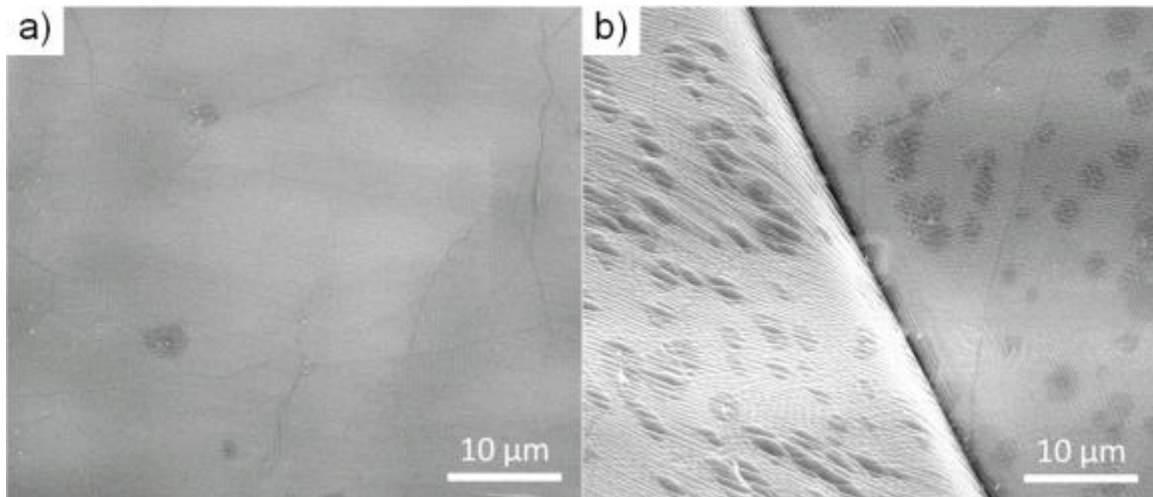


Figure 6.2. SEM images of a) mostly monolayer graphene grown with methane in purely argon atmosphere and b) graphene with many ad-layers grown with methane in a 5% hydrogen in argon atmosphere. Darker areas indicate graphene ad-layers.<sup>120</sup>

To test if gas diffusing through the copper also promotes graphene ad-layer growth, graphene was grown under helium. If it is gas diffusion that causes increased ad-layer growth, then growth under helium should result in a similar amount of graphene ad-layers as growing under hydrogen (which is what we see here). The activation energy for diffusion of helium in copper is  $\sim 1.1 \text{ eV}^{132}$ , hydrogen in copper is  $\sim 0.45 \text{ eV}^{133}$ , and argon in copper is  $\sim 2.65 \text{ eV}^{134}$  (for reference, the energy for vacancy formation in copper is  $1.28 \text{ eV}^{135}$ ). While at room temperature helium does not diffuse easily through copper (nine orders of magnitude slower than hydrogen), it does at elevated temperatures (at  $1000 \text{ }^\circ\text{C}$  only two orders of magnitude slower). Inert gas diffusion in metals is through the migration of vacancy-gas complexes with the rate-limiting step in the process being the jump of the gas out of the vacancy while a host atom jumps into that vacancy<sup>136</sup>. Helium was chosen because of both its ability to easily diffuse through copper (its activation

energy for diffusion is slightly less than the activation energy for vacancy formation in copper) and its chemical inertness. Since helium is chemically inert, if hydrogen was solely playing a chemical role of graphene edge passivation, resulting in increased ad-layer growth, then there would be a higher density of ad-layers after growth under hydrogen but not under helium (which is **not** what we see here).

To remove any already grown graphene - or any other carbon on the copper surface - an oxidation cleaning process was used similar to that recently published<sup>137</sup>. Here, the sample was heated to ~650 °C in the CVD chamber for 1 minute under ambient atmosphere. During this, the sample oxidizes and turns black. As the sample oxidizes and is then subsequently annealed at high temperature, the surface carbon is ‘burned off’ and removed from the surface through the formation of volatile carbon dioxide and carbon monoxide and provides a carbon free surface for graphene growth. Figure 6.3 shows SEM images of the same location on a copper substrate surface partially covered with graphene islands before the oxidation cleaning process (Figure 6.3a) and the clean surface after (Figure 6.3c). Interestingly, although the surface morphology changes drastically during this oxidation/reduction process (Figure 6.3b shows the surface after annealing under 5% hydrogen in argon to only 700 °C for 30 seconds), after the high temperature anneal the surface topology returns to that very similar to the original surface.

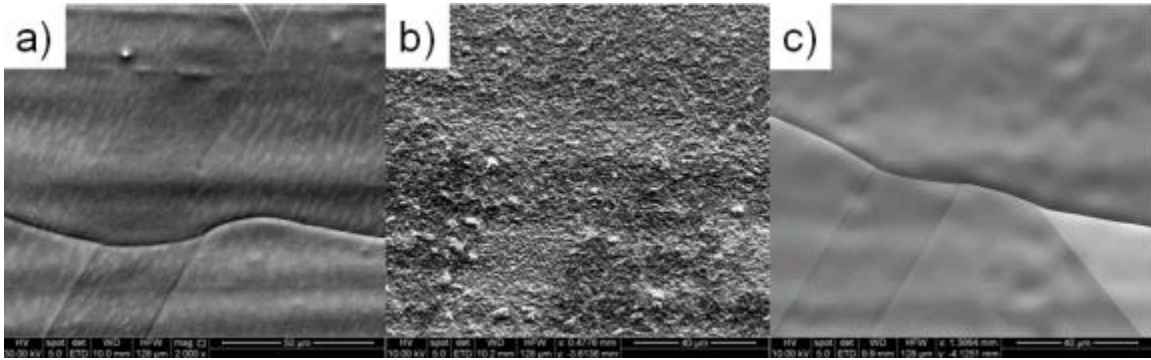


Figure 6.3. SEM images from the same location on the same copper substrate after a) submonolayer graphene growth, b) oxidation and annealing under 5% hydrogen in argon at 700 °C for 10 seconds, and c) annealing at 1000 °C for one hour.

Graphene was grown, in different runs on flat copper foils, under argon, helium, and 5% hydrogen in argon using 5% methane in argon at three different temperatures: 1000 °C, 1025 °C, and 1050 °C. Since the thermal conductivity of helium (428 mW/m/K for 1 atm at 1000 °C<sup>138</sup>) is significantly higher than that of argon (50.1 mW/m/K for 1 atm at 1000 °C<sup>139</sup>), more power is required to keep the substrate at 1000 °C under helium (~1800 W) than under argon (~650 W). The sample was held at the growth temperature for 5 minutes under 650 Torr of the background gas before 50 Torr of 5% methane in argon (which results in 2.5 Torr partial pressure of methane) was added over 30 seconds. As this is a ‘no-flow’ or ‘static-charge’ growth system, there is no gas flow rate during growth. As seen from the SEM images shown in Figure 6.4, the density of ad-layers on samples grown with either hydrogen or helium is similar while there are almost none present on the samples grown under argon. Interestingly, as seen in Figure 6.4d, the ad-layers can nucleate at different locations than the first graphene layer which indicates that the nucleation conditions for ad-layers may be different from the original layer.

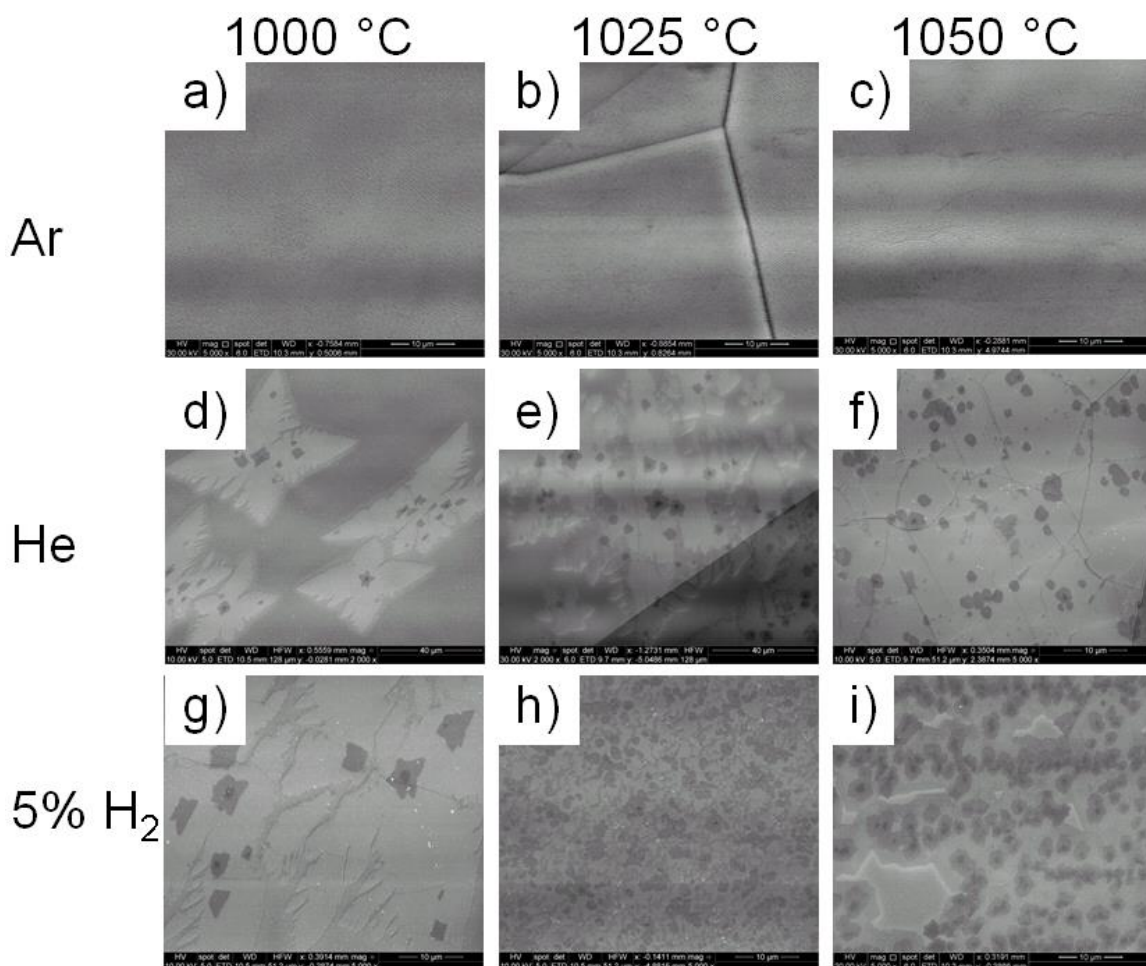


Figure 6.4. SEM images of graphene grown under (a-c) argon, (d-e) helium, and (g-i) 5% H<sub>2</sub> in argon. The samples were grown at (a,d,g) 1000 °C, (b,e,h) 1025 °C, and (c,f,i) 1050 °C.

While still on the copper substrate, Raman maps of the graphene shown in Figure 6.4e were made to verify that the difference in contrast seen in the SEM images correlate with graphene ad-layers (darker areas of the SEM images correspond to graphene ad-layers). Figure 6.5c shows the map of the Raman 2D-peak width - which changes with the number of graphene layers<sup>54, 140-142</sup>. As mentioned in the previous publication,

graphene grown under the presence of hydrogen had an increased Raman D-peak compared with the graphene grown under argon indicating that it was more defective<sup>120</sup>. Here we see a similar increased Raman D-peak in graphene grown under helium (Figure 6.5c). Not only do hydrogen and helium increase the number of graphene ad-layers, but it also results in more defective graphene.

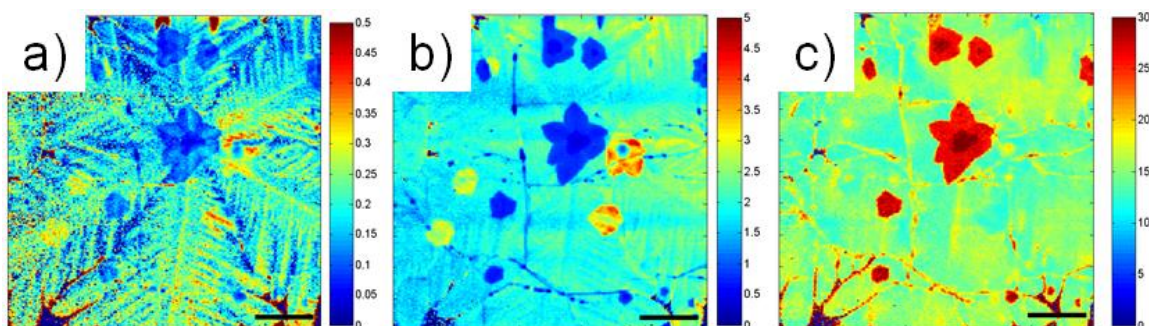


Figure 6.5. a and b) Micro-Raman maps of the graphene D and 2D peaks normalized to the G peak intensity for the sample grown under helium shown in Figure 6.4e. c) Raman map of the graphene 2D peak highlighting the ad-layer areas with a peak width of  $\sim 30 \text{ cm}^{-1}$ . Scale bars are  $5 \mu\text{m}$ .

### Conclusions:

Helium, like hydrogen, promotes the growth of graphene ad-layers during chemical vapor deposition on copper. This indicates that in addition to passivating graphene edges, hydrogen dissolved in the copper substrate may play an additional role in ad-layer growth. There are several possible explanations as to why there is increased ad-layer growth under hydrogen or helium than under argon: 1) Hydrogen and helium dissolve into and diffuse through copper more easily than argon. The dissolved gas is diffusing

through the copper to underneath the original graphene layer. As the gas comes to the copper surface, it is trapped by the graphene layer and delaminates the graphene slightly from the copper surface. This delamination allows carbon species to diffuse under the graphene and promotes ad-layer growth. 2) The hydrogen and helium are weakening the Cu-Cu surface bonds, which allows carbon species to diffuse under the graphene and promote ad-layer growth. 3) There is co-diffusion of H and C, or He and C, such that the H (or He) plays a role in allowing and accelerating the diffusion of C through the Cu to the underside of the original graphene layer. 4) At the high pressures, close to 1 atm, used in this study, trace impurities for the background gas may play a role in the observed results. Oxygen on the copper surface has been shown to remove the hydrogen from the graphene edges and promote carbon attachment<sup>114</sup>. If the helium used in this study has less trace oxygen than the argon, then the graphene edges may remain hydrogen terminated under the supplied helium but not under the supplied argon. The hydrogen terminated graphene edge may then be what is promoting the additional graphene layer growth<sup>118</sup>.

In order to reliably synthesize monolayer graphene with no ad-layers, growth should be done without the presence of hydrogen, helium, or any other gas which easily diffuses through the copper substrate. Using a larger atom inert background gas than argon, xenon for example, may further reduce graphene ad-layer growth and allow the synthesis of entirely mono-layer graphene films.

## Chapter Seven: Conclusions

In order to understand and further develop methods of producing graphene on copper foil by chemical vapor deposition, a new high-vacuum thermal CVD system was designed and built. The ability to operate this CVD system at pressure low enough to enable the use of a residual gas analyzer allowed the study of how oxygen evolves from decomposing copper oxide at high temperature in an oxygen deficient environment. Surface copper oxide was then deliberately used to release oxygen to ‘burn away’ any adventitious carbon on the copper surface, to produce clean copper substrate for repeatable low density graphene nucleation and growth of relatively large grain size graphene.

A potential application of large scale graphene films is as transparent conductive electrodes. Transparent conductive films of multi-walled carbon networks were modified by selectively depositing gold nanoparticles at the network nodes. Although the modified networks had half the sheet resistance as films made from unmodified multi-walled carbon nanotube networks, the sheet resistance was still more than that of even a single layer of graphene. The sheet resistance of graphene-based transparent conductive films can be improved by using multiple layers of graphene and by combining them with 1-dimensional conductive materials like metal nanowires or carbon nanotubes. Graphene including in these combinations is looking like it might be viable for TCF applications, particularly for flexible substrates.

Large graphene single crystals over 0.5 mm across have been grown inside copper enclosures with low methane partial pressures. While the inside of these enclosures produce large crystals of single layered graphene, the outside produces graphene with a high density of ad-layers. A possible cause for this increased ad-layer growth is proposed to be from gas (hydrogen in this case) diffusing through the copper and allowing carbon to diffuse under the original graphene. This source of carbon under the graphene layer allows for the growth of additional graphene layers. Growth of graphene on copper in a helium environment also leads to an increased density of graphene ad-layers while growing graphene in an argon (which does not diffuse through the copper as easily as hydrogen or helium) environment drastically decreases the amount of ad-layers.

As a result of this study, films of high quality graphene can be grown on copper substrates via high temperature chemical vapor deposition.

## Chapter Eight: Future Research Directions

While the quality of graphene produced on copper via CVD is already mature enough to be potentially viable in transparent conductive films, there are a couple of challenges that need to be overcome before it can be used for integrated circuits. First, the graphene film has wrinkles in it while still on the copper surface. A reason for this may be that while the copper substrate shrinks upon cooling after the high temperature graphene growth, the graphene itself expands due to its negative coefficient of thermal expansion (CTE)<sup>143</sup>. To mitigate this problem, either a low temperature growth method needs to be developed (which may not be thermodynamically possible) which would reduce the number of wrinkles by decreasing the amount the copper shrinks and graphene expands, or a method needs to be developed to remove the wrinkles while transferring the graphene onto a semiconducting substrate. Which brings up the second issue needing a better solution: the graphene must be reliably transferred onto semiconducting substrates on a large scale. Current transfer techniques have poor reliability, damage the graphene sheet, and/or introduce contaminants/dopants to the transferred film. To be commercially used in integrated circuits, smooth clean graphene needs to be reliably transferred onto semiconducting substrates.

As one final example, if graphene is to be used for spintronics, the orientation of the graphene crystal needs to be controlled. This may be possible under certain growth conditions on specific copper substrate crystal orientations. And while graphene domain boundaries do not have too adverse an impact on traditional electronic circuit

components, they could be detrimental to achieving large scale spintronic devices<sup>144</sup>. Not only does the graphene crystal orientation need to be controlled, but graphene crystals need to be large enough to enable full spintronic circuit fabrication<sup>8</sup>.

## Appendix

### ACRONYMS

<b>AFM</b>	Atomic Force Microscopy
<b>APCVD</b>	Atmospheric Pressure Chemical Vapor Deposition
<b>CNT</b>	Carbon Nanotube
<b>CTE</b>	Coefficient of Thermal Expansion
<b>CVD</b>	Chemical Vapor Deposition
<b>DFT</b>	Density Functional Theory
<b>D-STEM</b>	Diffraction Scanning Transmission Electron Microscopy
<b>EBID</b>	Electron Beam Induced Deposition
<b>FET</b>	Field Effect Transistor
<b>FTIR</b>	Fourier Transform Infrared Spectroscopy
<b>FWHM</b>	Full Width at Half Maximum
<b>HOPG</b>	Highly Ordered Pyrolytic Graphite
<b>ITO</b>	Indium Tin Oxide
<b>LEEM</b>	Low Energy Electron Microscopy
<b>MFC</b>	Mass Flow Controller
<b>MWCNT</b>	Multi-walled Carbon Nanotube
<b>OFHC</b>	Oxygen Free High Conductivity
<b>PED</b>	Proportional Integral Derivative
<b>PEEM</b>	PhotoElectron Emission Microscopy
<b>ppm</b>	Parts Per Million
<b>PMMA</b>	Poly(methyl methacrylate)
<b>RF</b>	Radio Frequency
<b>RGA</b>	Residual Gas Analyzer
<b>sccm</b>	Standard Cubic Centimeter
<b>SEM</b>	Scanning Electron Microscopy
<b>STP</b>	Standard Temperature and Pressure
<b>TCE</b>	Transparent Conductive Electrode
<b>TCF</b>	Transparent Conductive Film
<b>TEM</b>	Transmission Electron Microscope
<b>UHV</b>	Ultra High Vacuum
<b>UT</b>	The University of Texas at Austin
<b>UV</b>	Ultra-Violet
<b>XPS</b>	X-ray photoelectron spectroscopy

## LIST OF PUBLICATIONS

1. Li, X.; Magnuson, C. W.; Venugopal, A.; An, J.; Suk, J. W.; Han, B.; Borysiak, M.; Cai, W.; Velamakanni, A.; Zhu, Y.; Fu, L.; Vogel, E. M.; Voelkl, E.; Colombo, L.; Ruoff, R. S., Graphene Films with Large Domain Size by a Two-Step Chemical Vapor Deposition Process. *Nano Letters* **2010**, *10* (11), 4328-4334.
2. Li, X.; Magnuson, C. W.; Venugopal, A.; Tromp, R. M.; Hannon, J. B.; Vogel, E. M.; Colombo, L.; Ruoff, R. S., Large-Area Graphene Single Crystals Grown by Low-Pressure Chemical Vapor Deposition of Methane on Copper. *Journal of the American Chemical Society* **2011**, *133* (9), 2816-2819.
3. Chen, S.; Brown, L.; Levendorf, M.; Cai, W.; Ju, S.-Y.; Edgeworth, J.; Li, X.; Magnuson, C. W.; Velamakanni, A.; Piner, R. D.; Kang, J.; Park, J.; Ruoff, R. S., Oxidation Resistance of Graphene-Coated Cu and Cu/Ni Alloy. *ACS Nano* **2011**, *5* (2), 1321-1327.
4. Suk, J. W.; Kitt, A.; Magnuson, C. W.; Hao, Y.; Ahmed, S.; An, J.; Swan, A. K.; Goldberg, B. B.; Ruoff, R. S., Transfer of CVD-Grown Monolayer Graphene onto Arbitrary Substrates. *ACS Nano* **2011**, *5* (9), 6916-6924.
5. Chen, S.; Moore, A. L.; Cai, W.; Suk, J. W.; An, J.; Mishra, C.; Amos, C.; Magnuson, C. W.; Kang, J.; Shi, L.; Ruoff, R. S., Raman Measurements of Thermal Transport in Suspended Monolayer Graphene of Variable Sizes in Vacuum and Gaseous Environments. *ACS Nano* **2010**, *5* (1), 321-328.
6. Pirkle, A.; Chan, J.; Venugopal, A.; Hinojos, D.; Magnuson, C. W.; McDonnell, S.; Colombo, L.; Vogel, E. M.; Ruoff, R. S.; Wallace, R. M., The effect of chemical residues on the physical and electrical properties of chemical vapor deposited graphene transferred to SiO<sub>2</sub>. *Applied Physics Letters* **2011**, *99* (12), 122108.
7. An, J.; Voelkl, E.; Suk, J. W.; Li, X.; Magnuson, C. W.; Fu, L.; Tiemeijer, P.; Bischoff, M.; Freitag, B.; Popova, E.; Ruoff, R. S., Domain (Grain) Boundaries and Evidence of “Twinlike” Structures in Chemically Vapor Deposited Grown Graphene. *ACS Nano* **2011**, *5* (4), 2433-2439.
8. Stoller, M. D.; Magnuson, C. W.; Zhu, Y.; Murali, S.; Suk, J. W.; Piner, R.; Ruoff, R. S., Interfacial capacitance of single layer graphene. *Energy & Environmental Science* **2011**, *4* (11), 4685-4689.
9. Kholmanov, I. N.; Magnuson, C. W.; Aliev, A. E.; Li, H.; Zhang, B.; Suk, J. W.; Zhang, L. L.; Peng, E.; Mousavi, S. H.; Khanikaev, A. B.; Piner, R.; Shvets, G.; Ruoff, R. S., Improved Electrical Conductivity of Graphene Films Integrated with Metal Nanowires. *Nano Letters* **2012**, *12* (11), 5679-5683.
10. Velamakanni, A.; Magnuson, C. W.; Ganesh, K. J.; Zhu, Y.; An, J.; Ferreira, P. J.; Ruoff, R. S., Site-Specific Deposition of Au Nanoparticles in CNT Films by Chemical Bonding. *ACS Nano* **2010**, *4* (1), 540-546.
11. Ramón, M. E.; Parrish, K. N.; Chowdhury, S. F.; Magnuson, C. W.; Movva, H. C. P.; Ruoff, R. S.; Banerjee, S. K.; Akinwande, D., Three-Gigahertz Graphene Frequency

Doubler on Quartz Operating Beyond the Transit Frequency *IEEE Transactions on Nanotechnology* **2012**, 11 (5), 877 - 883.

## References

1. Venugopal, A.; Chan, J.; Li, X.; Magnuson, C. W.; Kirk, W. P.; Colombo, L.; Ruoff, R. S.; Vogel, E. M., Effective mobility of single-layer graphene transistors as a function of channel dimensions. *Journal of Applied Physics* **2011**, *109* (10), 104511-5.
2. Novoselov, K. S.; Geim, A. K.; Morozov, S. V.; Jiang, D.; Zhang, Y.; Dubonos, S. V.; Grigorieva, I. V.; Firsov, A. A., Electric Field Effect in Atomically Thin Carbon Films. *Science* **2004**, *306* (5696), 666-669.
3. Das Sarma, S.; Adam, S.; Hwang, E. H.; Rossi, E., Electronic transport in two-dimensional graphene. *Reviews of Modern Physics* **83** (2), 407-470.
4. Bolotin, K. I.; Sikes, K. J.; Jiang, Z.; Klima, M.; Fudenberg, G.; Hone, J.; Kim, P.; Stormer, H. L., Ultrahigh electron mobility in suspended graphene. *Solid State Communications* **2008**, *146* (9-10), 351-355.
5. Seol, J. H.; Jo, I.; Moore, A. L.; Lindsay, L.; Aitken, Z. H.; Pettes, M. T.; Li, X.; Yao, Z.; Huang, R.; Broido, D.; Mingo, N.; Ruoff, R. S.; Shi, L., Two-Dimensional Phonon Transport in Supported Graphene. *Science* **2010**, *328* (5975), 213-216.
6. Balandin, A. A.; Ghosh, S.; Bao, W.; Calizo, I.; Teweldebrhan, D.; Miao, F.; Lau, C. N., Superior Thermal Conductivity of Single-Layer Graphene. *Nano Letters* **2008**, *8* (3), 902-907.
7. Lee, C.; Wei, X.; Kysar, J. W.; Hone, J., Measurement of the Elastic Properties and Intrinsic Strength of Monolayer Graphene. *Science* **2008**, *321* (5887), 385-388.
8. Maurer, P. C.; Kucsko, G.; Latta, C.; Jiang, L.; Yao, N. Y.; Bennett, S. D.; Pastawski, F.; Hunger, D.; Chisholm, N.; Markham, M.; Twitchen, D. J.; Cirac, J. I.; Lukin, M. D., Room-Temperature Quantum Bit Memory Exceeding One Second. *Science* **2012**, *336* (6086), 1283-1286.
9. Tannock, Q., Exploiting carbon flatland. *Nat Mater* **2012**, *11* (1), 2-5.
10. Jo, S. B.; Park, J.; Lee, W. H.; Cho, K.; Hong, B. H., Large-area graphene synthesis and its application to interface-engineered field effect transistors. *Solid State Communications* **2012**, *152* (15), 1350-1358.
11. Batzill, M., The surface science of graphene: Metal interfaces, CVD synthesis, nanoribbons, chemical modifications, and defects. *Surface Science Reports* **2012**, *67* (3-4), 83-115.
12. Dreyer, D. R.; Ruoff, R. S.; Bielawski, C. W., From Conception to Realization: An Historical Account of Graphene and Some Perspectives for Its Future. *Angewandte Chemie International Edition* **49** (49), 9336-9344.
13. Boehm, H. P.; Setton, R.; Stumpp, E., Nomenclature and terminology of graphite intercalation compounds. *Carbon* **1986**, *24* (2), 241-245.
14. Li, X.; Cai, W.; An, J.; Kim, S.; Nah, J.; Yang, D.; Piner, R.; Velamakanni, A.; Jung, I.; Tutuc, E.; Banerjee, S. K.; Colombo, L.; Ruoff, R. S., Large-Area Synthesis of High-Quality and Uniform Graphene Films on Copper Foils. *Science* **2009**, *324* (5932), 1312-1314.

15. Petrone, N.; Dean, C. R.; Meric, I.; van der Zande, A. M.; Huang, P. Y.; Wang, L.; Muller, D.; Shepard, K. L.; Hone, J., Chemical Vapor Deposition-Derived Graphene with Electrical Performance of Exfoliated Graphene. *Nano Letters* **2012**, *12* (6), 2751-2756.
16. Geim, A. K.; Novoselov, K. S., The rise of graphene. *Nat Mater* **2007**, *6* (3), 183-191.
17. Berger, C.; Song, Z.; Li, T.; Li, X.; Ogbazghi, A. Y.; Feng, R.; Dai, Z.; Marchenkov, A. N.; Conrad, E. H.; First, P. N.; de Heer, W. A., Ultrathin Epitaxial Graphite: 2D Electron Gas Properties and a Route toward Graphene-based Nanoelectronics. *The Journal of Physical Chemistry B* **2004**, *108* (52), 19912-19916.
18. Chen, J.-H.; Jang, C.; Xiao, S.; Ishigami, M.; Fuhrer, M. S., Intrinsic and extrinsic performance limits of graphene devices on SiO<sub>2</sub>. *Nat Nano* **2008**, *3* (4), 206-209.
19. Sundaram, R. S.; Steiner, M.; Chiu, H.-Y.; Engel, M.; Bol, A. A.; Krupke, R.; Burghard, M.; Kern, K.; Avouris, P., The Graphene-Gold Interface and Its Implications for Nanoelectronics. *Nano Letters* **2011**, *11* (9), 3833–3837.
20. Siegel, D. A.; Park, C.-H.; Hwang, C.; Deslippe, J.; Fedorov, A. V.; Louie, S. G.; Lanzara, A., Many-body interactions in quasi-freestanding graphene. 2011; Vol. 108, pp 11365-11369.
21. Moriconi, L.; Niemeyer, D., Graphene conductivity near the charge neutral point. *Physical Review B* **2011**, *84* (19), 193401.
22. Ricco, M.; Pontiroli, D.; Mazzani, M.; Choucair, M.; Stride, J. A.; Yazyev, O. V., Muons Probe Strong Hydrogen Interactions with Defective Graphene. *Nano Letters* **2011**, *11* (11), 4919–4922.
23. Zhou, Y.; Yang, J.; Cheng, X.; Zhao, N.; Sun, L.; Sun, H.; Li, D., Electrostatic self-assembly of graphene-silver multilayer films and their transmittance and electronic conductivity. *Carbon* **2012**, *50* (12), 4343-4350.
24. Boehm, H. P.; Clauss, A.; Fischer, G. O.; Hofmann, U., Thin Carbon Leaves. *Z. Naturforsch* **1962**, *17*, 150-153.
25. Kralj, M.; Pletikoscicacute, I.; Petrovicacute, M.; Pervan, P.; Milun, M.; N'Diaye, A. T.; Busse, C.; Michely, T.; Fujii, J.; Vobornik, I., Graphene on Ir(111) characterized by angle-resolved photoemission. *Physical Review B* **2011**, *84* (7), 075427.
26. Loginova, E.; Bartelt, N. C.; Feibelman, P. J.; McCarty, K. F., Evidence for graphene growth by C cluster attachment. *New Journal of Physics* **2008**, *10* (9), 093026.
27. Loginova, E.; Bartelt, N. C.; Feibelman, P. J.; McCarty, K. F., Factors influencing graphene growth on metal surfaces. *New Journal of Physics* **2009**, *11* (6), 063046.
28. Gao, J.-H.; Ishida, N.; Scott, I.; Fujita, D., Controllable growth of single-layer graphene on a Pd(111) substrate. *Carbon* **2009**, *47* (12), 1674-1680.
29. Addou, R.; Dahal, A.; Sutter, P.; Batzill, M., Monolayer graphene growth on Ni(111) by low temperature chemical vapor deposition. *Applied Physics Letters* **2009**, *95* (2), 021601-3.

30. Yan, C.; Sun, J., Comment on "Mechanism of non-metal catalytic growth of graphene on silicon" [Appl. Phys. Lett. 100, 231604 (2012)]. *Applied Physics Letters* **2012**, *101* (9), 096101-1.
31. Liu, W.; Li, H.; Xu, C.; Khatami, Y.; Banerjee, K., Synthesis of high-quality monolayer and bilayer graphene on copper using chemical vapor deposition. *Carbon* **49** (13), 4122-4130.
32. Hong, G.; Wu, Q.-H.; Ren, J.; Lee, S.-T., Response to "Comment on 'Mechanism of non-metal catalytic growth of graphene on silicon'" [Appl. Phys. Lett. 101, 096101 (2012)]. *Applied Physics Letters* **101** (9), 096102-2.
33. Tang, S.; Ding, G.; Xie, X.; Chen, J.; Wang, C.; Ding, X.; Huang, F.; Lu, W.; Jiang, M., Nucleation and growth of single crystal graphene on hexagonal boron nitride. *Carbon* **2012**, *50* (1), 329-331.
34. Zinn, S.; Semiatin, S., Coil Design and Fabrication: Basic Design and Modifications. *Heat Treating* **1988**, *12*, 32-36.
35. Geng, D.; Wu, B.; Guo, Y.; Huang, L.; Xue, Y.; Chen, J.; Yu, G.; Jiang, L.; Hu, W.; Liu, Y., Uniform hexagonal graphene flakes and films grown on liquid copper surface. *Proceedings of the National Academy of Sciences* **2012**.
36. Yan, Z.; Lin, J.; Peng, Z.; Sun, Z.; Zhu, Y.; Li, L.; Xiang, C.; Samuel, E. L. c.; Kittrell, C.; Tour, J. M., Toward the Synthesis of Wafer-Scale Single-Crystal Graphene on Copper Foils. *ACS Nano* **2012**, *6* (10), 9110-9117.
37. Yu, Q.; Jauregui, L. A.; Wu, W.; Colby, R.; Tian, J.; Su, Z.; Cao, H.; Liu, Z.; Pandey, D.; Wei, D.; Chung, T. F.; Peng, P.; Guisinger, N. P.; Stach, E. A.; Bao, J.; Pei, S.-S.; Chen, Y. P., Control and characterization of individual grains and grain boundaries in graphene grown by chemical vapour deposition. *Nature Materials* **2011**, *10* (6), 443-449.
38. Wu, W.; Jauregui, L. A.; Su, Z.; Liu, Z.; Bao, J.; Chen, Y. P.; Yu, Q., Growth of Single Crystal Graphene Arrays by Locally Controlling Nucleation on Polycrystalline Cu Using Chemical Vapor Deposition. *Advanced Materials* **2011**, *23* (42), 4898-4903.
39. Wu, Y. A.; Fan, Y.; Speller, S.; Creeth, G. L.; Sadowski, J. T.; He, K.; Robertson, A. W.; Allen, C. S.; Warner, J. H., Large Single Crystals of Graphene on Melted Copper Using Chemical Vapor Deposition. *ACS Nano* **2012**, *6* (6), 5010-5017.
40. Wang, H.; Wang, G.; Bao, P.; Yang, S.; Zhu, W.; Xie, X.; Zhang, W.-J., Controllable Synthesis of Submillimeter Single-Crystal Monolayer Graphene Domains on Copper Foils by Suppressing Nucleation. *Journal of the American Chemical Society* **2012**, *134* (8), 3627-3630.
41. Luo, Z.; Kim, S.; Kawamoto, N.; Rappe, A. M.; Johnson, A. T. C., Growth Mechanism of Hexagonal-Shape Graphene Flakes with Zigzag Edges. *ACS Nano* **2011**.
42. Zhang, Y.; Zhang, L.; Kim, P.; Ge, M.; Li, Z.; Zhou, C., Vapor Trapping Growth of Single-Crystalline Graphene Flowers: Synthesis, Morphology, and Electronic Properties. *Nano Letters* **2012**, *12* (6), 2810-2816.
43. Gao, L.; Ren, W.; Xu, H.; Jin, L.; Wang, Z.; Ma, T.; Ma, L.-P.; Zhang, Z.; Fu, Q.; Peng, L.-M.; Bao, X.; Cheng, H.-M., Repeated growth and bubbling transfer of graphene

with millimetre-size single-crystal grains using platinum. *Nature Communications* **2012**, *3*, 699.

44. Iwasaki, T.; Park, H. J.; Konuma, M.; Lee, D. S.; Smet, J. H.; Starke, U., Long-Range Ordered Single-Crystal Graphene on High-Quality Heteroepitaxial Ni Thin Films Grown on MgO(111). *Nano Letters* **2011**, *11* (1), 79-84.

45. Luo, Z.; Lu, Y.; Singer, D. W.; Berck, M. E.; Somers, L. A.; Goldsmith, B. R.; Johnson, A. T. C., Effect of Substrate Roughness and Feedstock Concentration on Growth of Wafer-Scale Graphene at Atmospheric Pressure. *Chemistry of Materials* **2011**, *23* (6), 1441-1447.

46. Ago, H.; Ogawa, Y.; Tsuji, M.; Mizuno, S.; Hibino, H., Catalytic Growth of Graphene: Toward Large-Area Single-Crystalline Graphene. *The Journal of Physical Chemistry Letters* **2012**, *3* (16), 2228-2236.

47. Wood, J. D.; Schmucker, S. W.; Lyons, A. S.; Pop, E.; Lyding, J. W., Effects of Polycrystalline Cu Substrate on Graphene Growth by Chemical Vapor Deposition. *Nano Letters* **2011**, *11* (11), 4547-4554.

48. Kim, H.; Mattevi, C.; Calvo, M. R.; Oberg, J. C.; Artiglia, L.; Agnoli, S.; Hirjibehedin, C. F.; Chhowalla, M.; Saiz, E., Activation Energy Paths for Graphene Nucleation and Growth on Cu. *ACS Nano* **2012**, *6* (4), 3614-3623.

49. Ding, W.; Dikin, D.; Chen, X.; Piner, R.; Ruoff, R.; Zussman, E.; Wang, X.; Li, X., Mechanics of hydrogenated amorphous carbon deposits from electron-beam-induced deposition of a paraffin precursor. *Journal of Applied Physics* **2005**, *98* (1), 014905-014905-7.

50. Choubak, S.; Biron, M.; Levesque, P. L.; Martel, R.; Desjardins, P., No Graphene Etching in Purified Hydrogen. *The Journal of Physical Chemistry Letters* **2013**, *4* (7), 1100-1103.

51. Santoni, A.; Urban, J., AES and EELS investigation of carbonaceous layers on Cu(110) and Cu(100). *Surface Science* **1987**, *186* (3), 376-382.

52. Zhang, B.; Lee, W. H.; Piner, R.; Kholmanov, I.; Wu, Y.; Li, H.; Ji, H.; Ruoff, R. S., Low-Temperature Chemical Vapor Deposition Growth of Graphene from Toluene on Electropolished Copper Foils. *ACS Nano* **2012**, *6* (3), 2471-2476.

53. Ferrari, A. C.; Basko, D. M., Raman spectroscopy as a versatile tool for studying the properties of graphene. *Nature Nanotechnology* **2013**, *8* (4), 235-246.

54. Malard, L. M.; Pimenta, M. A.; Dresselhaus, G.; Dresselhaus, M. S., Raman spectroscopy in graphene. *Physics Reports* **2009**, *473* (5-6), 51-87.

55. Li, X.; Cai, W.; Colombo, L.; Ruoff, R. S., Evolution of Graphene Growth on Ni and Cu by Carbon Isotope Labeling. *Nano Letters* **2009**, *9* (12), 4268-4272.

56. Chen, S.; Brown, L.; Levendorf, M.; Cai, W.; Ju, S.-Y.; Edgeworth, J.; Li, X.; Magnuson, C. W.; Velamakanni, A.; Piner, R. D.; Kang, J.; Park, J.; Ruoff, R. S., Oxidation Resistance of Graphene-Coated Cu and Cu/Ni Alloy. *ACS Nano* **2011**, *5* (2), 1321-1327.

57. Poulston, S.; Parlett, P. M.; Stone, P.; Bowker, M., Surface Oxidation and Reduction of CuO and Cu<sub>2</sub>O Studied Using XPS and XAES. *Surface and Interface Analysis* **1996**, *24* (12), 811-820.
58. Dubé, C. E.; Workie, B.; Kounaves, S. P.; Robbat, A.; Aksub, M. L.; Davies, G., Electrodeposition of Metal Alloy and Mixed Oxide Films Using a Single-Precursor Tetranuclear Copper-Nickel Complex. *Journal of The Electrochemical Society* **1995**, *142* (10), 3357-3365.
59. Goswami, A.; Trehan, Y. N., The Thermal Decomposition of Cupric Oxide in vacuo. *Proceedings of the Physical Society B* **1957**, *70*, 1005.
60. Gan, Z. H.; Yu, G. Q.; Tay, B. K.; Tan, C. M.; Zhao, Z. W.; Fu, Y. Q., Preparation and characterization of copper oxide thin films deposited by filtered cathodic vacuum arc. *Journal of Physics D: Applied Physics* **2004**, *37* (1), 81.
61. Gong, Y. S.; Lee, C.; Yang, C. K., Atomic force microscopy and Raman spectroscopy studies on the oxidation of Cu thin films. *Journal of Applied Physics* **1995**, *77* (10), 5422-5425.
62. Kodera, K.; Kusunoki, I.; Shimizu, S., Dissociation Pressures of Various Metallic Oxides. *Bulletin of the Chemical Society of Japan* **1968**, *41* (5), 1039-1045.
63. Hallstedt, B.; Risold, D.; Gauckler, L. J., Thermodynamic assessment of the copper-oxygen system. *JPE* **1994**, *15* (5), 483-499.
64. Kagwade, S. V.; Clayton, C. R.; Chidambaram, D.; Halada, G. P., Photochemical breakdown of acetone on copper. *Electrochimica Acta* **2001**, *46* (15), 2337-2342.
65. Ryu, J.; Kim, Y.; Won, D.; Kim, N.; Park, J. S.; Lee, E.-K.; Cho, D.; Cho, S.-P.; Kim, S. J.; Ryu, G. H.; Shin, H.-A. S.; Lee, Z.; Hong, B. H.; Cho, S., Fast Synthesis of High-Performance Graphene Films by Hydrogen-Free Rapid Thermal Chemical Vapor Deposition. *ACS Nano* **2013**, *ASAP*.
66. Velamakanni, A.; Magnuson, C. W.; Ganesh, K. J.; Zhu, Y.; An, J.; Ferreira, P. J.; Ruoff, R. S., Site-Specific Deposition of Au Nanoparticles in CNT Films by Chemical Bonding. *ACS Nano* **2010**, *4* (1), 540-546.
67. Cao, Q.; Rogers, J. A., Ultrathin Films of Single-Walled Carbon Nanotubes for Electronics and Sensors: A Review of Fundamental and Applied Aspects. *Advanced Materials* **2009**, *21* (1), 29-53.
68. Gruner, G., Carbon nanotube films for transparent and plastic electronics. *Journal of Materials Chemistry* **2006**, *16* (35), 3533-3539.
69. Gruner, G., Carbon Nanonets Spark New Electronics. *Scientific American* **2007**, *296*, 76-83.
70. Hicks, J.; Behnam, A.; Ural, A., Resistivity in percolation networks of one-dimensional elements with a length distribution. *Physical Review E* **2009**, *79* (1), 012102.
71. Behnam, A.; Ural, A., Computational study of geometry-dependent resistivity scaling in single-walled carbon nanotube films. *Physical Review B* **2007**, *75* (12), 125432.

72. Khoo, K. H.; Chelikowsky, J. R., Electron transport across carbon nanotube junctions decorated with Au nanoparticles: Density functional calculations. *Physical Review B* **2009**, *79* (20), 205422.
73. Berhan, L.; Sastry, A. M., On Modeling Bonds in Fused, Porous Networks: 3D Simulations of Fibrous–Particulate Joints. *Journal of Composite Materials* **2003**, *37* (8), 715-740.
74. Berhan, L.; Yi, Y. B.; Sastry, A. M.; Munoz, E.; Selvidge, M.; Baughman, R., Mechanical properties of nanotube sheets: Alterations in joint morphology and achievable moduli in manufacturable materials. *Journal of Applied Physics* **2004**, *95* (8), 4335-4345.
75. Yu, M.-F.; Lourie, O.; Dyer, M. J.; Moloni, K.; Kelly, T. F.; Ruoff, R. S., Strength and Breaking Mechanism of Multiwalled Carbon Nanotubes Under Tensile Load. *Science* **2000**, *287* (5453), 637-640.
76. Kong, B.-S.; Jung, D.-H.; Oh, S.-K.; Han, C.-S.; Jung, H.-T., Single-Walled Carbon Nanotube Gold Nanohybrids: Application in Highly Effective Transparent and Conductive Films. *The Journal of Physical Chemistry C* **2007**, *111* (23), 8377-8382.
77. Shi, Y.; Yang, R.; Yuet, P. K., Easy decoration of carbon nanotubes with well dispersed gold nanoparticles and the use of the material as an electrocatalyst. *Carbon* **2009**, *47* (4), 1146-1151.
78. Lin, Z.; Huang, L.; Liu, Y.; Lin, J.-M.; Chi, Y.; Chen, G., Electrochemiluminescent biosensor based on multi-wall carbon nanotube/nano-Au modified electrode. *Electrochemistry Communications* **2008**, *10* (11), 1708-1711.
79. Lawson, G.; Gonzaga, F.; Huang, J.; de Silveira, G.; Brook, M. A.; Adronov, A., Au-carbon nanotube composites from self-reduction of Au<sup>3+</sup> upon poly(ethylene imine) functionalized SWNT thin films. *Journal of Materials Chemistry* **2008**, *18* (14), 1694-1702.
80. Oliveira, M. M.; Zarbin, A. J. G., Carbon Nanotubes Decorated with both Gold Nanoparticles and Polythiophene. *The Journal of Physical Chemistry C* **2008**, *112* (48), 18783-18786.
81. Rabbani, M. M.; Ko, C. H.; Bae, J.-S.; Yeum, J. H.; Kim, I. S.; Oh, W., Comparison of some gold/carbon nanotube composites prepared by control of electrostatic interaction. *Colloids and Surfaces A: Physicochemical and Engineering Aspects* **2009**, *336* (1–3), 183-186.
82. Gingery, D.; Bühlmann, P., Formation of gold nanoparticles on multiwalled carbon nanotubes by thermal evaporation. *Carbon* **2008**, *46* (14), 1966-1972.
83. Hang, Q.; Maschmann, M. R.; Fisher, T. S.; Janes, D. B., Assemblies of Carbon Nanotubes and Unencapsulated Sub-10-nm Gold Nanoparticles. *Small* **2007**, *3* (7), 1266-1271.
84. Showkat, A. M.; Lee, K.-P.; Gopalan, A. I.; Choi, S.-H.; Nho, Y. C., Dispersion of gold nanoparticles into thiol-functionalized carbon nanotubes by  $\gamma$ -radiation. *Diamond and Related Materials* **2007**, *16* (8), 1688-1692.

85. Zhang, Y.; Franklin, N. W.; Chen, R. J.; Dai, H., Metal coating on suspended carbon nanotubes and its implication to metal–tube interaction. *Chemical Physics Letters* **2000**, *331* (1), 35-41.
86. Mougin, K.; Zheng, Z.; Piazzon, N.; Gnecco, E.; Haidara, H., Thermal stability and reconstruction of nanoparticulate Au film on model molecular surfaces. *Journal of Colloid and Interface Science* **2009**, *333* (2), 719-724.
87. Yablokov, V. A.; Vasina, Y. A.; Zelyaev, I. A.; Mitrofanova, S. V., Kinetics of thermal decomposition of sulfur-containing amino acids. *Russ J Gen Chem* **2009**, *79* (6), 1141-1145.
88. Ganesh, K. J.; Kawasaki, M.; Zhou, J. P.; Ferreira, P. J., D-STEM: A Parallel Electron Diffraction Technique Applied to Nanomaterials. *Microscopy and Microanalysis* **2010**, *16* (05), 614-621.
89. Briggs, D., *Handbook of X ray and Ultraviolet Photoelectron Spectroscopy*. Hayden and Son Ltd.: 1978.
90. Briggs, D.; Seah, M. P., *Practical Surface Analysis: Auger and X-ray Photoelectron Spectroscopy*. John Wiley and Sons: 1996; Vol. I.
91. Castner, D. G.; Hinds, K.; Grainger, D. W., X-ray Photoelectron Spectroscopy Sulfur 2p Study of Organic Thiol and Disulfide Binding Interactions with Gold Surfaces. *Langmuir* **1996**, *12* (21), 5083-5086.
92. Cavalleri, O.; Gonella, G.; Terreni, S.; Vignolo, M.; Pelori, P.; Floreano, L.; Morgante, A.; Canepa, M.; Rolandi, R., High resolution XPS of the S 2p core level region of the L-cysteine/gold interface. *Journal of Physics: Condensed Matter* **2004**, *16* (26), S2477.
93. Doderio, G.; De Michieli, L.; Cavalleri, O.; Rolandi, R.; Oliveri, L.; Daccà, A.; Parodi, R., l-Cysteine chemisorption on gold: an XPS and STM study. *Colloids and Surfaces A: Physicochemical and Engineering Aspects* **2000**, *175* (1–2), 121-128.
94. Benayad, A.; Shin, H.-J.; Park, H. K.; Yoon, S.-M.; Kim, K. K.; Jin, M. H.; Jeong, H.-K.; Lee, J. C.; Choi, J.-Y.; Lee, Y. H., Controlling work function of reduced graphite oxide with Au-ion concentration. *Chemical Physics Letters* **2009**, *475* (1–3), 91-95.
95. XPS Studies of Supported Gold Catalysts the Role of Au<sup>0</sup> and Au<sup>δ+</sup> Species as Active Sites. *Surf. Interface Anal* **2006**, *38*, 215-218.
96. van der Pauw, L. J., A Method of Measuring the Resistivity and Hall Coefficient on Lamellae of Arbitrary Shape. *Philips Technical Review* **1958**, *20*, 220-224.
97. Ruoff, R. S. Method and System for Improving Conductivity and Mechanical Performance of Carbon Nanotube Nets and Related Materials. *Patent Application #20090155460* **2009**.
98. Rodríguez-Manzo, J. A.; Wang, M.-S.; Banhart, F.; Bando, Y.; Golberg, D., Multibranch Junctions of Carbon Nanotubes via Cobalt Particles. *Advanced Materials* **2009**, *21* (44), 4477-4482.

99. Ramanathan, T.; Fisher, F. T.; Ruoff, R. S.; Brinson, L. C., Amino-Functionalized Carbon Nanotubes for Binding to Polymers and Biological Systems. *Chemistry of Materials* **2005**, *17* (6), 1290-1295.
100. Aryal, S.; B.K.C, R.; Dharmaraj, N.; Bhattarai, N.; Kim, C. H.; Kim, H. Y., Spectroscopic identification of SAu interaction in cysteine capped gold nanoparticles. *Spectrochimica Acta Part A: Molecular and Biomolecular Spectroscopy* **2006**, *63* (1), 160-163.
101. Wu, Z.; Chen, Z.; Du, X.; Logan, J. M.; Sippel, J.; Nikolou, M.; Kamaras, K.; Reynolds, J. R.; Tanner, D. B.; Hebard, A. F.; Rinzler, A. G., Transparent, Conductive Carbon Nanotube Films. *Science* **2004**, *305* (5688), 1273-1276.
102. Suk, J. W.; Kitt, A.; Magnuson, C. W.; Hao, Y.; Ahmed, S.; An, J.; Swan, A. K.; Goldberg, B. B.; Ruoff, R. S., Transfer of CVD-Grown Monolayer Graphene onto Arbitrary Substrates. *ACS Nano* **2011**, *5* (9), 6916-6924.
103. Kholmanov, I. N.; Magnuson, C. W.; Aliev, A. E.; Li, H.; Zhang, B.; Suk, J. W.; Zhang, L. L.; Peng, E.; Mousavi, S. H.; Khanikaev, A. B.; Piner, R.; Shvets, G.; Ruoff, R. S., Improved Electrical Conductivity of Graphene Films Integrated with Metal Nanowires. *Nano Letters* **2012**, *12* (11), 5679-5683.
104. Kholmanov, I. N.; Magnuson, C. W.; Piner, R.; Kim, J.-Y.; Kim, T.; Aliev, A. E.; Tan, C.; Zakhidov, A. A.; Baughman, R. H.; Ruoff, R. S., Elastomeric and transparent conducting films by sandwiching an oriented carbon nanotube sheet between two graphene layers *submitted to Nature Communications* **2014**.
105. Li, X.; Magnuson, C. W.; Venugopal, A.; Tromp, R. M.; Hannon, J. B.; Vogel, E. M.; Colombo, L.; Ruoff, R. S., Large-Area Graphene Single Crystals Grown by Low-Pressure Chemical Vapor Deposition of Methane on Copper. *Journal of the American Chemical Society* **2011**, *133* (9), 2816-2819.
106. Li, X.; Magnuson, C. W.; Venugopal, A.; An, J.; Suk, J. W.; Han, B.; Borysiak, M.; Cai, W.; Velamakanni, A.; Zhu, Y.; Fu, L.; Vogel, E. M.; Voelkl, E.; Colombo, L.; Ruoff, R. S., Graphene Films with Large Domain Size by a Two-Step Chemical Vapor Deposition Process. *Nano Letters* *10* (11), 4328-4334.
107. Huang, P. Y.; Ruiz-Vargas, C. S.; van der Zande, A. M.; Whitney, W. S.; Levendorf, M. P.; Kevek, J. W.; Garg, S.; Alden, J. S.; Hustedt, C. J.; Zhu, Y.; Park, J.; McEuen, P. L.; Muller, D. A., Grains and grain boundaries in single-layer graphene atomic patchwork quilts. *Nature* **2011**, *469* (7330), 389-392.
108. Yazyev, O. V.; Louie, S. G., Electronic transport in polycrystalline graphene. *Nat Mater* **2010**, *9* (10), 806-809.
109. Bauer, E., Low energy electron microscopy *Reports on Progress in Physics* **1994**, *57* (9), 895-938.
110. Knox, K. R.; Wang, S.; Morgante, A.; Cvetko, D.; Locatelli, A.; Menten, T. O.; Niño, M. A.; Kim, P.; Osgood, R. M., Spectromicroscopy of single and multilayer graphene supported by a weakly interacting substrate. *Physical Review B* **2008**, *78* (20), 201408.

111. Li, X.; Zhu, Y.; Cai, W.; Borysiak, M.; Han, B.; Chen, D.; Piner, R. D.; Colombo, L.; Ruoff, R. S., Transfer of Large-Area Graphene Films for High-Performance Transparent Conductive Electrodes. *Nano Letters* **2009**, *9* (12), 4359-4363.
112. Casiraghi, C.; Pisana, S.; Novoselov, K. S.; Geim, A. K.; Ferrari, A. C., Raman fingerprint of charged impurities in graphene. *Applied Physics Letters* **2007**, *91* (23), 233108.
113. Kim, S.; Nah, J.; Jo, I.; Shahrjerdi, D.; Colombo, L.; Yao, Z.; Tutuc, E.; Banerjee, S. K., Realization of a high mobility dual-gated graphene field-effect transistor with Al<sub>2</sub>O<sub>3</sub> dielectric. *Applied Physics Letters* **2009**, *94* (6), 062107.
114. Hao, Y.; Bharathi, M. S.; Wang, L.; Liu, Y.; Chen, H.; Nie, S.; Wang, X.; Chou, H.; Tan, C.; Fallahazad, B.; Ramanarayan, H.; Magnuson, C. W.; Tutuc, E.; Yakobson, B. I.; McCarty, K. F.; Zhang, Y.-W.; Kim, P.; Hone, J.; Colombo, L.; Ruoff, R. S., The Role of Surface Oxygen in the Growth of Large Single-Crystal Graphene on Copper. *Science* **2013**, *342* (6159), 720-723.
115. Wu, B.; Geng, D.; Guo, Y.; Huang, L.; Xue, Y.; Zheng, J.; Chen, J.; Yu, G.; Liu, Y.; Jiang, L.; Hu, W., Equiangular Hexagon-Shape-Controlled Synthesis of Graphene on Copper Surface. *Advanced Materials* **2011**, *23* (31), 3522-3525.
116. Yazyev, O. V.; Pasquarello, A., Effect of Metal Elements in Catalytic Growth of Carbon Nanotubes. *Physical Review Letters* **2008**, *100* (15), 156102.
117. Li, Q.; Chou, H.; Zhong, J.-H.; Liu, J.-Y.; Dolocan, A.; Zhang, J.; Zhou, Y.; Ruoff, R. S.; Chen, S.; Cai, W., Growth of Adlayer Graphene on Cu Studied by Carbon Isotope Labeling. *Nano Letters* **2013**, *13* (2), 486-490.
118. Zhang, X.; Wang, L.; Xin, J.; Yakobson, B. I.; Ding, F., The Role of Hydrogen in Graphene Chemical Vapor Deposition (CVD) Growth on Copper Surface. *JACS* **submitted**.
119. Hao, Y.; al., e., **Manuscript in preperation**.
120. Piner, R.; Li, H.; Kong, X.; Tao, L.; Kholmanov, I. N.; Ji, H.; Lee, W. H.; Suk, J. W.; Ye, J.; Hao, Y.; Chen, S.; Magnuson, C. W.; Ismach, A. F.; Akinwande, D.; Ruoff, R. S., Graphene Synthesis via Magnetic Inductive Heating of Copper Substrates. *ACS Nano* **2013**, *7* (9), 7495-7499.
121. Jung, D. H.; Kang, C.; Kim, M.; Cheong, H.; Lee, H.; Lee, J. S., Effects of Hydrogen Partial Pressure in the Annealing Process on Graphene Growth. *The Journal of Physical Chemistry C* **2014**.
122. Vlassiuk, I.; Regmi, M.; Fulvio, P.; Dai, S.; Datskos, P.; Eres, G.; Smirnov, S., Role of Hydrogen in Chemical Vapor Deposition Growth of Large Single-Crystal Graphene. *ACS Nano* **2011**, *5* (7), 6069-6076.
123. Mattevi, C.; Kim, H.; Chhowalla, M., A review of chemical vapour deposition of graphene on copper. *Journal of Materials Chemistry* **2011**, *21* (10), 3324-3334.
124. Bhaviripudi, S.; Jia, X.; Dresselhaus, M. S.; Kong, J., Role of Kinetic Factors in Chemical Vapor Deposition Synthesis of Uniform Large Area Graphene Using Copper Catalyst. *Nano Letters* **2010**, *10* (10), 4128-4133.

125. Tao, L.; Lee, J.; Chou, H.; Holt, M.; Ruoff, R. S.; Akinwande, D., Synthesis of High Quality Monolayer Graphene at Reduced Temperature on Hydrogen-Enriched Evaporated Copper (111) Films. *ACS Nano* **2012**, *6* (3), 2319-2325.
126. Gao, L.; Ren, W.; Zhao, J.; Ma, L.-P.; Chen, Z.; Cheng, H.-M., Efficient growth of high-quality graphene films on Cu foils by ambient pressure chemical vapor deposition. *Applied Physics Letters* **2010**, *97* (18).
127. Ryu, J.; Kim, Y.; Won, D.; Kim, N.; Park, J. S.; Lee, E.-K.; Cho, D.; Cho, S.-P.; Kim, S. J.; Ryu, G. H.; Shin, H.-A. S.; Lee, Z.; Hong, B. H.; Cho, S., Fast Synthesis of High-Performance Graphene Films by Hydrogen-Free Rapid Thermal Chemical Vapor Deposition. *ACS Nano* **2014**, *8* (1), 950–956.
128. Shapovalov, V., Proceedings of the 1999 International Symposium on Liquid Metal Processing and Casting. *Santa Fe, New Mexico* **1999**, 21-24.
129. Wampler, W. R.; Schober, T.; Lengeler, B., Precipitation and trapping of hydrogen in copper. *Philosophical Magazine* **1976**, *34* (1), 129-141.
130. Ellis, D. E.; Mundim, K. C.; Fuks, D.; Dorfman, S.; Berner, A., Interstitial carbon in copper: electronic and mechanical properties. *Philosophical Magazine B* **1999**, *79* (10), 1615-1630.
131. Sinclair, R.; Itoh, T.; Chin, R., In Situ TEM Studies of Metal-Carbon Reactions. *Microscopy and Microanalysis* **2002**, *8* (04), 288-304.
132. Donnelly, S. E.; Evans, J. H., *Fundamental aspects of inert gases in solids / edited by S.E. Donnelly and J.H. Evans*. Plenum Press: New York, 1991.
133. Hagi, H., Diffusion Coefficient of Hydrogen in Ni-Cu and Ni-Co Alloys. *J. Japan Inst. Metals* **1983**, *47* (17), 1029-1035.
134. Kurnosikov, O.; Kulikov, D. V.; Kharlamov, V. S.; Swagten, H. J. M.; Trushin, Y. V., Temperature-induced evolution of subsurface nanocavities in argon-implanted copper. *Physical Review B* **2011**, *84* (5), 054109.
135. Kuhalainen, J.; Manninen, M.; Kautto, E., Helium, neon and argon in copper studied with the effective medium theory *Journal of Physics: Condensed Matter* **1996**, *8* (49), 10317-10326.
136. Wilson, W. D.; Bisson, C. L., Atomistics of helium diffusion in copper and tungsten. *Radiation Effects* **1973**, *19* (1), 53-58.
137. Magnuson, C. W.; Kong, X.; Ji, H.; Tan, C.; Li, H.; Piner, R.; Ventrice, C. A.; Ruoff, R. S., Copper Oxide as a ‘Self-cleaning’ Substrate for Graphene Growth. *JMR Accepted*.
138. Vargaftik, N. B.; Zimina, N. K., Thermal conductivity of helium at temperatures of 0–1000°C and pressures of 1–200 atm. *At Energy* **1965**, *19* (3), 1221-1225.
139. Chen, S. H. P.; Saxena, S. C., Thermal conductivity of argon in the temperature range 350 to 2500 K. *Molecular Physics* **1975**, *29* (2), 455-466.
140. Ferrari, A. C., Raman spectroscopy of graphene and graphite: Disorder, electron-phonon coupling, doping and nonadiabatic effects. *Solid State Communications* **2007**, *143* (1–2), 47-57.

141. Lazzeri, M.; Mauri, F., Nonadiabatic Kohn Anomaly in a Doped Graphene Monolayer. *Physical Review Letters* **2006**, *97* (26), 266407.
142. Kalbac, M.; Kong, J.; Dresselhaus, M. S., Raman Spectroscopy as a Tool to Address Individual Graphene Layers in Few-Layer Graphene. *The Journal of Physical Chemistry C* **2012**, *116* (35), 19046–19050.
143. Yoon, D.; Son, Y.-W.; Cheong, H., Negative Thermal Expansion Coefficient of Graphene Measured by Raman Spectroscopy. *Nano Letters* **2011**, *11* (8), 3227-3231.
144. Yazyev, O. V., Polycrystalline graphene: Atomic structure, energetics and transport properties. *Solid State Communications* **2012**, *152* (15), 1431-1436.

## **Vita**

Carl W. Magnuson attended the University of Southern California from 2000-2005 on the Trustee Scholarship. At USC he was a Merit Researcher in the Mirco Photonics Device Group under Prof. O'Brien and received his Bachelors of Science in Electrical Engineering in 2005. From 2003-2004, he studied Chinese language and culture at Peking University through the National Security Education Program's David L. Boren Scholarship. He worked as a systems engineer from 2005-2008 on the Space Based Infrared Systems at Northrop Grumman Electronic Systems. In 2008, he moved to Austin, Texas, to earn his Doctorate of Philosophy in Materials Science studying carbon based nano-materials under Prof. Ruoff at the University of Texas. He received Sandia National Lab's Laboratory Directed Research and Development Fellowship from 2010-2013.

Permanent email: [carl.magnuson@utexas.edu](mailto:carl.magnuson@utexas.edu)

This dissertation was typed by the author.